Nanopore-extrusion Induced Sphere-to-cylinder Transition of Block Copolymer Micelles

CHEN, Qianjin

A Thesis Submitted in Partial Fulfilment

of the Requirements for the Degree of

Doctor of Philosophy

in

Chemistry

The Chinese University of Hong Kong

August 2013

Thesis/Assessment Committee

Professor To Ngai (Chair)

Professor Chi Wu (Thesis Supervisor)

Professor Jianfang Wang (Committee Member)

Professor Charles C. Han (External Examiner)

摘　要

眾所周知，兩親性嵌段高分子溶解於選擇性溶劑中時，其憎溶劑的嵌段傾向於發生聚集，從而高分子鏈會發生自組裝行為，進而得到一系列的聚集形態，包括有球狀，柱狀以及囊泡狀的結構。 通過調控高分子於溶劑之間的相互作用，不同的聚集形態之間可以發生轉變。具體的調控方法包括有高分子的嵌段組分、溶劑的性質以及溶液溫度等。在此篇博士論文中，我們將嵌段聚合物球狀膠束用於直徑為二十納米的納米孔進行超濾擠出實驗時，發現在特定的條件下出現了由球狀到柱狀（蠕蟲狀）膠束的轉變。擠出後，這些細長的納米線並沒有像預期得那樣快速的解散成初始的球狀膠束的結構，相反，整個解散過程持續了相當長的時間（數天到一週）。

首先，為了進一步理解由納米孔擠壓誘導下高分子膠束從球狀到柱狀的變化機理，我們系統得研究了嵌段高分子組成、高分子鏈的長度、溶劑性質以及超濾擠出實驗時的流速對擠出結果的影響。我們使用了激光光散射技術和透射電子顯微鏡技術來表徵了在納米孔擠出之前和之後的膠束形貌結構。此外，我們還測量了在擠出過程中，納米孔超濾膜兩側的壓強差的變化。基於上述的研究結果，我們基本比較清楚球狀膠束在納米孔擠出過程是如何轉變成柱狀的膠束。

具體來說，當納米孔擠出開始時，那些流體力學半徑尺寸大約三十納米的球狀膠束首先會被卡在比他們小很多的納米孔前。隨著不斷增加的剪切流下的液體動力，這些球狀膠束最終會發生變形進而被擠入到納米孔中，並在納米孔內發生互相融合。由於球狀膠束在納米孔前源源不斷的發生堆積，以及它們在納米孔內的互相融合和重排，這樣最終在納米孔的出口得到了細長的柱狀膠束。我們的實驗結果顯示，膠束的軟硬度，尤其是膠束核的軟硬度，對球狀到柱狀的轉變起到了很關鍵的作用。 當膠束核內分子間作用太強，或者說膠束核太硬時，他們在剪切流下很難發生形變進入納米孔內，而且後期在納米孔內的相互融合和分子重排過程亦較難發生。相反，當膠束核內分子間作用太弱，或者說膠束核太軟，球狀膠束在強剪切力作用進入納米孔前有可能發生解散或者

在後期形成的柱狀膠束也會很快得解散。在本課題中，高分子膠束的軟硬度主要是依靠調節混合溶劑中良溶劑的比例來實現的。

其次，我們進一步結合了光散射和掃描電鏡技術定量得研究了擠出後得到的柱狀膠束的緩慢解散動力學和解散機理。實驗結果證實納米線的伸直長度隨著解散時間不斷降低，直至全部變回初始的球狀膠束形貌。通過對不同解散時間下柱狀膠束納米結構的顯微鏡圖片研究，我們又對解散過程的斷裂機理和相應的降解驅動力進行了詳細討論。經過對不同斷裂模型的計算模擬比較，結果顯示納米線既有在末端斷裂的機理，也有斷裂點沿著納米線高斯分佈的機理，而斷裂速率常數則正比於納米線的伸直長度，並且隨著時間略有增加。

最後，我們進一步採用納米孔擠壓誘導嵌段高分子膠束由球狀到柱狀的轉變的方法來製備各種柱狀雜化高分子功能材料。首先將功能型金屬納米顆粒包覆在高分子球狀膠束的中間，然後通過簡單的納米孔擠壓方法，將金屬納米顆粒均勻得沿著納米線的方向分佈。這種得到的一維的複合納米線材料擁有特殊的光學性能並且在納米器件製備上有潛在的應用。更加重要的是，如果能夠在擠出後將這些數以十億計的納米線在剪切流暢下進行取向排列，並且最終紡絲成一股由大量取向了的納米線組成的纖維，那麼這種得到的化學交聯的，取向的纖維將擁有傑出的機械性能。因此，我們發現的納米孔擠壓誘導嵌段高分子膠束由球狀到柱狀的轉變的方法一定程度上為製備高性能多功能的聚合物纖維提供了可能。

Abstract

Amphiphilic block copolymers can self-assemble into colloidal particles with various structures (phases), including spheres, cylinders and vesicles, in a selective solvent. These phases can be transformed from one to another, conventionally, by an alternation of the polymer-solvent interaction that is affected by the block copolymer composition and the solvent quality. In this thesis study, we found that the extrusion of a block copolymer solution in its spherical micelle phase through a commercial 20-nm nanopore under a proper condition can also induce the sphere-to-cylinder transition to form long wormlike micelles. Not as expected, such formed wormlike micelles do not quickly disassemble back to their original spherical but undergo a slow dissociation process over a long time period (days or even weeks) before returning to their original thermodynamically stable spherical morphology.

To understand such a nanopore-extrusion induced sphere-to-cylinder transition, we further investigated effects of the copolymer composition, chain length, solvent quality and extrusion flow rate. Using a combination of laser light scattering and transmission electron microscopy, we characterized the micelle morphology in the copolymer solution before and after the nanopore-extrusion. In addition, we also monitored the hydraulic pressure drop across the nanopore during the nanopore-extrusion. On the basis of these studies, we have qualitatively learned how those spherical micelles are transformed into long cylindrical micelles in the nanopore extrusion.

As the extrusion started, those spherical micelles with a hydrodynamic radius of 30 nm were naturally blocked at the entrance of smaller pores (20 nm). Under the hydrodynamic force of the elongational flow field, the blocked spherical micelles were squeezed into the nanopore and undergo a inter-micelle fusion inside the nanopore while more spherical micelles are accumulated at the pore entrance, resulting in a rearrangement of individual spherical micelles into a long cylindrical micelle inside each nanopore. Our results showed that it is critically important to control the softness of micelles, especially their core; namely, the interchain

interaction inside the core should not be too strong so that the inter-micelle fusion can occur under the external compression, but also not too weak so that the resultant cylindrical micelles after the extrusion will not quickly disintegrated back to small spherical micelles. Such interchain interaction (the softness of the core) can be adjusted by the solvent quality.

Further, we quantitatively studied the slow cylinder-to-sphere dissociation kinetics by a combination of laser light scattering and electron microscopy. The results show the weight-average length of the fibers formed after the extrusion gradually decreases. The dissociation mechanism and driving force are discussed on the basis of the TEM analysis of the structures of the fiber at different dissociation times. The simulation of the dissociation using various scission models reveals that the cylinder fragmentation follows a combination of the Gaussian and end scission model and the scission rate constant is essentially a linear function of the fiber length and slightly increases with time.

This thesis study also leads to a novel way to prepare various functional polymeric cylindrical core-shell micelles (nanowires). By incorporating metal nanoparticles inside the initial spherical micelles, long hybrid cylindrical micelles can be prepared by extruding them through nanopores. Such prepared “nanowires” have some unique photo-properties and are potentially useful in nano-devices. More importantly, in comparison with long and disorientated cylindrical micelles normally formed in a selective solvent, the production of billions nanowires in one extrusion using a membrane with parallel nanopores looks promising. These nanowires might be aligned under the elongation flow so that they could be spun into a microscopic fiber bundle (microfiber). Therefore, the extrusion studied in this thesis provides a possible way to manufacture high-quality and functional polymeric microfibers (nanowires) in the future.

Acknowledgement

Foremost, I would like to express my sincere gratitude to my supervisor, Professor Chi Wu, for his insightful guidance and encouragement during the entire period of my study in the department of chemistry of the Chinese University of Hong Kong. I entered the *Polymer & Colloid Laboratory* in 2008 and during the last five years in this laboratory, I always feel warm and gratefulness since he has spent much time to give me his excellent guidance and considerations. Not only I have learned a lot from him; but also been inspired by his passion to the scientific research. I believe the trainings and experiences I gained from him should be great helpful in my future.

My sincere thanks are also given to my dear group members in the *Polymer & Colloid Laboratory*, their friendship and assistance during the last five years left me many happy and unforgettable memories. They are Prof. Fan Jin, Prof. Liangzhi Hong, Dr. Xiangjun Gong, Dr. Rui Deng, Dr. Hui Ge, Dr. Shu Diao, Dr. Yanan Yue, Mr. Hong Zhao, Mr. Yongzheng Ma, Ms. Zhuojun Dai, Mr. Jianqi Wang, Ms. Jinge Cai, Mr. Yuan Li, Mr. Wei Liu, Mr. Xiaoqing Ming, Ms. Baizhu Chen and Ms. Yanjing Wang in Room 226. Labmates in RRSSB 210 are also thanked. They are Dr. Zifu Li, Dr. Xiaoling Wei, Dr. Xiaochen Xing, Mr. Guanqing Sun, Ms.Jingjing Wei, Mr. Xiaodong Li, Ms. Li Hua, Ms. Zhaohui Wang, Mr. Yifeng Sheng.

I am also very grateful to Prof. To Ngai and Prof. Jianfang Wang for their help including fruitful discussions and invaluable advices. Thanks are also given to those visiting Professors and scholars, Prof. Gaojian Chen, Prof. Zaijun Lu, Prof. Shizhong Luo, Prof. Yonggang Shangguan, Dr. Ning He.

Thanks are also given to all the staff members in the Department of Chemistry, the Chinese University of Hong Kong for the active academic atmosphere and the service they offered. The financial support of the Hong Kong Special Administration Region Earmarked Grants is gratefully acknowledged.

Finally, I am also indebted to my family for their endless love and strong moral support during my pursuit of a higher degree. I also thank all of my friends who understand and encourage me and let me know more about the world and people.

Chen, Qianjin

May, 2013

CUHK

Table of Contents

List of Symbols and Abbreviations

a:	Monomer size
A_2:	Second viral coefficient
A_S	Peak area contribution of spheres in hydrodynamic radius distribution
A_C	Peak area contribution of cylinders in hydrodynamic radius distribution
b:	Monomer number between successive branch point
C:	Concentration after aultrafiltration
C_0:	Concentration before ultrafiltration
CONTIN:	A regularization program from Provencher
CMC:	Critical micelle concentration
D:	Diameter of nanopore
dn/dC:	Refractive-index increment
E_s:	Scattered electric field
E_{conf}:	Confined energy
E_h:	Hydrodynamic energy
$f(\tau)$:	Characteristic decay time distribution
$f(R_h)$:	Hydrodynamic radius distribution
F_h:	Hydrodynamic force
F_w	Weight length frequency
$G^{(1)}(\tau)$:	Correlation function of electric field
$g^{(1)}(\tau)$:	Normalized first-order electric field time correlation function
$g^{(2)}(\tau)$:	Base-line normalized intensity time correlation function
$G(\Gamma)$:	Normalized characteristic line-width distribution function of Γ
$G^{(2)}(\tau)$:	Correlation function of intensity
I:	Scattered intensity
<I>:	Ensemble-averaged scattered light intensity
I_0:	Intensity of the incident radiation
I_B	Electric current blockade
k_B:	Boltzmann constant
k_{ij}	Scission rate of a micelle of length L_i into two shorter cylinders

	with *i* and *i-j* subunits
l_e:	Effective length of one blob along the flow field
L_n	Number length of nanofibers
L_W	Weight length of nanofibers
LLS:	Laser light scattering
M_w:	Apparent weight average molar weight at a finite concentration
M_b:	Molecular weight of one blob
n:	Solvent refractive index
N_A:	Avogadro's number
PS:	Polystyrene
PI:	Polyisoprene
$P(\theta)$:	Particle scattering factor
$<R_g>$:	z-average radius of gyration
$<R_h>$:	Average hydrodynamic radius
$R_{vv}(\theta)$:	Rayleigh ratio with vertically polarized incident and scattered light at scattering angle θ
S_r:	Shear rate
t:	Extension ratio of polymers
T:	Absolute temperature
U:	Voltage potential
v:	Flow velocity
$v_{x:}$	Flow velocity along x-axis
v_y:	Flow velocity along y-axis
v_z:	Flow velocity along z-axis
α:	polarizability; expansion factor; depth parameter of square well
β:	Coherence factor
ε:	dielectric constant
Φ:	Distribution function of end-to-end distance
η:	Viscosity of the solvent
λ_0:	Wavelength of light in vacuum
θ:	Scattering angle
ρ:	Density

σ:	The internal concentration
Γ:	Characteristic linewidth
ξ:	correlation length of one blob

Chapter 1

Introduction and Background

1.1 Brief Overview of Polymers Passing through Nanopores

Transport of polymers through membrane channels is ubiquitous, either in industry[1] such as water purification, or in biology.[2] For example, RNA transport through cell nuclear pore is central for further gene expression as presented in Figure 1.1. Hence the study of polymer chains translocation through nanopores is one of the most interesting research focuses in polymer chemistry, physics and the biophysics. Lots of computer simulations[3-6] and experiments[7-11] investigations have been carried out for the translocation mechanism study to understand the concerns of polymer chain properties such as stiffness, chain length, chain topologies, nanopores diameters and the possible interaction between the polymer chain and the pore wall. Basically, when the polymer chains are smaller than the pores, the polymer chains can just diffuse through the pore, simply by Brownian motion, just like dialysis, and this is certainly not what we concern in our study. Instead, we are interested in how polymer chains with characteristic size larger than the nanoscale pore pass through a nanopore. Such a translocation process can be realized by external forces, such as electric force and hydrodynamic force. Strong affinity between the polymer chains and the pore wall can also greatly facilitate such a translocation.

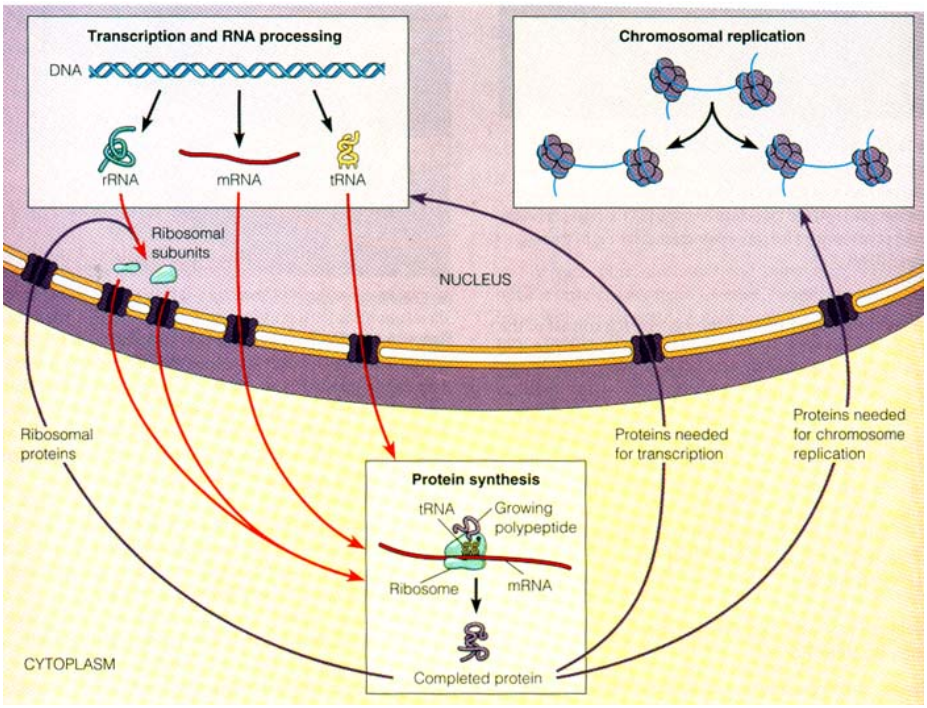

Figure 1.1. Scheme for the biopolymers transport across the cell nuclear pore during the gene expression.

1.1.1 Polymer passing through nanopores under electric field

The studies on the polymer translocation through a nanopore under electric field are based on the principles of Coulter counter, which measures the conductance changes when polymer chains or particles move across an opening. In these experiments, a membrane with a biological or synthetic pore is placed between two electrolyte solutions and a constant trans-membrane electric potential is applied. The passage of a charged chain or particle through a small pore by an electric force leads to a transient current decrease because of its excluded volume. With fast electronics and sensitive detection, each translocation event can be recorded with a higher time resolution so that its structure and translocation dynamics could be evaluated.

In the absence of specific chemical interactions between analytes and the channel itself, there are four possible transport mechanisms that can contribute the velocity of a particle through the channel of a Coulter counter. They are velocities arising from pressure-driven flow (v_{PD}), electrophoresis (v_{EP}), electroosmosis (v_{EO}), and diffusion (v_D). Compared with the electrophoresis, the diffusional transport is negligible and the particle velocities can be expressed as:

$$v = v_{PD} + v_{EP} + v_{EO} = \frac{a^2}{\eta l}\Delta P + \frac{\mu}{l}U + \frac{\varepsilon\xi}{\eta l}U \tag{1-1}$$

where η, ΔP, U, μ, ε, ξ are the solution viscosity, pressure and voltage across the channel, electrophoretic mobility of the particle, solution dielectric constant, zeta-potential of the channel surface, respectively. The current reduction is related with the polymer chain or particle size and can be simply estimated by:

$$I_B(d) = 1 - (\frac{a}{d})^2 \tag{1-2}$$

where d is the diameter of the nanopore and a is the effective diameter of the cross section of the polymer chain or a particle.

Although this method was established early in 1953, the application of Coulter counter is not extended sufficiently until the well-defined smaller nanopores becomes available, and the achievement of faster electronic devices and data acquisition. The first trail for the single polymer translocation detection with a nanopore was carried out in 1994,[7] for the counting of neutral polymer PEG passing through a natural channel formed by peptides, which was incorporated in the suspended bilayer lipid. Later in 1996, single stranded DNA, for the first time, was used by Kasianowicz[9] in a similar system to purse a "distant dream" of single-base DNA sequencing simply based on electric current discrimination for different bases. Ever since then, investigations for on the polymer translocation have an explosive increasing. And solid state small nanopores with diameter as smaller as 2 nm[12] also fabricated to complement the biological protein nanopores, as presented in Figure 1.2. In the past few years, it has been tried to discriminate bases of nucleic-acid,[13-15] probe local structure of DNA,[10, 16, 17] RNA[18] and proteins;[19] and measure forces required to unzip a nucleic acid or rupture a DNA-protein or RNA-protein complex[20, 21]. So far, most of these studies are focused on the short polymer chain translocation. And it has been found that the transloation dynamics for a long polymer chain through the nanopore can be quite complicated, considering into the size discrepancy of diameter of the polymer chain cross section and that of the nanopore, and the possible interaction between the polymer chain and the pore wall.

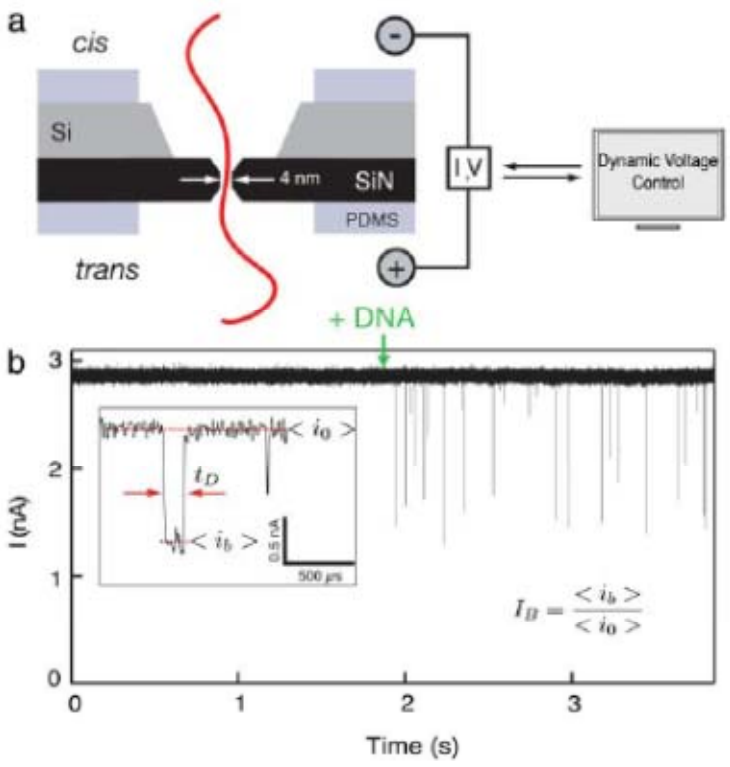

Figure 1.2. Nanopore-based DNA analysis. Voltage applied to the salt solution through Ag/AgCl electrodes drives a flow of ions through the nanopore. Charged molecules are also driven though the pore, modifying the ion flux as they pass through, which can be measured as changing current through the ammeter. The size where DNA is added is typically referred to as cis, with the other side trans.[17]

Here we would like to present two examples for such a complex translocation dynamics of polymer chains through different nanopores.[22, 23] Figure 1.3 present the translocation dynamic of a synthetic linear anionic poly(styrenesulfonic acid) (PSS) chains through an α-hemolysin protein channel, embedded in a lipid bilayer which is suspended on a glass nanopore membrane. Unlike the usually found rectangular current shape for DNA translocation events, there is major type of events with distinct bi-level current blockades with a shallow block level at current decrease of ~60%, followed by a deep block level with current decrease of ~85%. The shallow block is corresponding to the chain staying in vestibule of the pore without translocation, while the deep block is corresponding to the real translocation process. And increasing the applied voltage decreases the duration time of chain translocation

through the pore, while increases the characteristic time of the PSS within the vestibule.

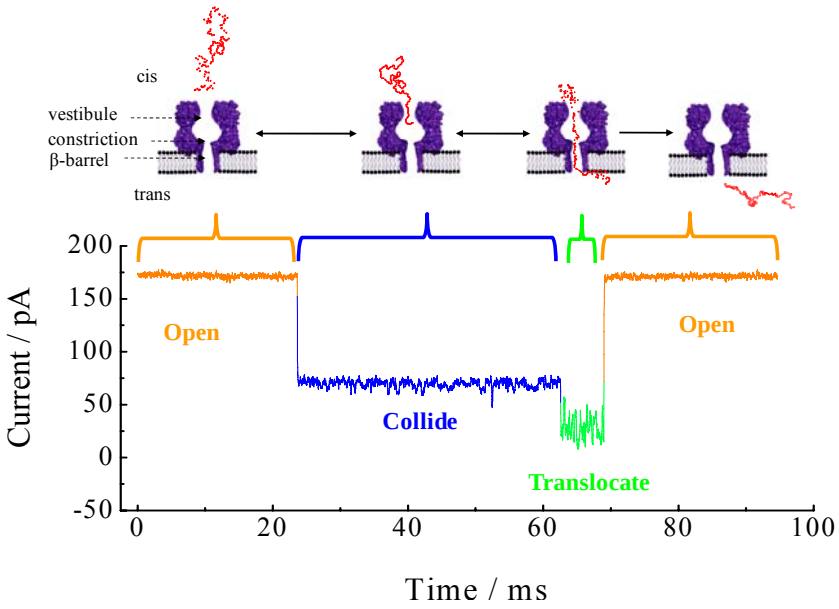

Figure 1.3. Model of the interaction of a PSS chain (136500 g/mol) with α-hemolysin protein pore and the corresponding translocation event current traces.[22]

Another example is for the long supercoiled plasmid DNA chains passing through conical glass nanopores shown in Figure 1.4.[23] The transport dynamics of individual supercoiled DNA chains through the nanopores are quite distinct with different opening. For larger pores, they can pass through the conical glass capillary without much stretching; namely, the current pulse has a typical triangle shape and its half-height duration time decreases, but its occurring frequency (f) increases exponentially, as V increases. For a smaller tip opening, f strangely increases and then decreases with an increasing V. And each current pulse composes of four steps as follows. 1) I sharply decreases from its baseline (I_o) when a DNA chain approaches the tip opening and inserts a segment to block the pore; 2) The inserted segment is stretched under the electric field gradient so that the pore is less blocked, resulting in a slight current increase; 3) then I slightly decreases once more, indicating that the pulling of the inserted segment is faster than the relaxation (unwinding) of the rest of the chain outside so that it clogs at the tip entrance; and 4)

I gradually increases and finally returns to I_o because more and more segments are gradually pulled in by the electrical field until the entire chain slips through the conical glass capillary. These steps can be well explained in terms of a big difference between times of pulling the first segment inside the tip and relaxing the rest segments outside.

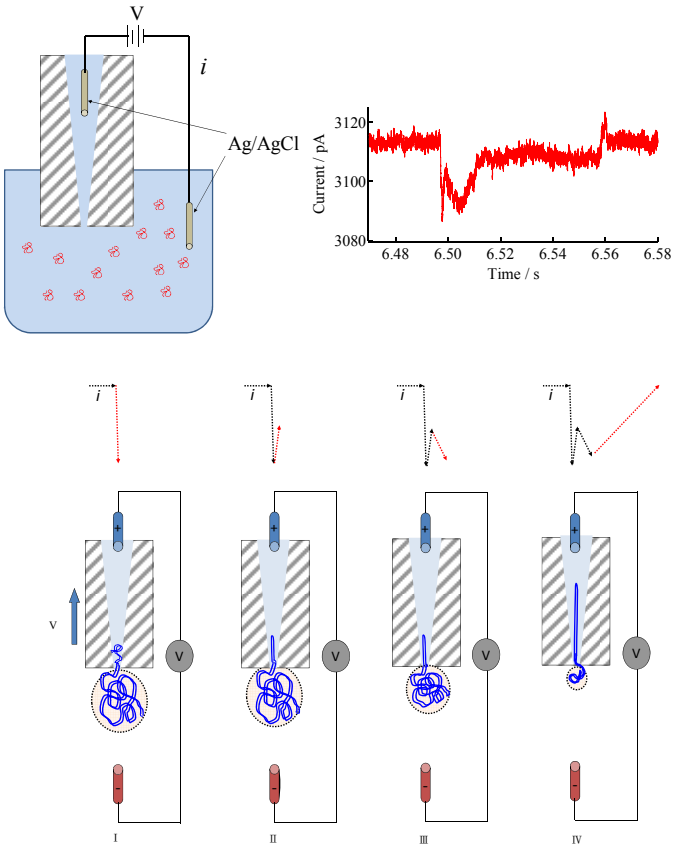

Figure 1.4. Schematic of translocation dynamics of a supercoiled plasmid DNA chain through a small conical glass capillary under a high applied voltage and their corresponding current response based on Figure 3E. [23]

Despite of the enormous investigation and large number of the fancy publications based on the resistive pulse method of the polymer chain translocation through nanopores, such a method also suffers drawbacks. The polymer chains has to be charged so that they can be driven by the electric force and the solution medium is only limited to the aqueous solution, which should be conductive to provide electric current information during the translocation event. On the other hand, since the

method is only based on single nanopore, the efficiency for further application of analytes separation is really low. So the pressure driven polymer chain translocation attracts more and more attentions.

1.1.2 Polymer passing through nanopores under flow field

Studies on polymer chains passing through nanopores under flow have been intensively investigated from 50 years ago to now. In comparison, theory in this aspect is much advanced than its experimental findings. Peterlin[24, 25] brought forward a critical strain-rate should exist for polymer chain expansion under elongational flow in 1966. Later de Gennes[26, 27] refined it as a so called "coil-stretching" transition and claimed such transition was a first-order transition. Then Pincus[28] described the transition was a process of stretching polymer chains into strings of blobs. Following these, various simulation studies on stretching of polymer chains under flow filed have been reported based on the development of computer technique and theoretical improvement.[6, 29-31] Experimentally, Anderson and his associates[32-36] have made significant contribution in this research area. However, the "first order transition" of polymer chain under flow field only have been experimentally proved in our lab until recently.[37]

Compared with coil-stretching transition of polymer chains, the expansion of polymers with more complicated architectures are more intricate. Other chain conformations such as stars,[2, 27, 38-40] comb-like polymers[41] and branch polymers[27, 42] have been investigated both theoretically and experimentally. However, up to now, there is still no prediction for how polymeric soft particles, such as polymeric micelles and micro-gels are deforming under a sufficiently strong elongation flow field.

1.1.2.1 Shear flow field

For simplicity, we only discuss shear flow with a constant velocity gradient tensor. When polymer chains are under weaker shear rate, there was a linear relationship between distortion and reduced shear $\tau_Z S_r$ by birefringernce,[43] as shown by

Janeshitz-Kriegl. Here S_r is the shear rate and τ_Z is the largest relaxation time of the unperturbed molecule based on Zimm model. Such argument has been widely used in the polymer melt rheology.[44]

When polymer chains are under strong shear rate, the Peterlin approximations were used to estimate the conformation hysteresis in the shear flow.[24-26] The associated current contains three contributions: drift in the external velocity field $v=S_r r$, motion under the restoring force F, and Brownian motion with a diffusion coefficient D.

$$q = \Phi \mathbf{S}_r \mathbf{r} + D[(\Phi/\mathrm{T})F - \nabla\Phi] \tag{1-3}$$

where Φ is the distribution function of end-to-end distance.

Considering a random coil under strong shear flow, only the outer segments are directly exposed to the flow field, the exposure degree will increase as the increasing of the shear flow, then the chain will be more distorted and more monomers are exposed to the shear, resulting in further chain extension and exposure. Details of such feedback are dependent on different flow field. For a two-dimensional flow (v_x, v_z) described by the vorticity $\omega=½(\partial v_x/\partial z-\partial v_z/\partial x)$ and pure deformation rate $A=½(\partial v_x/\partial z+\partial v_z/\partial x)$, the coil-to-stretch transition is a second order transition as shown in Figure 1.5.

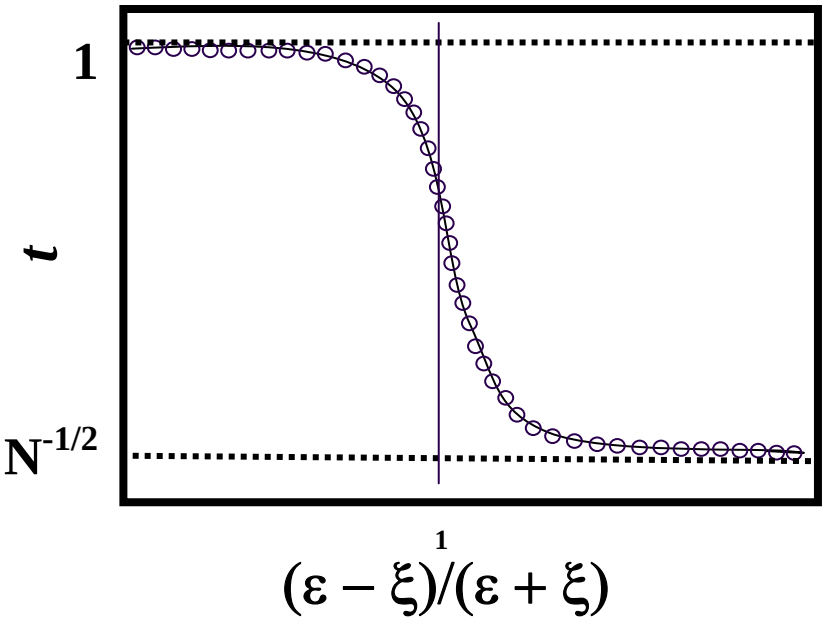

Figure 1.5. The coil to stretched transition of a polymer chain in

vorticity[26]

When a polymer chain is under a flow with longitudinal gradients (e.g., $v_x = S_x, v_z = -S_z$), the t(Sr) shows a S shape, indicating a bistable equilibrium in Figure 1.6. And there is one critical value of S = Sr*, at which a chain will switch from coil to stretch, with a first order transition.

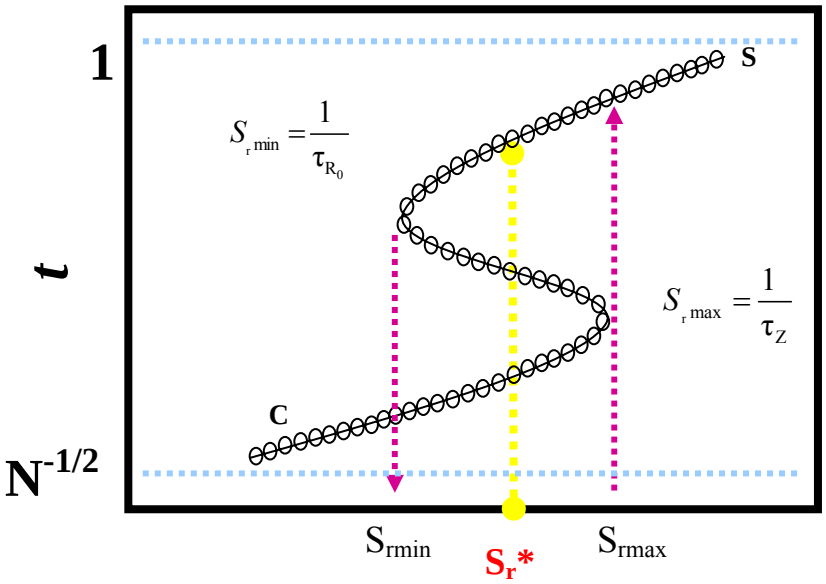

Figure 1.6 The coil to stretched transition of a polymer chain in a "longitudinal gradient", the $S_{rmin} = 1/\tau_R$ and $S_{rmax} = 1/\tau_z$ is order of Rouse and Zimm frequency, respectively.[26]

1.1.2.2 Polymer chains with different topologies

The possibility for a polymer chain to automatically pass through a cylindrical pore with a diameter of D much smaller than its size is extremely low because of the extra confinement penalty. However, an external force such as hydrodynamic force in the elongational flow can pull the chain through the small nanopore when the hydrodynamic force overcomes the confinement force. There have been many well established theories for predicting the relation between the minimum force (critical flow rate q_c) and the chain's topology and deformability as well as the pore size.[26-28] And in particular, de Gennes[26] and Pincus[28] showed that for a flexible linear polymer chain, $q_{c,linear} \sim k_B T/\eta$, independent on the polymer chain length and the pore size, where k_B, T and η are the Boltzmann constant, absolute temperature and solution

viscosity, respectively. Our previous study on linear polystyrene chains passing through the pore confirmed that $q_{c,linear}$ is indeed independent of the chain length (Figure 1.7) but decreases as D increases.[45] And the reason behind is explained as follows: chain segment inside the each "blob" should not be treated as a hard sphere and a parameter of l_e is further introduced, describing the effective length along the flow direction. Then, the critical flow rate is rewritten as[37, 45]

$$q_{c,linear} = \frac{k_B T}{3\pi\eta} \frac{D}{l_e} \tag{1-4}$$

with l_e scaled to D as $D = kl_e^{\alpha}$ with k, a solution dependent constant and $1/2 \leq \alpha \leq 3/5$, varying with the solution quality. Such a scaling argument was recently supported by the first principles calculation.[46, 47]

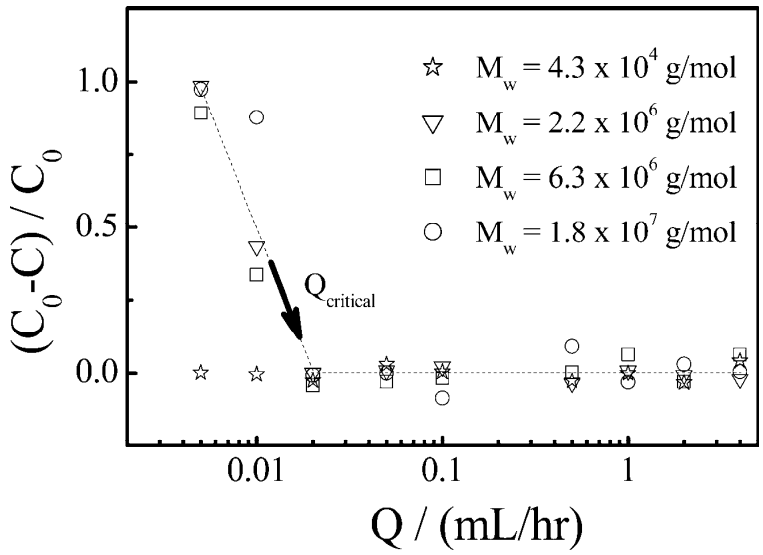

Figure 1.7. Macroscopic flow rate (Q) dependence of retention concentration of different molecular weights PS linear chains in cyclohexane at $T = 34.5$ °C.[45]

Later the ultrafiltration behaviors of regular star-like polymer chains through small cylindrical pore are also studied.[48] Star polystyrene chains with arm length (L_A) and arm numbers (f) are synthesized by coupling the living polystyrene anionic chains with crosslinker divinylbenzene (DVB). It is found that the critical flow rate ($q_{c,star}$) dramatically increases with f but is nearly independent of L_A for a given f, contradictory to the de Gennes' prediction, in which the full extension of each

pulled-in arm was assumed.[27] Instead, it is found that $q_{c,star}$ is simply related to the number of forwarded arms inside the pore (f_{in}), i.e.

$$\frac{q_{c,star}}{q_{c,linear}} = \frac{f + |f - 2f_{in}|}{2} \tag{1-5}$$

It can result in two cases as shown in Figure 1.8. Namely, when $1 \le f_{in} \le f/2$, $q_{c,star} = f_{out}\, q_{c,star}$ while $f/2 \le f_{in} \le f$, $q_{c,star} = f_{in}\, q_{c,star}$ with the minimum $q_{c,star}$ at $f_{in} = f/2$.

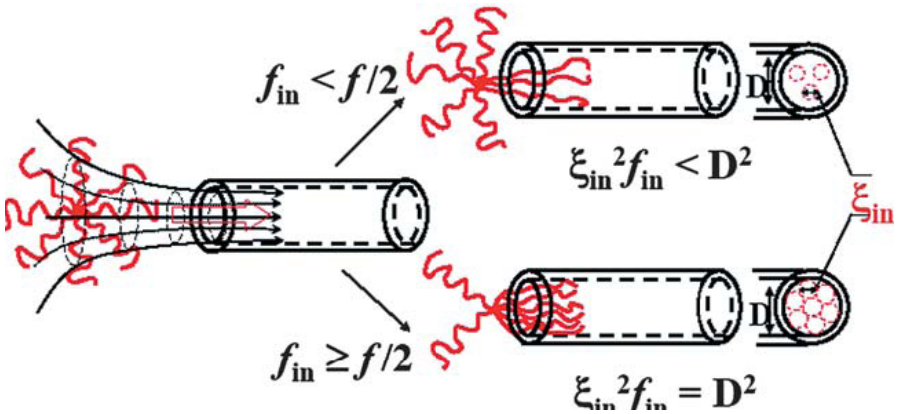

Figure 1.8. Schematic of how a star chain enters a nanopore under two different situations; namely, $1 \le f_{in} \le f/2$ and $f/2 \le f_{in} \le f$.[48]

Recently, we further studied the ultrafiltration of hyperbranched chains, which is much more complicated because a hyperbranched chain can be either weakly or strongly confined inside a pore, depending on both the blob (ξ) and the subchain length (l_s).[42] The "defect-free" hyperbranched polystyrenes with uniform and long subchains are prepared from seesaw-type linear macromonomers, azide~~alkyne~~azide by click chemistry, where ~~ represents a polystyrene chain. It is revealed that $q_{c,branch}$ is dependent on both polymerization degrees of the entire chain and subchain (N_t, and N_b); namely, $q_{c,branch} \sim N_t^{\gamma} N_b^{\varphi}$.

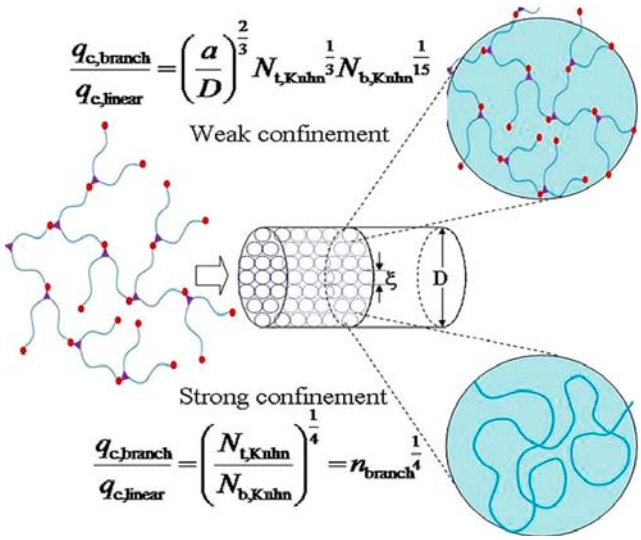

Figure 1.9. Schematic of weak and strong confinements of a hyperbranched chain inside a small cylindrical pore with a diameter D, where each small circle represents a blob with a size of ξ.[42]

1.1.2.3 Polymeric micelles

Block copolymer would like to self-assemble into micelles in a selective solvent at concentration above the critical micelle concentration (CMC) and the solvophobic blocks aggregate due to hydrophobic interaction, to form the micellar core while the soluble blocks protrude into the solution. For polymeric micelles with a size much larger than a nanopore, only one or few soluble blocks ("arms") could enter the pore with no flow or under a low flow rate. In this case, such a micelle must be stuck at the pore entrance, schematically shown in Figure 1.10. Previous studies described each lyophilic block as a polymer chain tethered on the lyophilic/lyophobic interface with a stretched conformation and made of a string of small correlated blobs.[49-51] Under an elongation flow, the Stocks hydrodynamic force for each blob is $\eta v\zeta$, where η, v and ζ are the solvent viscosity, the flow velocity and the blob size, respectively. The hydrodynamic force (F_h) on each lyophilic arm is the sum of the total hydrodynamic force on all the blobs in one arm, i.e., ηvH, where H is the length of the arm along the flow direction and v equals the flow rate (J) divided by the cross-section area of the pore (D^2). If such a polymeric micelle is not deformable under a force stronger than the interaction among the insoluble blocks inside the core,

individual chains would be pulled out of the micelle, pass the pore and then reassemble at the other side. Based on this assumption, for the first time, the hydrodynamic force that is required to rupture each polymeric micelle and pull individual block copolymer chains out is estimated by in situ studying the flow-rate dependent retention of polymeric core-shell micelles in a selective solvent through small pores (20 nm) in an ultra-filtration experiment in Figure 1.11.[52] It is also revealed that both lengths of the soluble and insoluble blocks strongly affect $f(F_h)$. If the insoluble PS block is too long or the soluble PI block is too short, polymeric micelles cannot be disintegrated even under the fastest flow (200 mL/hr) available in our current set-up.

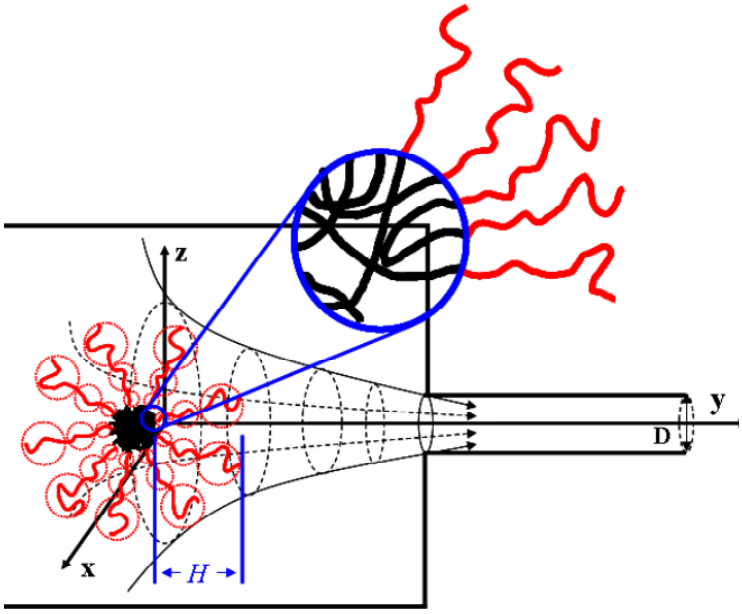

Figure 1.10. Schematic of ultrafiltration of a polymeric core-shell micelle made of a block copolymer chains through a smaller pore under an elongational flow. The enlarged picture shows different kinds of chain packing of insoluble blocks in the core.[52]

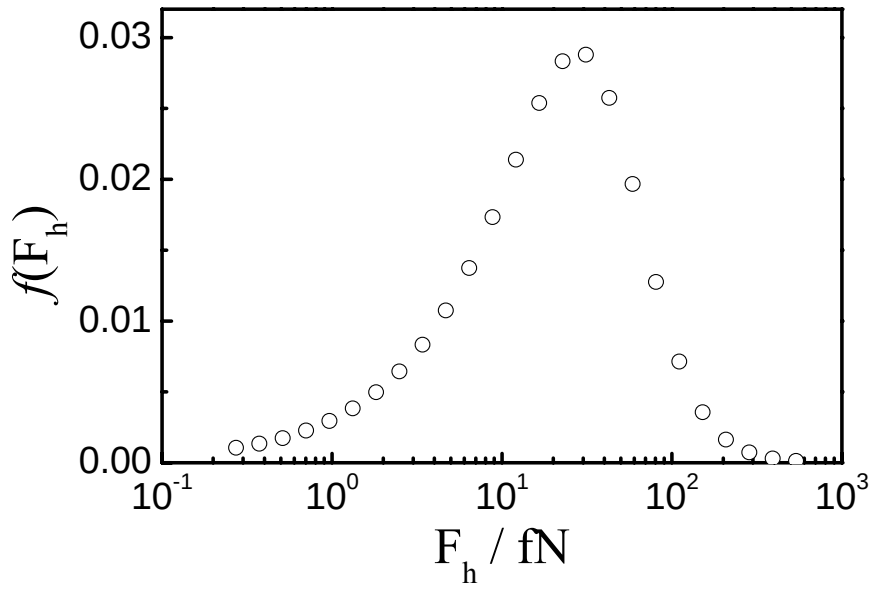

Figure 1.11. Distribution of hydrodynamic force ($f(F_h)$) required to rupture polymeric micelles made of $(St)_{180}$-*b*-$(Iso)_{500}$ in n-hexane at 25.0 ^{o}C.[52]

1.2 Brief Overview of Block Copolymers

Block copolymers are macromolecules composed of sequences, or blocks of chemically distinct repeat units. Those blocks are generally immiscible, leading to a microphase separation.[53-55] Block copolymers are also called polymeric surfactants. Since the different blocks are covalently linked, the microphase separation is spatially limited and results in self-assembled structures with characteristic sizes of 10-100 nm. Enormous interesting in the research of block copolymers ranges from development of new and facile synthetic strategies, macromolecular chemistry and physics, self-assembly in bulk and in solution, to their applications in materials science, surface science as well as biomedicines and biomimics.[53]

By definition, the architectures of the block copolymers can be as simple as linear AB diblock, and as complex as Super H-Shaped A_5BA_5, and the different block copolymer architectures can be realized by different synthesis strategies. Figure 1.12 shows some typical architectures of block copolymers.

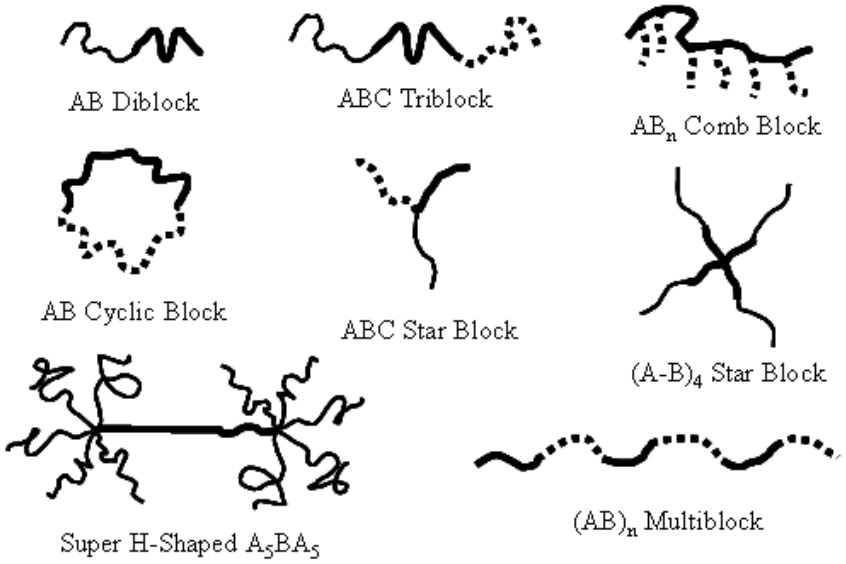

Figure 1.12. Schematic illustration of some typical architectures of block copolymers.

1.2.1 Synthesis of block copolymers

The synthesis of block copolymers has been studied extensively and general overviews can be found elsewhere in the literature. Here we only discuss several most used techniques for the preparation of block copolymers, including the sequential anionic polymerization, ATRP, RAFT, coupling reaction.

Sequential anionic polymerization

Sequential anionic polymerization has been the most used technique for the preparation of well-defined block copolymers. Since its discovery by Szwarc[56] in 1956, a large variety of block copolymers were prepared from styrene, dienenes, methacrylates, oxiranes, thiiranes, lactones, cyclic siloxanes.[57] Typical examples of such block copolymers are PS-poly(dinene) di- and triblock, PS-PVP, PPO-PEO, PS-PAA as hydrophilic –hydrophobic copolymers, acrylic copolymers and many others. The initiation step is typically achieved using alkyl lithium species such as *sec*- or *n*-butyl-lithium and propagation steps proved to be "living" under suitable conditions. More detail will be further discussed in Chapter 2.

The main limitation in the synthesis of block copolymers by anionic polymerization is that it is applicable to a limited number of monomers and that the

relative reactivity of the monomers has to be taken into account for the sequential addition. Specifically, functional monomers, e.g. monomers having hydroxyl, mercapto, carbonyl, etc. groups cannot be polymerized, because of the side reactions of these active hydrogen with either the initiator or the living chain end. And to overcome these problems, suitable protection of these functional groups should be involved, which increases the difficulty and steps.

Atom transfer radical polymerization (ATRP)

ATRP originates from a widely used reaction in organic synthesis known as atom transfer radical addition (ATRA).[58-60] In this synthesis technique, halogen atom transfers from an organic halide to a transition metal complex occurs to activate organic radicals, which can attack vinyl group by addition reaction and then quickly deactivated by back-transfer of the halogen atom from the transition metal to the organic radical species. The ATRP is the extension of ATRA to polymerization. The comparison of the mechanism of ATRA and ATRP is shown in Figure 1.13.

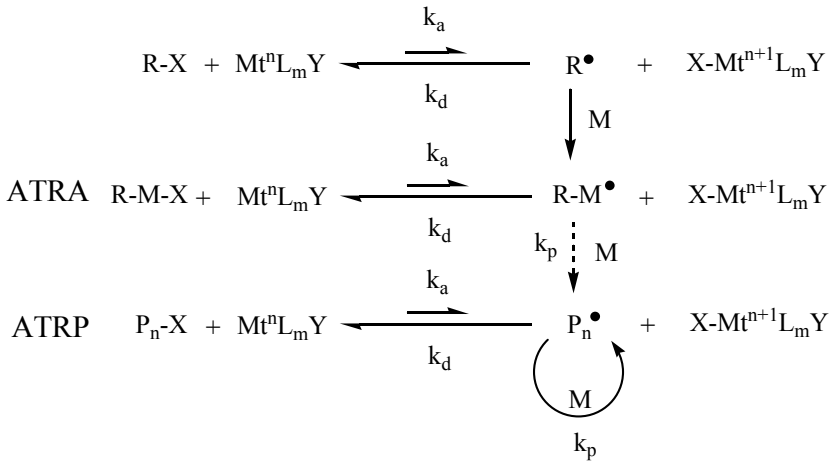

Figure 1.13 Comparison of ATRA and ATRP mechanism.[60]

The catalyst is key important to ATRP since it determines the atom transfer equilibrium and the kinetics of exchange between the dormant and active species.[61] The efficient ATRP catalyst consists of a transition metal species (M_t^n) which can expand its coordination sphere and increase its oxidation number, a complexing ligand (L), and a counterion which can form a covalent or ionic bond with the metal center. The transition metal complex (M_t^n/L) is responsible for the homolytic

cleavage of an alkyl halogen bond R-X which generates the corresponding higher oxidation state metal halide complex $M_t^{n+1}X/L$ and an organic radical $R^{\bullet}$. The $R^{\bullet}$ can then propagate with vinyl monomer, terminate as in conventional free radical polymerization by either coupling or disproportionation, or be reversibly deactivated in this equilibrium by $M_t^{n+1}X/L$ to form a halide-capped dormant polymer chain. Complexes of Cu have been found to be the most efficient catalysts in the ATRP of a broad range of monomers in diverse media. Additionally, the dynamic equilibrium between dormant species and propagating radicals can be easily and appropriately adjusted for a given system by modifying the complexing ligand of the catalyst.[60, 62] Commonly employed N-based ligands used in conjunction with Cu/ATRP catalysts include derivatives of bidentate: bipyridine (bpy) and pyridine imine; tridentate: diethylenetriamine (DETA), and tetradentate tris(2-aminoethyl)amine (TREN) and tetraazacyclotetradecane (CYCLAM) among many other multidentate ligands. The counterion is very often a halide ion.

A variety of monomers have been successfully polymerized using ATRP. Typical monomers include styrenes, (methy)acrylates, acrylates, (meth)acrylamides, and acrylonitrile. Shortly after the discovery of ATRP, it was recognized that the wide variety of monomers, conservation of end groups, and control over molecular weights and polydispersities could facilitate the synthesis of block copolymers. The first example was the synthesis of polystyrene-*b*-poly(methyl acrylate). Since then, a wide variety of diblock, triblock or tetrablock copolymers have been successfully accomplished by sequential monomer addition or post-polymerization modification. One typical example is shown in Figure 1.14, the synthesis of PtBuA-*b*-PS-*b*-PMA reported by Matyjaszewski and coworkers.[63]

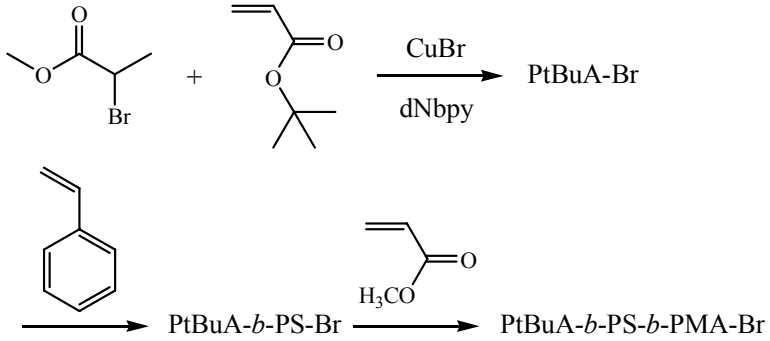

Figure 1.14. Synthesis of ABC triblock copolymer by ATRP.[63]

Reversible addition–fragmentation chain transfer polymerization (RAFT)

RAFT with dithioesters invented by Ezio Rizzardo is successful because the rate constant of chain transfer is faster than the rate constant of propagation.[64, 65] Analogous to ATRP, the polymer chains spend the majority of the reaction time in the dormant state and are only activated for a short period of time. The RAFT agents are stabilized dithio compounds, which contain a small molecule capable of initiating a polymer chain. After homolytic cleavage to release the initiator, the RAFT agent can reversibly deactivate the polymer chains resulting in a level of control over the polymerization. Exchange reactions in this technique are also very fast, leading to well controlled systems.

The mechanism of RAFT is shown in Figure 1.15.[66] Successful application of the RAFT process requires the appropriate selection of a RAFT reagent for a particular monomer. Various dithioesters, dithiocarbamates, trithio- carbonates and xanthates have been effectively used as transfer agents to control molecular weights, molecular weight distributions, and even molecular architecture, as shown in Figure 1.16. RAFT is among the most successful controlled radical polymerization processes due in large to its applicability to a wide range of monomers. It has high tolerance to functional monomers and also no demanding reaction conditions for the polymerizations.[67]

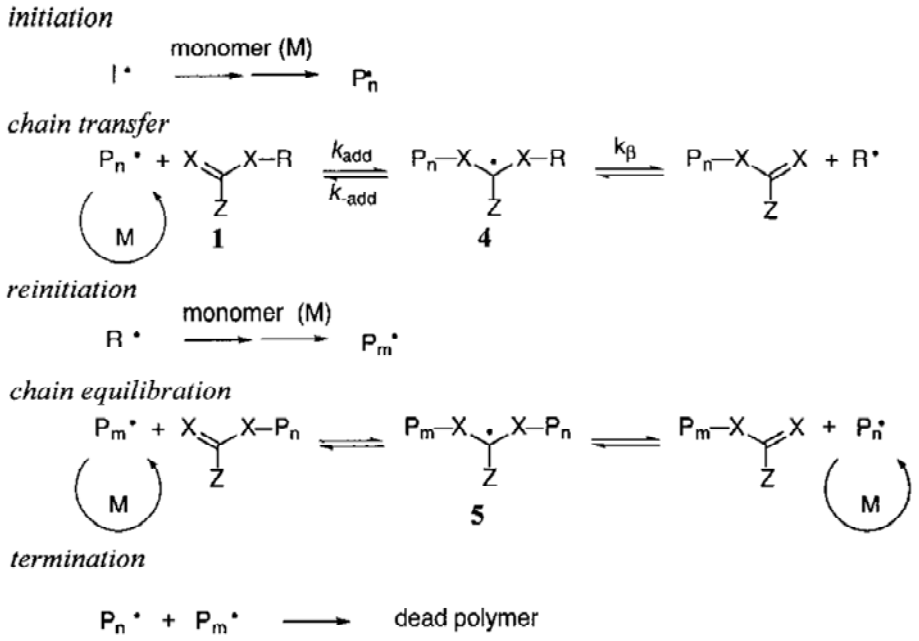

Figure 1.15. The mechanism of RAFT polymerization.[66]

Several different types of block copolymers have been synthesized using RAFT technique. The versatility of RAFT is shown by the preparation of AB type block copolymer with a variety of monomer pairs, such as styrene with *n*-butyl acrylate or *N,N'*-dimethylacrylamide, methyl methacrylates with styrene, *N*-isopropylacrylamide with acrylic acid et al..[68, 69] RAFT can be used directly incorporate acrylic and methacrylic acid into block copolymers without extra protection, which cannot yet be accomplished using ATRP system. ABA type block copolymers polystyrene-*b*-poly(*n*-butyl acrylate)-*b*-polystyrene was synthesized based on trithiocarbonate, a difunctional chain transfer agent.[70]

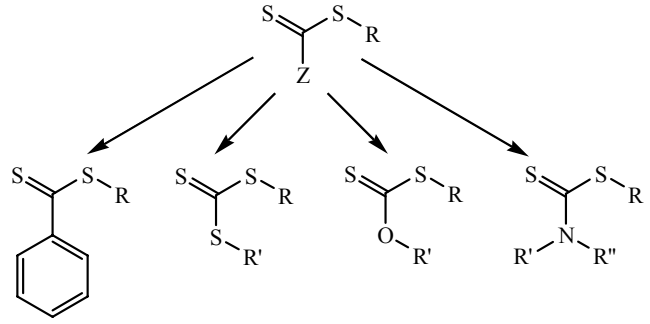

Figure 1.16. General structures of RAFT agents with different functional groups on the Z position: dithioester, xanthate, trithiocarbonate and dithiocarbamate.

Coupling methods

In this method, blocks with different chemical composition are synthesized first, and then are coupled together by the functional group attached to the end of the polymer blocks *via* condensation polymerization mechanism. A variety of di- and tri block copolymers are prepared in this procedure. Click chemistry has been used as a highly efficient reaction to couple two distinct linear polymers to make block copolymers.[71] Linear homopolymers of methyl methacrylate and styrene, for which α-alkynyl or ω-azido functionalities are incorporated from an alkynyl-functionalized initiator or from chain-end modification, are found to undergo high-yielding Cu(I)-catalyzed dipolar cycloaddition reactions to produce block copolymers.[72]

1.2.2 Molecular characterization of block copolymers

After synthesis, the average molecular weight and block composition, as well as molecular and compositional homogeneity of the block copolymers are essential. Possible further detailed characterization methods include nuclear magnetic resonance spectroscopy (NMR), infrared spectroscopy (IR) and UV spectroscopy for the molecular structure and chemical composition determination and size exclusion chromatography (SEC) or gel permeation chromatography (GPC), static light scattering (SLS), membrane osmometry for molecular weight and molecular weight distribution determination. The principles for each of the characterization method will not be discussed here. However the NMR, GPC, and static LLS characterization for the specific block copolymer we used in our study will be further discussed in the next Chapter.

1.2.3 Block copolymers self-assembly in solution (equilibrium state)

When dissolved in a selective solvent, good for one block, but poor for another, the block copolymers can undergo self-assembly into micelle aggregates in order to minimize the energetically unfavourable solvophobic interactions between the one block and the solvent.[73, 74] The various reported morphologies including spheres,[75] cylinders,[76] vesicles[77] and more complex flower-like and multicompartment structures[78, 79] are primarily a result from the inherent molecular curvature and is

mainly governed by a force balance among the core block attraction, the corona block repulsion, and the core–corona interfacial tension.[80] Over the last few decades, the micelle morphological transitions in solutions have been realized by changing the block copolymer composition,[81-84] polymer concentration,[85] solvent composition[86] and temperature,[87, 88] or by the addition of homopolymer.[89]

Spherical micelles are the simplest with hydrodynamic radius 10-50nm. Triblock copolymer PEO-PPO-PEO can self-assemble into spherical micelles with hydrodynamic radius of 10 nm at 40 ^{o}C.[90] Generally, the density of the spherical micelle core is larger than the density of the micelle shell with micelle overall $<R_g>/<R_h>$ less than 0.774. Other more sophisticated spherical micelles, such as shell cross-linked micelles,[91] and multicompartmental 'hamburger' micelle[79] are also reported recently.

Block copolymer cylindrical (or worm-like) micelles have also been widely reported. Such one dimensional structures have unique properties for biological system.[92, 93] For example, filomicelles can function as nano-carrier to effectively deliver the anticancer drug with long circulation time and sustained drug release.[93] Compared to shortened cylinders with end-defect, infinitely long cylinders are energetically favorable, since long cylinders allow uniform curvature across the entire aggregate. However, on the other hand, the formation of defects such as end caps (more energetically favorable) and branch points (less energetically favorable) are also entropically favorable.[94] Further, the wide array of intramolecular and intermolecular interactions within block copolymer assemblies generates even more sophisticated structures. For example, linear triblock copolymer PAA-PMA-PS has been reported to form toroids[95] as well as multicompartment one dimensional nanostructures[96] in solution, and in each case the driving force for structure formation appears to be minimization of the end cap energy.

Polymeric vesicles (polymersomes) are most common observed bilayer-type structures generated through copolymer self-assembly[77, 97]. Compared to the low molecular counterpart, i.e., the liposomes, polymersomes show higher stability and a higher designable permeability. Such polymer vesicles could be potentially used in

fields such as drug delivery,[98] nanoreactors as well as biological functional models.

Here we would like to present few examples for the diblock copolymer self-assembly in solution. Eisenberg and his coworkers[77, 80, 99-102] investigated the morphologies of poly(styrene-*b*-acrylic acid) (PS-*b*-PAA) ionic diblock copolymers in solvent mixtures of water and dioxane. By varying block compositions, water content in the mixture solvent and the copolymer concentration, very systematic phase diagrams have been established in Figure 1.17.

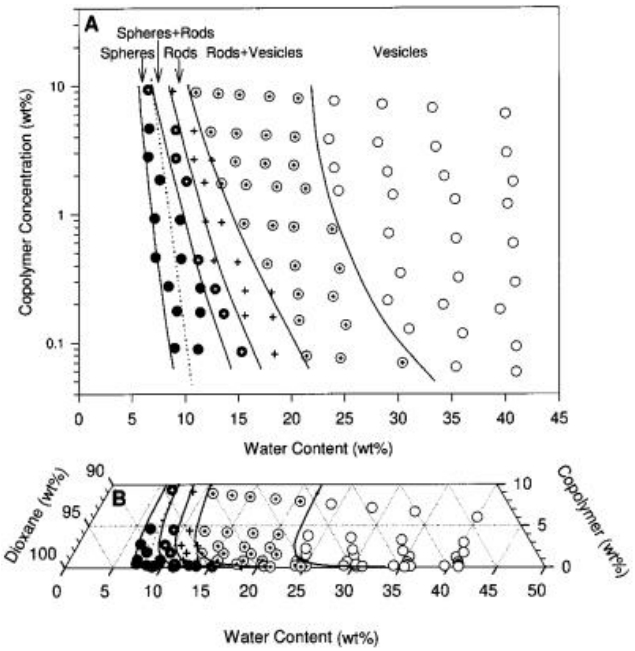

Figure 1.17. Phase diagram of the block copolymer PS_{310}-PAA_{52} in dioxane/H_2O mixture.[102]

On the other hand, Bates and co-workers[94] used poly(butadiene-*b*-ethylene oxide) (PB-*b*-PEO) diblock copolymer to demonstrate that much more complicated micro-structures, including Y junctions and three-dimensional networks in water in addition to the conventional spherical, wormlike and vesicle micelles can be observed. Fragmentation of the network produces a non-ergodic array of complex reticular aggregates based on the cryogenic TEM images. They also showed that a molar mass PB-*b*-PEO can form gigantic wormlike micelles at low concentration in water. More importantly, they found that subsequent generation of free radicals with a conventional water-based redox reaction leads to chemical cross-linking of the PB

core without disrupting the cylindrical morphology, as evidenced by small-angle neutron scattering experiments and also by cryo-TEM.[76] These wormlike rubber micelles exhibit unusual viscoelastic properties in water.

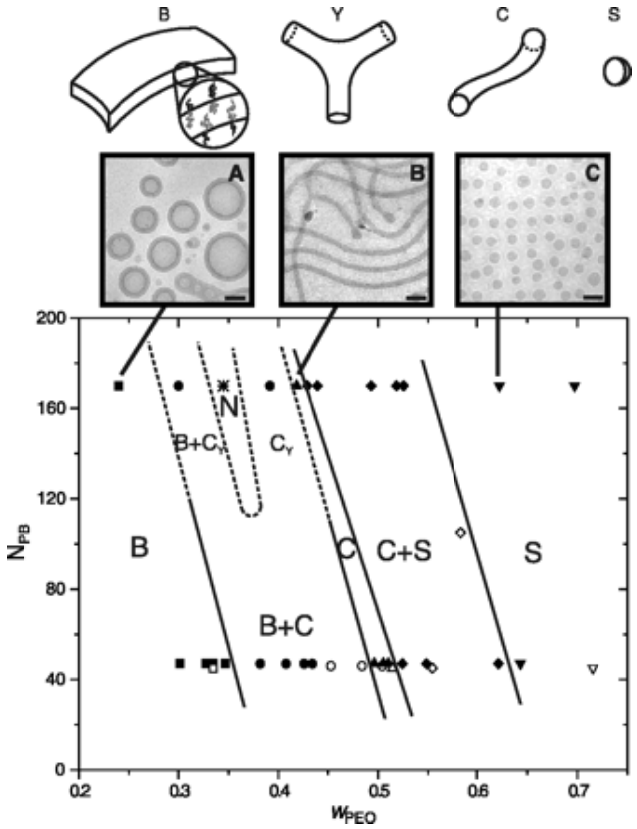

Figure 1.18. Morphology diagram for PB-PEO in water as a function of molecular size and composition.[94]

1.2.4 Block copolymers self-assembly in solution (non-equilibrium state)

We have previously discussed that by changing the block copolymer composition, structures, polymer concentration, solvent composition, and temperature, or by the addition of homopolymer, different micelle morphologies transition can be obtained. And those variables can be summarized as the thermodynamic parameters under equilibrium state. On the other hand, some methods by controlling the kinetic factors can also lead to various morphologies. Shear rate has been proved effective to induce possible morphology transformation not only for small molecule surfactants,[103-106] but also for the polymeric surfactants.[107-110] Winnik's group[107] found the spherical hybrid micelles with QDs aggregated to form stable wormlike networks under rapid stirring. More recently, Moffitt and coworkers[108] produced variable flow-induced

morphologies including cylinders, Y-junctions, bilayers and networks by a mechanism of collision-coalescence enabled by strong and localized on-chip shear fields in a gas-liquid microfluidic reactor, where exclusively spherical morphology are found for the off-chip condition in Figure 1.19. Those morphologies should be only kinetically trapped intermediate states, but not globally equilibrated or thermodynamically favorable.

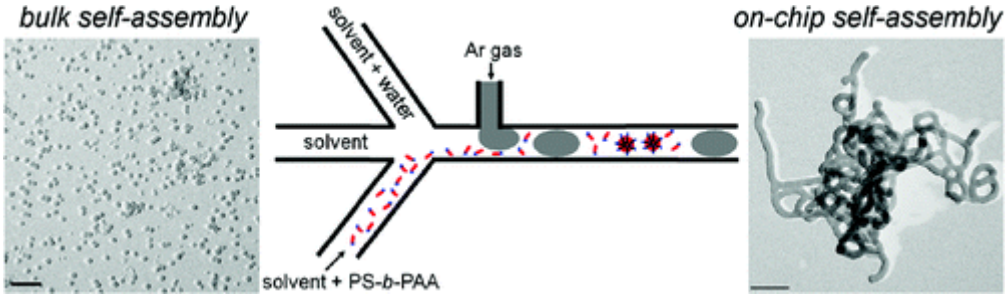

Figure 1.19. Scheme for the flow-induced morphology transition from spherical micelles to non-spherical micelles in microfluidic reactor.[108]

Slow crystalline process of core block is another case of kinetically controlling of micelle structures. An excellent example is the work in Winnik's and Manners's group based on block copolymers with polyferroceylsilane (PFS) core blocks.[111-114] When at temperature lower than melting point of PFS block, the block copolymers tend to form cylindrical micelles. And remarkably if further amount of dissolved PFS-based block copolymers was added to the precrystallized "seed" micelles, the original cylindrical micelles can grow a distinct component from the ends of the existing micelles.[113] The whole process are named "living propagation" of cylindrical micelles. Nanoprecipitation-induced polymer assemblies are another example of the bottom up methods and such technique can even be extended to obtain homopolymers nanostructures. We will not further discuss about the details here.

1.3 Research Objectives and Achievements

Understanding the macromolecular translocation mechanism through nanopores is important not only for the biological gene expression, but also for the industrial applications of fractionation and separation of macromolecules with different conformations. In principle, macromolecular chains with different conformations and configurations have distinct critical flow rate to pass through a nanopore, so by choosing a flow rate in between, it is practical to separate the macromolecular chains simply by a flow experiment. With great advances in membrane science, studies on polymer chains with different conformations such as star and branch passing through nanopores in a flow are recently reported.[42, 48] We also successfully separated a mixture of linear and star-like chains by choosing a flow rate between $q_{c,star}$ and $q_{c,linear}$, and a mixture of hyperbranched chains with similar molecular weight but different subchain length molecular weight at a flow rate between their $q_{c,branch}$. With the above achievements in the ultrafiltration of the polymer chains, we want to further extend the macromolecular chains to soft polymeric particles, such as micelles and microgels to see how they are deforming under a flow. We have previous reported that polymeric micelles from short insoluble block and long soluble block can pass through a nanopore in a flow, while that from long insoluble block and short soluble block cannot be disintegrated even under a sufficiently strong flow. After adding common solvent THF to swell the spherical polymeric micelles, we accidently find a sphere-to-cylinder transition from the nanopore extrusion of the swollen spherical micelles (in Chapter 3 and 4). The swelling of the spherical micelles with different THF content has been carefully studied using a combination of laser light scattering and transmission electron microscopy techniques. The following generation of wormlike nanofibers from the nanopore extrusion of block copolymer micelles is confirmed with different techniques. And it is also found that these wormlike micelles undergo unexpected slow fragmentation after extrusion over few days before turning to their original spherical phase.

In Chapter 5, to understand such a sphere-to-cylinder transition induced by

nanopore extrusion mechanism, we further investigated the effects of block copolymer composition, solvent quality (swelling of polymeric micelles) and extrusion flow rate. The sphere-to-cylinder transition extent can be estimated by I_0/I_∞, where I_0, and I_∞ are the scattering intensity for the micelle solution soon after extrusion and that are thermodynamically stable spherical micelles solution long time after extrusion. In addition, we also monitored the hydraulic pressure drop across the nanopore during the nanopore extrusion. Based on these studies, we basically understand how those spherical micelles are transformed into long cylindrical micelles in the nanopore extrusion. The trapping and further shell-crosslinking with the vinyl group in polyisoprene are also discussed.

In Chapter 6, we quantitatively investigated the slow cylinder-to-sphere dissociation kinetics by light scattering and electron microscopy. Both techniques show the weight-average length of the nanofibers (L_w) after extrusion decreases with dissociation. The change of time-dependent length distribution (f(L)) and L_w were compared with those calculated ones on the basis of end-scission, random-scission and Gaussian-scission models. The results reveal that the cylinder-to-sphere transition involves a combination of 1) the Gaussian- scission model with a preference in the middle of a long cylinder and a Gaussian distributed probability at other sites; and 2) the end-scission model with a preferred higher scission rate constant at the two ends of each cylinder. Our results also reveal that the scission rate constant is nearly a linear function of L but slightly increases with time for a given length.

In Chapter 7, the nanopore-extrusion induced sphere-to-cylinder transition is applied to fabricate 1D hybrid long metal nanoparticle/block copolymer cylindrical micelles. Small gold nanoparticles was pre-coated with thiol terminated polystyrene and then further encapsulated inside block copolymer spherical micelles by a precipitation method. By controlling the weight ratio of Au/polymer, the average nanoparticles number per micelles can be varied. This method is also applicable for producing multifunctional cylindrical micelles comprising different nanoparticle species, such as gold nanoparticles, quantum dots and magnetic nanoparticles.

1.5 References and Notes

(1) Zeman, L. J.; Zydney, A. L., *Microfiltration and Ultrafiltration: Principles and Applications*. New York, 1996; Vol. Marcel Dekker.

(2) Fox, M. E.; Szoka, F. C.; Frechet, J. M. J., *Acc. Chem. Res.* **2009,** 42, 1141-1151.

(3) Aksimentiev, A., *Nanoscale* **2010,** 2, 468-483.

(4) Muthukumar, M.; Kong, C. Y., *Proc. Natl. Acad. Sci. USA* **2006,** 103, 5273-5278.

(5) Meller, A., *J. Phys. Condens. Matter* **2003,** 15, R581-R607.

(6) Slonkina, E.; Kolomeisky, A. B., *J. Chem. Phys.* **2003,** 118, 7112-7118.

(7) Bezrukov, S. M.; Vodyanoy, I.; Parsegian, V. A., *Nature* **1994,** 370, 279-281.

(8) Bezrukov, S. M.; Vodyanoy, I.; Brutyan, R. A.; Kasianowicz, J. J., *Macromolecules* **1996,** 29, 8517-8522.

(9) Kasianowicz, J. J.; Brandin, E.; Branton, D.; Deamer, D. W., *Proc. Natl. Acad. Sci. USA* **1996,** 93, 13770-13773.

(10) Meller, A.; Nivon, L.; Branton, D., *Phys. Rev. Lett.* **2001,** 86, 3435-3438.

(11) Movileanu, L.; Cheley, S.; Bayley, H., *Biophys. J.* **2003,** 85, 897-910.

(12) Dekker, C., *Nat. Nanotechnol.* **2007,** 2, 209-215.

(13) Meller, A.; Nivon, L.; Brandin, E.; Golovchenko, J.; Branton, D., *Proc. Natl. Acad. Sci. USA* **2000,** 97, 1079-1084.

(14) Ashkenasy, N.; Sanchez-Quesada, J.; Bayley, H.; Ghadiri, M. R., *Angew. Chem. Int. Ed.* **2005,** 44, 1401-1404.

(15) Stoddart, D.; Heron, A. J.; Mikhailova, E.; Maglia, G.; Bayley, H., *Proc. Natl. Acad. Sci. USA* **2009,** 106, 7702-7707.

(16) Maglia, G.; Restrepo, M. R.; Mikhailova, E.; Bayley, H., *Proc. Natl. Acad. Sci. USA* **2008,** 105, 19720-19725.

(17) Wanunu, M.; Sutin, J.; McNally, B.; Chow, A.; Meller, A., *Biophys. J.* **2008,** 95, 4716-4725.

(18) Butler, T. Z.; Gundlach, J. H.; Troll, M. A., *Biophys. J.* **2006,** 90, 190-199.

(19) Wang, H. Y.; Ying, Y. L.; Li, Y.; Kraatz, H. B.; Long, Y. T., *Anal. Chem.* **2011,** 83, 1746-1752.

(20) Hornblower, B.; Coombs, A.; Whitaker, R. D.; Kolomeisky, A.; Picone, S. J.; Meller, A.; Akeson, M., *Nat. Methods* **2007,** 4, 315-317.

(21) Wanunu, M.; Bhattacharya, S.; Xie, Y.; Tor, Y.; Aksimentiev, A.; Drndic, M., *ACS Nano* **2011,** 5, 9345-9353.

(22) Chen, Q. J.; Liu, J.; Schibel, A. E. P.; White, H. S.; Wu, C., *Macromolecules* **2010,** 43, 10594-10599.

(23) Chen, Q. J.; Diao, S.; Wu, C., *Soft Matter* **2012,** 8, 5451-5458.

(24) Peterlin, A., *J. Polym. Sci. Part B: Polym. Lett.* **1966,** 4, 287-291.

(25) Peterlin, A., *Pure Appl. Chem.* **1966,** 12, 563-586.

(26) de Gennes, P. G., *J. Chem. Phys.* **1974,** 60, 5030-5042.

(27) de Gennes, P. G., *Adv. Polym. Sci.* **1999,** 138, 91-105.

(28) Pincus, P., *Macromolecules* **1976,** 9, 386-388.

(29) Kolomeisky, A. B.; Slonkina, E., *Biophys. J.* **2003,** 84, 95a-95a.

(30) Piguet, F.; Foster, D. P., *J. Chem. Phys.* **2013,** 138.

(31) Sung, W.; Park, P. J., *Phys. Rev. Lett.* **1996,** 77, 783-786.

(32) Quinn, J. A.; Anderson, J. L.; Ho, W. S.; Petzny, W. J., *Biophys. J.* **1972,** 12, 990-1007.

(33) Anderson, J. L.; Quinn, J. A., *Biophys. J.* **1974,** 14, 130-150.

(34) Malone, D. M.; Anderson, J. L., *Aiche J.* **1977,** 23, 177-184.

(35) Long, T. D.; Anderson, J. L., *J. Polym. Sci. Part B: Polym. Phys.* **1984,** 22, 1261-1281.

(36) *J. Polym. Sci. Part B: Polym. Phys.* **1985,** 23, 191-197.

(37) Jin, F.; Wu, C., *Phys. Rev. Lett.* **2006,** 96.

(38) Ripoll, M.; Winkler, R. G.; Gompper, G., *Phys. Rev. Lett.* **2006,** 96.

(39) Ripoll, M.; Winkler, R. G.; Gompper, G., *Eur. Phys. J. E* **2007,** 23, 349-354.

(40) Ge, H.; Pispas, S.; Wu, C., *Polymer Chemistry* **2011,** 2, 1071-1076.

(41) Gay, C.; Raphael, E., *Adv. Colloid Interf. Sci* **2001,** 94, 229-236.

(42) Li, L. W.; He, C.; He, W. D.; Wu, C., *Macromolecules* **2012,** 45, 7583-7589.

(43) Janeshitz-Kriegl, H., *Adv. Polym. Sci.* **1969,** 6, 170.

(44) Lodge, T. P.; Lodge, S. A., *Rheologica Acta* **1992,** 31, 32-43.

(45) Ge, H.; Jin, F.; Li, J. F.; Wu, C., *Macromolecules* **2009,** 42, 4400-4402.

(46) Freed, K. F.; Wu, C., *Macromolecules* **2011,** 44, 9863-9866.

(47) Freed, K. F.; Wu, C., *J. Chem. Phys.* **2011,** 135.

(48) Ge, H.; Pispas, S.; Wu, C., *Polym. Chem.* **2011,** 2, 1071-1076.

(49) Birshtein, T. M.; Zhulina, E. B., *Polymer* **1989,** 30, 170-177.

(50) Halperin, A.; Tirrell, M.; Lodge, T. P., *Adv. Polym. Sci.* **1992,** 100, 31-71.

(51) Zhulina, E. B.; Adam, M.; LaRue, I.; Sheiko, S. S.; Rubinstein, M., *Macromolecules* **2005,** 38, 5330-5351.

(52) Hong, L. Z.; Jin, F.; Li, J. F.; Lu, Y. J.; Wu, C., *Macromolecules* **2008,** 41, 8220-8224.

(53) Hadjichristidis, N. P., S.; Floudas, G., *Block Copolymers: Synthetic Strategies, Physical Properties, and Applications*. John Wiley & Sons, Inc., Hoboken, New Jersey: 2003.

(54) Hamley, I. W., *The Physics of Block Copolymers*. Oxford University Press: New York, 1998.

(55) Lazzari, M. L., G.; Lecommandoux, S., *Block Copolymers in Nanoscience*. WILEY-VCH Verlag GmbH & Co. KGaA: 2006.

(56) Szwarc, M. L., M.; Milkovich, R., *J. Am. Chem. Soc.* **1956,** 78, 2556-2657.

(57) Riess, G. H., G.; Bahadur, P., *Encyclopedia of Polymer Science and Engineering*. Wiley: New York, 1985; Vol. 2.

(58) Wang, J. S.; Matyjaszewski, K., *Macromolecules* **1995,** 28, 7901-7910.

(59) Matyjaszewski, K., *Chem-Eur. J.* **1999,** 5, 3095-3102.

(60) Matyjaszewski, K.; Xia, J. H., *Chem. Rev.* **2001,** 101, 2921-2990.

(61) Braunecker, W. A.; Matyjaszewski, K., *Prog. Polym. Sci.* **2007,** 32, 93-146.

(62) Patten, T. E.; Matyjaszewski, K., *Acc. Chem. Res.* **1999,** 32, 895-903.

(63) Davis, K. A.; Matyjaszewski, K., *Macromolecules* **2001,** 34, 2101-2107.

(64) Chiefari, J.; Chong, Y. K.; Ercole, F.; Krstina, J.; Jeffery, J.; Le, T. P. T.; Mayadunne, R. T. A.; Meijs, G. F.; Moad, C. L.; Moad, G.; Rizzardo, E.; Thang, S. H., *Macromolecules* **1998,** 31, 5559-5562.

(65) Mayadunne, R. T. A.; Rizzardo, E.; Chiefari, J.; Chong, Y. K.; Moad, G.; Thang, S. H., *Macromolecules* **1999,** 32, 6977-6980.

(66) Moad, G.; Chiefari, J.; Chong, Y. K.; Krstina, J.; Mayadunne, R. T. A.; Postma, A.; Rizzardo, E.; Thang, S. H., *Polym. Int.* **2000,** 49, 993-1001.

(67) Perrier, S.; Takolpuckdee, P., *J. Polym. Sci. Part A: Polym. Chem.* **2005,** 43, 5347-5393.

(68) Chong, Y. K.; Le, T. P. T.; Moad, G.; Rizzardo, E.; Thang, S. H., *Macromolecules* **1999,** 32, 2071-2074.

(69) Schilli, C. M.; Zhang, M. F.; Rizzardo, E.; Thang, S. H.; Chong, Y. K.; Edwards, K.; Karlsson, G.; Muller, A. H. E., *Macromolecules* **2004,** 37, 7861-7866.

(70) Mayadunne, R. T. A.; Rizzardo, E.; Chiefari, J.; Krstina, J.; Moad, G.; Postma, A.; Thang, S. H., *Macromolecules* **2000,** 33, 243-245.

(71) Opsteen, J. A.; van Hest, J. C. M., *Chem. Commun.* **2005**, 57-59.

(72) Tsarevsky, N. V.; Sumerlin, B. S.; Matyjaszewski, K., *Macromolecules* **2005,** 38, 3558-3561.

(73) Riess, G., *Prog. Polym. Sci.* **2003,** 28, 1107-1170.

(74) Zhulina, E. B.; Borisov, O. V., *Macromolecules* **2012,** 45, 4429-4440.

(75) Bang, J.; Jain, S.; Li, Z.; Lodge, T. P.; Pedersen, J. S.; Kesselman, E.; Talmon, Y., *Macromolecules* **2006,** 39, 1199-1208.

(76) Won, Y. Y.; Davis, H. T.; Bates, F. S., *Science* **1999,** 283, 960-963.

(77) Discher, D. E.; Eisenberg, A., *Science* **2002,** 297, 967-973.

(78) Moughton, A. O.; Hillmyer, M. A.; Lodge, T. P., *Macromolecules* **2012,** 45, 2-19.

(79) Groschel, A. H.; Schacher, F. H.; Schmalz, H.; Borisov, O. V.; Zhulina, E. B.; Walther, A.; Muller, A. H. E., *Nature Commun,* **2012,** 3.

(80) Zhang, L. F.; Eisenberg, A., *Polym. Adv. Techol.* **1998,** 9, 677-699.

(81) Zhang, L.; Eisenberg, A., *Science* **1995,** 268, 1728-1731.

(82) Zhang, L.; Eisenberg, A., *J. Am. Chem. Sci.* **1996**, 3168-3181.

(83) Jain, S.; Bates, F. S., *Science* **2003,** 300, 460-464.

(84) Zhulina, E. B.; Adam, M.; LaRue, I.; Sheiko, S. S.; Rubinstein, M., *Macromolecules* **2005,** 38, 5330-5351.

(85) Zhang, L.; Eisenberg, A., *Macromolecules* **1999**, 2239-2249.

(86) Bang, J.; Jain, S.; Li, Z.; Lodge, T. P.; Pedersen, J. S.; Kesselman, E.; Talmon, Y., *Macromolecules* **2006,** 39, 1199-1208.

(87) LaRue, I.; Adam, M.; Pitsikalis, M.; Hadjichristidis, N.; Rubinstein, M.; Sheiko, S. S., *Macromolecules* **2006,** 39, 309-314.

(88) Bhargava, P.; Tu, Y.; Zheng, J. X.; Xiong, H.; Quirk, R. P.; Cheng, S. Z. D., *J. Am. Chem. Sci.* **2007,** 129, 1113-1121.

(89) Ouarti, N.; Viville, P.; Lazzaroni, R.; Minatti, E.; Schappacher, M.; Deffieux,

A.; Borsali, R., *Langmuir* **2005,** 21, 1180-1186.

(90) Alexandridis, P.; Hatton, T. A., *Colloids Surfaces A: Physicochem. Eng. Aspects* **1995,** 96, 1-46.

(91) Read, E. S.; Armes, S. P., *Chem. Commun.* **2007**, 3021-3035.

(92) Bhirde, A. A.; Patel, V.; Gavard, J.; Zhang, G. F.; Sousa, A. A.; Masedunskas, A.; Leapman, R. D.; Weigert, R.; Gutkind, J. S.; Rusling, J. F., *ACS Nano* **2009,** 3, 307-316.

(93) Geng, Y.; Dalhaimer, P.; Cai, S.; Tsai, R.; Tewari, M.; Minko, T.; Discher, D. E., *Nat. Nanotechnol.* **2007,** 2, 249-255.

(94) Jain, S.; Bates, F. S., *Science* **2003,** 300, 460-464.

(95) Pochan, D. J.; Chen, Z. Y.; Cui, H. G.; Hales, K.; Qi, K.; Wooley, K. L., *Science* **2004,** 306, 94-97.

(96) Cui, H. G.; Chen, Z. Y.; Zhong, S.; Wooley, K. L.; Pochan, D. J., *Science* **2007,** 317, 647-650.

(97) Bang, J.; Jain, S.; Li, Z.; Lodge, T. P.; Pedersen, J. S.; Kesselman, E.; Talmon, Y., *Macromolecules* **2006,** 39, 5583-5583.

(98) Ding, J. F.; Liu, G. J., *J. Phys. Chem. B* **1998,** 102, 6107-6113.

(99) Zhang, L.; Eisenberg, A., *Science* **1995,** 268, 1728-1731.

(100) Zhang, L.; Eisenberg, A., *J. Am. Chem. Soc.* **1996**, 3168-3181.

(101) Zhang, L.; Eisenberg, A., *Macromolecules* **1999**, 2239-2249.

(102) Shen, H. W.; Eisenberg, A., *J. Phys. Chem. B* **1999,** 103, 9473-9487.

(103) Rehage, H.; Wunderlich, I.; Hoffmann, H., *Progr. Colloid & Polym. Sci.* **1986,** 59, 51-59.

(104) Turner, M. S.; Cates, M. E., *J. Phys. Condens. Matter* **1992,** 4, 3719-3741.

(105) Keller, S. L.; Boltenhagen, P.; Pine, D. J.; Zasadzinski, J. A., *Phys. Rev. Lett.* **1998**, 2725-2728.

(106) Vasudevan, M.; Buse, E.; Lu, D. L.; Krishna, H.; Kalyanaraman, R.; Shen, A. Q.; Khomami, B.; Sureshkumar, R., *Nature Mater.* **2010,** 9, 436-441.

(107) Zhang, M.; Wang, M. F.; He, S.; Qian, J. S.; Saffari, A.; Lee, A.; Kumar, S.; Hassan, Y.; Guenther, A.; Scholes, G.; Winnik, M. A., *Macromolecules* **2010,** 43, 5066-5074.

(108) Wang, C. W.; Sinton, D.; Moffitt, M. G., *J. Am. Chem. Soc.* **2011,** 133, 18853-18864.

(109) Rychkov, I., *Macromol. Theory Simul.* **2005,** 14, 207-242.

(110) Yu, H. Z.; Jiang, W., *Macromolecules* **2009,** 42, 3399-3404.

(111) Wang, X. S.; Arsenault, A.; Ozin, G. A.; Winnik, M. A.; Manners, I., *J. Am. Chem. Soc.* **2003,** 125, 12686-12687.

(112) Wang, X. S.; Liu, K.; Arsenault, A. C.; Rider, D. A.; Ozin, G. A.; Winnik, M. A.; Manners, I., *J. Am. Chem. Soc.* **2007,** 129, 5630-5639.

(113) Wang, X. S.; Guerin, G.; Wang, H.; Wang, Y. S.; Manners, I.; Winnik, M. A., *Science* **2007,** 317, 644-647.

(114) Rupar, P. A.; Cambridge, G.; Winnik, M. A.; Manners, I., *J. Am. Chem. Soc.* **2011,** 133, 16947-16957.

Chapter 2
Principle of Laser Light Scattering and Methods

In the classical theory of light scattering an incident electromagnetic field exerts a force on the charges in the scattering volume. These accelerating charges then radiate light. When visible light is incident upon the medium, the atoms in a subregion of the illuminated volume, small compared to the cube of the incident light wavelength, see essentially the same incident electric field. If many subregions of equal size are considered, the scattered electric field is the superposition of the scattered fields from each of them. If the subregions are optically identical, that is, each has the same dielectric constant; there will be no scattered light in other than the forward direction. However, if the regions are optically different, that is, have different dielectric constants, then the amplitudes of the light scattered from the different subregions are no longer identical and complete cancellation will no longer take place, thus there will be scattered light in other than the forward direction. From the kinetic theory, it is known that molecules are constantly translating and rotating so that the instantaneous dielectric constant of a given region will fluctuate and thus give rise to light scattering.[1]

Based on the light scattering, various radiations can be used as incident such as X-Rays, Neutrons, Electrons as well as the Laser light, which are classified by their wavelength range. The name “laser” is an acronym for “light amplification by stimulated emission of radiation”, which bearing some unique properties such as single wavelength and coherence. When laser light is incident on a dilute macromolecule solution or suspension of colloidal particles which bearing different refractive index from that of the solvent, the incident light can be scattered by each illuminated macromolecule or colloidal particle in all directions.[1, 2] The scattered light waves from different macromolecules or particles mutually interfere, or combine, at a distant, fast photomultiplier tube (PMT) or avalanche-photodiode (APD) detector and produce a net scattered intensity I(t) or photon counts n(t) which is not uniform on the detection plane. Consider all the macromolecules or particles are stationary, the scattered light intensity for fixed direction would be a constant i.e., independent of time. However, in reality, because of the thermal energy of kT, there will always be fluctuation of densities or concentrations, which will further

contribute to the fluctuations of I(t) with time. Such fluctuation rates can be related to different relaxation processes such as translational and rotational diffusions as well as internal motions or slow motions of the macromolecules in the solution. The faster the relaxation process, the faster the intensity fluctuations will be.

In a broad definition, laser light scattering (LLS) could be classified as inelastic (e.g., Raman, fluorescence, and phosphorescence) and elastic (no absorption) light scattering. However, in polymer and colloid science, light scattering is normally referred to in terms of static (elastic) or dynamic (quasi-elastic) measurements, or both, of the scattered light.[2] Static LLS as a classical and absolute analytical method measures the angular distribution of time-average scattered intensity. On the other hand, dynamic LLS measures the intensity fluctuations instead of the average light intensity, and its essence may be explained as follows. When the incident light is scattered by a moving macromolecule or particle, the detect frequency of the scattered light will be slightly higher or lower than that of the original incident light owing to the Doppler effect, depending on whether the particle moves towards or away from the detector. Thus, the frequency distribution of the scattered light is slightly broader than that of the incident light. This is why dynamic LLS is also called quasi-elastic light scattering (QELS). The frequency broadening ($\approx 10^5$-10^7 Hz) is so small in comparison with the incident light frequency ($\approx 10^{15}$ Hz) so that it is very difficult to detect the broadening directly in the frequency domain. However, it can be effectively recorded in the time domain through a time correlation function. For this reason, dynamic light scattering is sometimes known as intensity fluctuation spectroscopy. If we use digital photons to measure the intensity fluctuations, the term photon correlation spectroscopy (PCS) is then used to refer to the technique described here.

The first experimental studies on light scattering were carried out by Tyndall. He observed the scattering of the natural light when it passed through a colloid dispersion. In 1881, based on Maxwell theory of electromagnetic field, Rayleigh derived that the intensity of the scattered light by the non-absorption, non-interaction and optically isotropic small particles is reversely proportional to the fourth power of the incident wavelength. In 1944, Debye measured the molecular weight of macromolecules from dilute solution using light scattering method. Later, Zimm[3] proposed the famous Zimm plot by extrapolating both concentration and angular angle to zero value at a single coordinate. Since then, light scattering, strictly, static light scattering as a classical and

absolute analytical method has been widely used to characterize both synthetic and natural macromolecules. However, light scattering at that time was limited in measuring scattered intensity at different angles and concentration, from which three parameters of macromolecules, namely the weight-average molecular weight (M_w), z-average root-mean-square radius of gyration ($<R_g^2>^{1/2}$, simply R_g) and the second-order virial coefficient (A_2) can be obtained. This situation was changed in the 1960s with the invention of laser. In 1964, Cummins[4] first reported using lasers as source of incident radiation for the study of macromolecular solutions, poly(styrene), and during the last two decades, thanks to the advance of stable laser, ultrafast electronics and personal computers, LLS, especially dynamic LLS has evolved from a very special instrument for physicists and physical chemists to a routine analytical tool in polymer laboratories.[5, 6] Commercially available research-grade LLS instruments are normally capable of making static and dynamic measurements simultaneously for studies of colloidal particles in suspension or macromolecules in solution as well as in gels and viscous media.

2.1 Static Laser Light Scattering

2.1.1 Scattering by a small particle

When an electromagnetic wave enters the isotropic particle which is suspended in vacuum, polarization will be induced in the direction of the electric field of the incident wave. (Figure 2.1) The polarization, which oscillates with the same frequency as the incident light serves as a broadcasting station that emits a second radiation in all directions. When the particle is much smaller than the wavelength of the incident light λ_o (in practice, smaller than $\lambda_o/20$), the electric field of the incident light

$$\vec{E} = \overrightarrow{E_0} \exp[i(2\pi\nu t - \phi)] \tag{2-1}$$

is homogeneous within the particle; dipole moment induced to be $\vec{\mu} = \alpha\vec{E}$. The electric field oscillates with frequency ν and so does the induced dipole. When the electric field is not too strong, the induced dipole is proportional to the field:

$$\vec{\mu} = \alpha\vec{E} = 4\pi\varepsilon_0\alpha'\vec{E} \tag{2-2}$$

here α' is the polarizability tensor of the particle and ε is dielectric coefficient at vacuum.

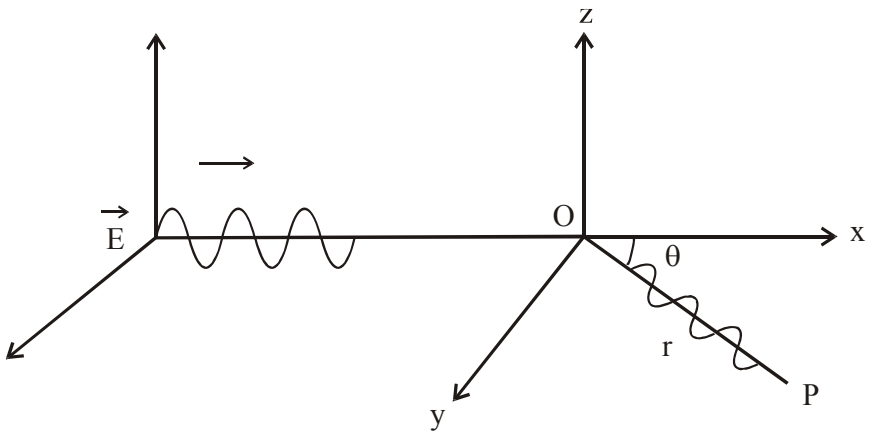

Figure 2.1 Three dimensional coordinates where origin o represents a scatter and P is observation point at xoy plane. The vertically polarized incident beam causes polarization in the scatter, which radiates into different direction.

According to Maxwell electromagnetic equations, the electric field generated by the oscillating dipole at point p with distance *r* from origin o and angle of θ from the incident light is

$$\overrightarrow{E_s} = \frac{d^2\vec{p}/dt^2}{4\pi\varepsilon_0 rc^2} = \frac{d^2(\overrightarrow{\mu_0}+\vec{\mu})/dt^2}{4\pi\varepsilon_0 rc^2} = -\frac{4\pi^2\alpha'}{r\lambda_0^2}\vec{E} \qquad (2\text{-}3)$$

where *c* is the velocity of light in vacuum and α' is the polarizability volume. $\vec{p}$ is the total dipole of the particle, i.e., the summation of the permanent $\overrightarrow{\mu_0}$ and the induced dipole $\vec{\mu}$. Since $\overrightarrow{\mu_0} << \vec{\mu}$ at room temperature and $\overrightarrow{\mu_0}$ is independent of high frequency electromagnetic field, we have adopted $d^2\vec{p}/dt^2 = d^2\vec{\mu}/dt^2$ in equation (2-3). Thus, the time-average scattered intensity *i* (kJ·m^{-2}·s^{-1}) of the particle at point p is

$$i_s = \varepsilon_o c\left\langle E_s^2 \right\rangle = \frac{16\pi^4\alpha'^2}{\lambda_0^4 r^2}(\varepsilon_o c < E^2 >) = \frac{16\pi^4\alpha'^2}{\lambda_0^4 r^2} I_o \qquad (2\text{-}4)$$

where I_o is the intensity of primary light. Equation (2-4) shows that the scattered intensity is proportional to the square of molecular weight since for particles made from a given isotropic material, α' is proportional to their molecular weight. On the other hand, $i_s / I_0 \propto \lambda_0^{-4}$, means that the scattering is much stronger for light of a

shorter wavelength. This explains why the sky is blue because the scattering is stronger toward the short-wavelength end of the visible spectrum.

2.1.2 Scattering by a single polymer chain

Because of the interference of beams scattered by different part of the large molecule, the scattering by a long polymer chain is stronger. The scattered field of the whole particle at point p is the superposition of the electric field of all N' units:

$$\overrightarrow{E_s} = \sum_{l=1}^{N'} \overrightarrow{E_{s,l}} = -\frac{4\pi^2}{\lambda_0^2 r} \alpha'_o \overrightarrow{E_0} \sum_{l=1}^{N'} \exp[i(2\pi\nu t - \phi_l)] \tag{2-5}$$

Then the time-average scattered intensity at point p becomes

$$I = \varepsilon_o c \left\langle E_s^2 \right\rangle = \frac{16\pi^4 \alpha'^2_o}{\lambda_0^4 r^2} I_o \left\langle \sum_{l=1}^{N'} \sum_{m=1}^{N'} \exp[i(\vec{q} \cdot \overrightarrow{r_{lm}})] \right\rangle \tag{2-6}$$

where $\Delta\phi_{lm} = \phi_l - \phi_m$ is phase difference between scattering unit *l* and *m* at point p, as presented in Figure 2.2.

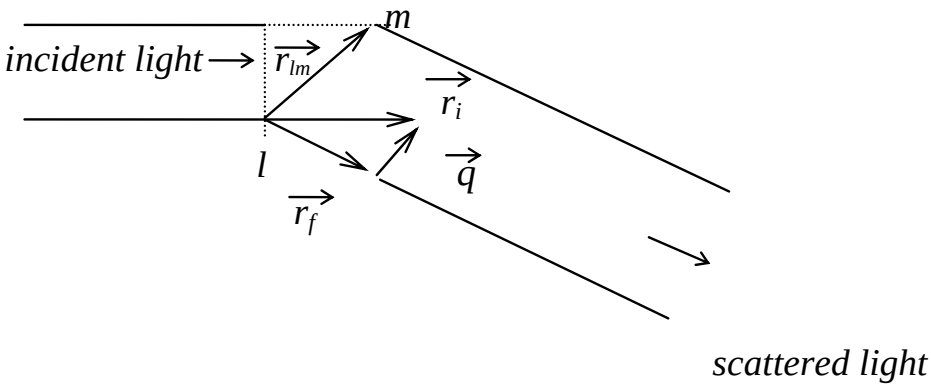

Figure 2.2. A schematically show of the scattering vector and the interference of scattered light inside a larger particle.

and

$$\Delta\phi_{lm} = \vec{q} \cdot \overrightarrow{r_{lm}} \tag{2-7}$$

where $\overrightarrow{r_{lm}} = \overrightarrow{r_m} - \overrightarrow{r_l}$ and $\vec{q} = \vec{r_i} - \overrightarrow{r_f}$ is called scattering vector which is the difference of the unit vector in the direction of the incident beam ($\vec{r_i}$) and the one along the scattered beam ($\overrightarrow{r_f}$), and the vector module

$$q = \left|\vec{q}\right| = \frac{4\pi n}{\lambda_o} \sin\left(\frac{\theta}{2}\right) \tag{2-8}$$

where *n* is the refractive index of the medium.

From equation (2-6), $\exp[i(\vec{q}\cdot\overrightarrow{r_{lm}})]\cong 1$ and I/I_0 is increased by a factor of N^2 compared with a single monomer. The constructive interference between photons scattered by different parts of the polymer chain causes this N^2 dependence. If each part scatters the light independently, then I/I_0 would increase only by a factor of N, as list bellow.

$$I_s = i(N/V) = \frac{16\pi^4 N\alpha'^2}{V\lambda_0^4 r^2} I_o \tag{2-9}$$

with N independent small particles in volume V.

2.1.3 Scattering by many polymer chains

In real system, to obtain reliable time average intensity, where must be many (thousands of) polymer chains in the scattering volume shown in Figure 2.3. Here we consider how these chains collectively contribute to the total scattering intensity.

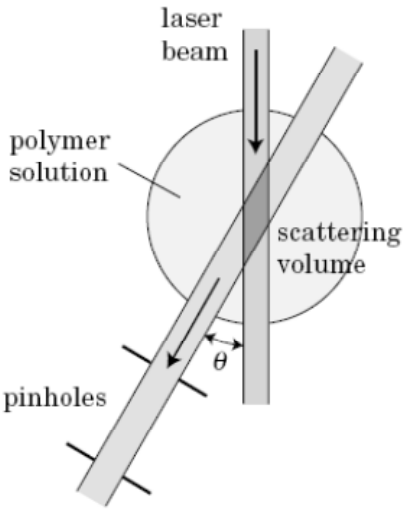

Figure 2.3. Scattering volume is an intersection of the laser beam with the solid angle subtended by the two pineholes.

Considering there are n_p chains, each consisting of N' monomers, the equation (2-6) can be extended to:[7]

$$I = \frac{16\pi^4 \alpha'^{\,2}_o}{\lambda_0^4 r^2} I_o \left\langle \sum_{i,j=1}^{n_p} \sum_{l,m=1}^{N'} \exp[i(\vec{q}\cdot\overrightarrow{r_{jm,il}}) \right\rangle \tag{2-10}$$

where $\overrightarrow{r_{jm,il}} = \vec{r}_{il} - \overrightarrow{r_{jm}}$. The equation can be further deduced into two terms, one is the contribution from two monomers on the same chain, and the other term is a

contribution from two monomers on different chains. The summations in equation (2-10) can therefore be replaced by:

$$\sum_{i,j=1}^{n_p}\sum_{l,m=1}^{N'}\exp[i(\vec{q}\cdot\overrightarrow{r_{jm,il}}) = n_p\sum_{l,m=1}^{N'}\langle\exp[i(\vec{q}\cdot\overrightarrow{r_{1m,1l}})\rangle + {n_p}^2\sum_{l,m=1}^{N'}\langle\exp[i(\vec{q}\cdot\overrightarrow{r_{1m,2l}})\rangle \qquad (2\text{-}11)$$

where $n_p(n_p\text{-}1)$ was approximated by ${n_p}^2$ in the second term. The average in the first term is taken with a statistical weight of a configuration for a single chain and the average in the second term is taken with a weight of configuration of the two chains. At dilute concentrations, polymer chains are sufficiently distant from each other. So the contribution of the second term can be negligible. Thus the scattering intensity can be simplified to be:

$$I = \frac{16\pi^4{\alpha'_o}^2}{\lambda_0^4 r^2} n_p I_o \left\langle \sum_{l=1}^{N'}\sum_{m=1}^{N'}\exp[i(\vec{q}\cdot\overrightarrow{r_{lm}}) \right\rangle \qquad (2\text{-}12)$$

2.1.4 Scattering structure factor and Zimm plot

With an increasing θ, q increases and q^{-1} has been used as a spatial resolution ruler with which static LLS is able to probe the size of colloidal particles and macromolecules at a finite angle. By averaging over all possible orientations ($\overrightarrow{r_{lm}}$) of the particle, we finally have

$$i(\theta) = \frac{16\pi^4}{r^2\lambda_0^4} I_o {\alpha'_o}^2 \sum_{l=1}^{N'}\sum_{m=1}^{N'}\frac{\sin(q\ r_{lm})}{q\ r_{lm}} \qquad (2\text{-}13)$$

where θ is the inclined angle from direction of primary beam to that of line OP, as is shown in Figure 2.1. When $\theta \to 0$,

$$i(\theta \to 0) = \frac{16\pi^4}{r^2\lambda_0^4} I_o {\alpha'_o}^2 N'^2 \qquad (2\text{-}14)$$

Note $N'\alpha_o' = \alpha'$ so that equation (2-14) is the same as equation (2-4). We then define an angular scattering function $P(\theta)$ as

$$P(\theta) = \frac{R(\theta)}{R(0)} = \frac{1}{N'^2}\sum_{l=1}^{N'}\sum_{m=1}^{N'}\frac{\sin(q\ r_{lm})}{q\ r_{lm}} \qquad (2\text{-}15)$$

After developing $\sin(q\ r_{lm})$ into a Taylor series ($\sin x = x - x^3/6 + \ldots$) and retain the two leading terms, the result reads

$$P(\theta) = 1 - \frac{q^2}{6N'^2}\sum_{l=1}^{N'}\sum_{m=1}^{N'}{r_{lm}}^2 + \cdots \qquad (2\text{-}16)$$

where $\frac{1}{2N'^2}\sum_{l=1}^{N'}\sum_{m=1}^{N'} r_{lm}^{\ 2}$ is defined as the mean square of radius of gyration $R_g^{\ 2}$. Thus

$$P(\theta) = 1 - (1/3)q^2 R_g^{\ 2} + \cdots \tag{2-17}$$

which is related to the conformation of the larger particles and that is why it is also called the structure factor (or form factor). For N independent larger particles in volume V, equation (2-13) can be re-written as

$$R(\theta) = \frac{16\pi^4 N}{V\lambda_0^4}\alpha' P(\theta) \tag{2-18}$$

R_{excess} is the net scattering intensity of the solute by substracting the intensity of solvent from that of the solution and can be expressed as (the deduction is omitted here):

$$R_{\text{excess}} = \frac{4\pi^2 n^2}{\lambda_o^{\ 4} N_A}\left(\frac{dn}{dC}\right)^2 \frac{CM}{1 + 2A_2 CM + \cdots} \tag{2-19}$$

Rearrange equation (2-19) by defining $K = 4\pi^2 n^2 (\mathrm{d}n/\mathrm{d}C)^2 / (N_A \lambda_0^4)$, we get

$$\frac{KC}{R} = \frac{1}{M} + 2A_2 C + \cdots \tag{2-20}$$

where we have omitted the footnote "excess" in R_{excess}. For larger macromolecules, construction factor must be introduced, thus

$$\frac{KC}{R(\theta)} = \frac{1}{MP(\theta)} + 2A_2 C \tag{2-21}$$

The last question in deriving basic equation of static LLS is the polydispersity in real cases. From equation (2-17), in the limit of vanishing concentration $C \to 0$,

$$R(\theta) = KCMP(\theta) = KCM[1\text{-}(1/3)\, q^2 R_g^{\ 2} + \cdots] \tag{2-22}$$

Considering the additive nature of the excess Rayleigh ratio, for a polydispersed polymer solution at $C \to 0$

$$R(\theta) = \sum_i R(\theta)_i = \sum_i KC_i M_i [1 - (1/3)q^2 R_{g,i}^{\ 2} + \cdots] \tag{2-23}$$

If we divide equation (2-23) by the total polymer concentration $C = \sum_i C_i$, we get, after slightly re-arrangement,

$$\frac{R(\theta)}{KC} = \frac{\sum_i C_i M_i}{\sum_i C_i}\left(1 - \frac{q^2 \sum_i C_i M_i R_{g,i}^{\ 2}}{3\sum_i C_i M_i} + \cdots\right) \tag{2-24}$$

or

$$\frac{R(\theta)}{KC} = M_w[1-(1/3)q^2 < R_g{}^2 >_z + \cdots] \tag{2-25}$$

Now, come back to equation (2-21). When $q^2R_g{}^2 << 1$, omitting the higher order terms in series, we get

$$\frac{KC}{R(\theta)} = \frac{1}{M_w}[1+\frac{1}{3}q^2 < R_g{}^2 >_z] + 2A_2C \tag{2-26}$$

This is the basic equation of static LLS which is frequently shown in scientific papers. Naturally, the molar mass in the equation, $M_w = \sum_i C_i M_i / \sum_i C_i$, is weight-average; and the mean square radius of gyration, $< R_g{}^2 >_z = \sum_i C_i M_i R_{g,i}{}^2 / \sum_i C_i M_i$, is z-average. It shows that with $R(\theta)$ measured at a series of C and q, we are able to determine $<R_g{}^2>_z$ from the slope of $[KC/R(\theta)]_{C\to 0}$ versus q^2; A_2 from the slope of $[KC/R(\theta)]_{\theta\to 0}$ versus C; and M_w from $[KC/R(\theta)]_{C\to 0,K\to 0}$. The Zimm plot, i.e., $KC/R(\theta)$ versus (q^2 + kC) with k being an adjustable constant, allows both q and C extrapolations to be made on a single coordinate plane.[8, 9] It should be mentioned that Equation (2-26) is valid under the restriction that the polymer solution exhibits no adsorption, no fluorescence, and no depolarized scattering. For branched structures, the Berry[10] plot ($[KC/R(\theta)]^{1/2}$ vs q^2 + kC) is more adequately used because it often removes much of the curvature observed in the angular dependence of the Zimm plot. If the structure is expected to be large and globular, the Berry plot is not linearized but still shows upturn. In these cases, it is often appropriate to apply a modified Guinier[11, 12] plot, i.e., $\ln[KC/R(\theta)]$ vs q^2 + kC that removes the upturn even more efficiently.

In practice, the Rayleigh ratio is determined by a relative method; namely, by measuring the scattering intensity of a standard such as benzene or toluene, we can calculate the Rayleigh ratio of a give solution by

$$R_{vv}(\theta) = R^o_{vv}(\theta)\frac{I(\theta)_{solution} - I(\theta)_{solvent}}{I(\theta)_{standard}}(\frac{n_{solvent}}{n_{standard}})^{\gamma} \tag{2-27}$$

where the subscript "*vv*" means both the incident and the scattered light are vertically (z-axis direction in Figure 2.1) polarized; I and n are, respectively, the time-averaged scattered light intensity and the refractive index. The term $(n_{solvent}/n_{standard})^{\gamma}$ is a

refraction correction for the scattering volume and γ is a constant between 1 and 2, depending on the detection geometry of the light scattering instrument, because we should compare the same scattering volume from the solution and the reference standard. If we take the incident light as the *x*-direction and the scattered light as the *y*-direction (i.e., $\theta = 90^{o}$), we only need to have a linear correction of the refraction in the *x*-direction if a slit is used to determine the scattering volume, i.e., $\gamma = 1$ because we have already seen all the scattered lights in the z-direction (vertical). On the other hand, if a pinhole with a size much smaller than the diameter of the incident beam at the center of the scattering cell, we have to correct the refraction in both the *x*- and *z*-directions, i.e., $\gamma = 2$. However, if the pinhole size is comparable to the beam diameter, $1 < \gamma < 2$. In practice, we should avoid this situation by choosing either a slit or a smaller pinhole.[1, 13]

2.2 Dynamic Laser Light Scattering

Motions (translational, rotational or internal motion) of macromolecules or colloidal particles in solution can be conveniently studied by using dynamic laser light scattering (dynamic LLS). Measurement at a single scattering angle (or at a finite q) gives information on the dimension of macromolecules or colloidal particle in the solution with reasonable accuracy. Unlike the static LLS version, dynamic LLS does not rely on the excess scattering intensity between the pure solvent and a dilute solution. The signal from the slowly moving polymer is unambiguously separated from the signal that originates from the rest of the solution. The principle of dynamic LLS has been utilized in some commercial particle-sizing systems for many years. The measurement and data analysis are automated. Users only need to prepare clean solutions by filtration. In recently years, dynamic LLS has been also used as an on-line detector in size exclusion chromatography (SEC). Nowadays, the most commonly used method in quasi-elastic light scattering (QELS) is the digital technique of photon correlation spectroscopy (or optical mixing) which measures the intensity fluctuation of scattered light in time domain. Practically there are two basic forms of optical mixing: heterodyne and homodyne (self-beating). By heterodyne mixing we refer to the mix of the scattered light with a reference beam (local oscillator) unshifted or shifted in frequency from the incident light beam. In self-beating optical mixing the scattered wave is not mixed with a reference signal

but directly detected. Here we only consider the self-beating intensity-intensity time correlation spectroscopy.

2.2.1 Power spectrum of time-correlation function

The powder spectrum $S_A(\omega)$ of a time-correlation function $<A(0)A^*(t)>$ is defined as

$$S_A(\omega) = \frac{1}{2\pi}\int_{-\infty}^{\infty} < A(0)A^*(t) > \exp(-i\omega\, t)\mathrm{d}t \tag{2-28}$$

where A^* is the complex conjugate of A. This quantity plays an important role in much of what follows. In fact, as we shall see, what is measured in light scattering is the power spectral density of the electric field of the scattered light. Fourier Inversion of the equation leads to an expression for the time-correlation function in terms of the powder spectrum.

$$< A(0)A^*(t) > = \int_{-\infty}^{\infty} \exp(i\omega\, t)\ S_A(\omega)\mathrm{d}t \tag{2-29}$$

Thus the time-correlation $< A(0)A^*(t) >$ and the power spectrum $S_A(\omega)$ are Fourier transforms of one another and the experimental determination of one as a function of its argument is sufficient for the determination of the other. In fact, $< A(0)A^*(t) >$ can be either the scattered field-field autocorrelation function $< E(0)E^*(t) >$ or the intensity-intensity autocorrelation function $< I(0)I(t) >$, which will be further discussed in the following sections.

2.2.2 Autocorrelation of scatter field

Now we consider again an N particle (macromolecule or colloidal particles) scattering system with scattering volume V. We view N particles as N scatters. Thus, the scattered field as well as the scattered intensity at point p in Figure 2.1 can still be expressed using equation (2-5) and (2-6) and they are,

$$\vec{E}(t) = \sum_{i=1}^{N} \overrightarrow{E_i}(t) = -\frac{4\pi^2}{\lambda_0^2 r}\alpha'_o\, \overrightarrow{E_0} \sum_{i=1}^{N} \exp i[2\pi\nu t - \phi_i(t)] \tag{2-30}$$

and

$$I(t) \propto \sum_{i=1}^{N}\sum_{j=1}^{N} \exp i\,\vec{q}[\vec{r_i}(t) - \vec{r_j}(t)] \tag{2-31}$$

Note $\phi_i(t)$ represents the phase term of ith particle and is now a function of time due to the motion of the particles. Same situation should be applied to $I(t)$ and $\Delta\phi_{ij}(t)$ because $\Delta\phi_{ij}(t) = \vec{q}\cdot\overrightarrow{r_{ij}}(t)$ and $\overrightarrow{r_{ij}}(t)$ will have different orientation at different time t. When the scatters are undergoing Brownian motion, $\vec{E}(t)$ has a randomly

modulated phase. The scattered light is broadened in frequency with an optical frequency distribution, or, power spectrum $S(\omega)$ as illustrated in Figure 2.4.

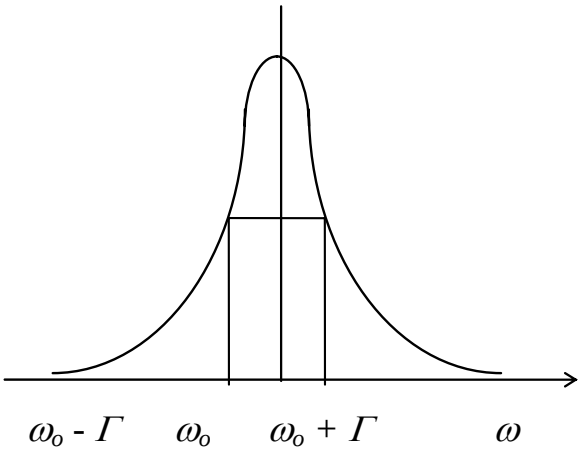

Figure 2.4. The power spectrum S(ω) of scattered light: a Lorentzian optical frequency distribution centered by the angular frequency of the incident light ω_0 with line width of Γ.

The form of this curve, arising from dissipative fluctuations, is a Lorentzian distribution centered at the incident laser frequency ω_o, described by:

$$S(\omega) = \frac{2\Gamma}{\Gamma^2 + (\omega - \omega_o)^2} \tag{2-32}$$

It can be seen from Figure 2.4 and equation (2-32) that when $\omega = \omega_o$, $S(\omega) = 2/\Gamma$; and when $\omega = \omega_o \pm \Gamma$, $S(\omega) = 1/\Gamma$. That means when the scattered frequency shifts a distance of Γ from ω_o, the density function of power spectrum $S(\omega)$ is half the value that of its peak value. For this reason, Γ is called half-width at half-height, or simply, line-width. As stated before, it is difficult to measure Γ (or $S(\omega)$) directly in frequency domain because $\Gamma << \omega_o$. It is known from mathematics that $S(\omega)$ and the field-field autocorrelation function $<E(0)E^*(t)>$ are a pair of Fourier transform and inverse Fourier transform:

$$< E(0)E^*(t) > = \int_{-\infty}^{\infty} S_x(\omega)\exp(-i\omega\, t)\mathrm{d}\omega \tag{2-33}$$

$$S(\omega) = \frac{1}{2\pi}\int_{-\infty}^{\infty} < E(0)E^*(t) > \exp(i\omega\, t)\mathrm{d}t \tag{2-34}$$

These two equations are known as Wiener-Khintchine theory. Thus, $S(\omega)$ and $<E(0)E^*(t)>$, two functions originally located in frequency domain and time domain

respectively, are now connected with each other. Γ is directly related to the characteristic decay time $\Gamma = 1/\tau_c$.

To relate with the intensity-intensity autocorrelation function, the normalized electric-field autocorrelation function is defined as:

$$g^1(q,\tau) = \frac{< E(q,0)E^*(q,\tau) >}{< E(q,0)E^*(q,0) >} \tag{2-35}$$

2.2.3 Autocorrelation of Intensity

The autocorrelator calculates the average of the product of two scattering intensities $I(t)$ and $I(t+\tau)$ measured at the two times separated by τ, with τ called delay time. The average $<I(t)I(t+\tau)>$ is function of τ and is called intensity-intensity autocorrelation function. The autocorrelator converts $I(t)$ into $<I(t)I(t+\tau)>$ and the intensity-intensity autocorrelation can be written to:

$$<I(t)\, I(t+\tau)> = <I>^2 + <\Delta I(t)\Delta I(t+\tau)> \tag{2-36}$$

Division of $<I(t)\, I(t+\tau)>$ by $<I>^2$ leads to:

$$\begin{aligned} <I(t)\, I(t+\tau)> / <I>^2 &= 1 + <\Delta I(t)\Delta I(t+\tau)> / <I>^2 \\ &= 1 + f_c\, g^2(\tau) \end{aligned} \tag{2-37}$$

where f_c is called the coherence factor, defined as

$$f_c = <\Delta I>^2 / <I>^2 \tag{2-38}$$

and the second factor is the baseline-subtracted, normalized intensity autocorrelation function:

$$g^2(q,\tau) = <\Delta I(q,t)\Delta I(q,t+\tau)> / <\Delta I>^2 \tag{2-39}$$

The coherence factor depends on the coherence of the light falling on the photodetector. The beam has a finite cross section, and different parts of the beam may not have the same phase. If they have the same phase, the number of photons will be distributed with a Possion distribution. The variance of I is then equal to the square of the mean, i.e., $f_c = 1$. In general, $0 < f_c < 1$. Use of a smaller pinhole increases f_c at the expense of a weakening intensity. As shown in Figure 2.5a, $g^2(q,\tau)$ is 1 at $\tau = 0$ and decays to zero as $\tau \to \infty$.

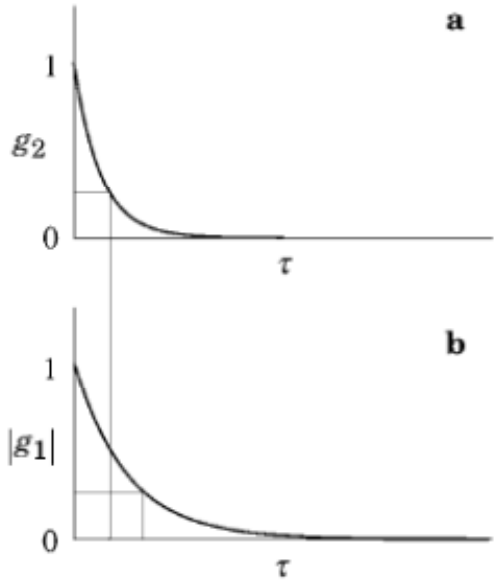

Figure 2.5. Baseline-subtracted, normalized intensity autocorrelation function $g^2(q,\tau)$ (a) and the absolute value of the baseline-substracted, normalized electric-field autocorrelation function, $g^1(q,\tau)$ (b).

2.2.4 Siegert relation[2]

Another important equation in dynamic LLS is Siegert relation. Without a local oscillator (i.e., a constant fraction of the incident light reaching the detector from various intentional sources, such as surface scratching or reflection), the self-beating of the scattered electric field leads to normalized intensity-intensity autocorrelation function, $g^{(2)}(q,t)$ based in essence on the Sieget relation:

$$g^{(2)}(q,t) = 1 + \left| g^{(1)}(q,t) \right|^2 \tag{2-40}$$

where $g^{(2)}(q,t) \equiv [\langle I(q,0)I(q,t)\rangle / \langle I(q,0)\rangle^2]$ and $g^{(1)}(q,t) \equiv [\langle E(q,0)E^*(q,t)\rangle / \langle E(q,0)E^*(q,0)\rangle]$ is the normalized field-field time correlation functions. Thus, the intensity-intensity time correlation function

$$G^{(2)}(q,t) = \langle I(q,0)I(q,t)\rangle = \langle I(q,0)\rangle^2 g^{(2)}(q,t)$$
$$= \langle I(q,0)\rangle^2 [1+|g^{(1)}(q,t)|^2] \tag{2-41}$$

The significance of introducing $g^{(2)}(q,t)$ and $G^{(2)}(q,t)$ lies in the fact that $G^{(2)}(q,t)$ and $\langle I(q,0)\rangle$ can be measured experimentally. In practice, the detection area can not be zero no matter how small it is. Therefore, the scattered light detected can not be purely coherent and an instrument parameter, β (<1), is introduced in equation (2-41):

$$G^{(2)}(q,t) = A(1+\beta \left| g^{(1)}(q,t) \right|^2) \tag{2-42}$$

where $A(\equiv< I(q,0) >^2)$ is the baseline, t is the delay time, β is a parameter depending on the coherence of the detection optics, and $I(t)$ is the detected scattered intensity or photon counts at time t, including contributions from the solvent and the solute. Therefore, $G^{(2)}(q,t) =< [I_{solvent}(q,0) + I_{solute}(q,0)][I_{solvent}(q,t) + I_{solute}(q,t)] >$ and equation (2-42) becomes

$$G^{(2)}(q,t) = A\{1 + \beta[\frac{I_{solvent}}{I_{solution}} \mid g^{(1)}_{solvent}(q,t) \mid + \frac{I_{solute}}{I_{solution}} \mid g^{(1)}_{solute}(q,t) \mid]^2\} \qquad (2\text{-}43)$$

where all the cross terms have been dropped by assuming that the light scattered by solvent molecules and particles is not correlated. It should be noted that $\mid g^{(1)}_{solvent}(q,t) \mid$ decays much faster than $\mid g^{(1)}_{solute}(q,t) \mid$ because small solvent molecules diffuse much faster than larger particles. Thus, after a very short delay time, equation (2-42) becomes

$$G^{(2)}(q,t) \cong A[1 + \beta(\frac{I_{solute}}{I_{solution}})^2 \mid g^{(1)}_{solute}(q,t) \mid^2]$$

$$= A[1 + \beta_{app} \left| g^{(1)}_{solute}(q,t) \right|^2] \qquad (2\text{-}44)$$

where $\beta_{app} = \beta(I_{solute}/I_{solution})^2$. For a dilute solution, the scattered intensity from solvent molecules could become appreciable (i.e., $I_{solute} \leq I_{solution}$) and thus the apparent coherence β_{app} would be lower, i.e., $G^{(2)}(q,0)$ appears to have a very low value than expected. We should be aware of this situation, especially for weakly scattered dilute and low-molar-mass polymer solution. For example, if $I_{solute} = I_{solvent}$, $\beta_{app} = \beta/4$. It should be noted that β is constant for each particular optical geometry of the scattering instrument. In fact, I_{solute} can be estimated from β_{app} if the values of β at different scattering angles have been pre-calibrated with a narrowly distributed latex standard whose scattering intensity is much stronger than water (solvent), as first demonstrated by Sun *et al.*[14]

2.2.5 Translational diffusions

Now we will see how to get the information about the motion of the particles from the measured intensity-intensity time correlation function $G^{(2)}(q,t)$. Generally, the relaxation of $\mid g^{(1)}(\mathrm{q},t) \mid$ includes both diffusion (translation and rotation) and internal motions. Let us first consider the translational diffusion relaxation of the particles. For monodispersed spherical scatters, $|g^{(1)}(q,t)|$ is theoretically represented as an exponential decay function:

$$| g^{(1)}(\mathrm{q},t) | = G\exp(-\Gamma t) \tag{2-45}$$

where G and Γ are the factor of proportionality and the line-width, respectively and $\Gamma = \tau_c^{-1}$, the characteristic decay time representing the rate of dynamic relaxation in self-beating. For a polydispersed polymer sample with a continuous distribution of molar mass M, equation (2-45) may be generalized as

$$| g^{(1)}(q,t) | = \int_0^\infty G(\Gamma)\exp(-\Gamma t)d\Gamma \tag{2-46}$$

where $G(\Gamma)$ is called the line width distribution and $G(\Gamma)\mathrm{d}\Gamma$ is the statistic weight of the particles or macromolecules which possess line width Γ. For a dilute solution, Γ measured at a finite scattering angle is related to C and q by[15]

$$\Gamma = q^2 D(1 + k_d C)(1 + f\ q^2 < R_g^2 >_z) \tag{2-47}$$

where D is the translational diffusion coefficient of the solute molecule at $C \to 0$, k_d is the diffusion second virial coefficient, and f is a dimensionless parameter depending on polymer chain structure and solvent (For polymers with flexible chains in a good solvent, f is between 0.1 and 0.2). Hence, for small C and q, $D \approx \Gamma/q^2$ and it is apparent that $|g^{(1)}(q,t)|$ decays faster at a higher scattering angle. Figure 2.6 demonstrates the linear dependence of the line with Γ on the scattering vector q and shows that this relaxation mode has diffusive character.

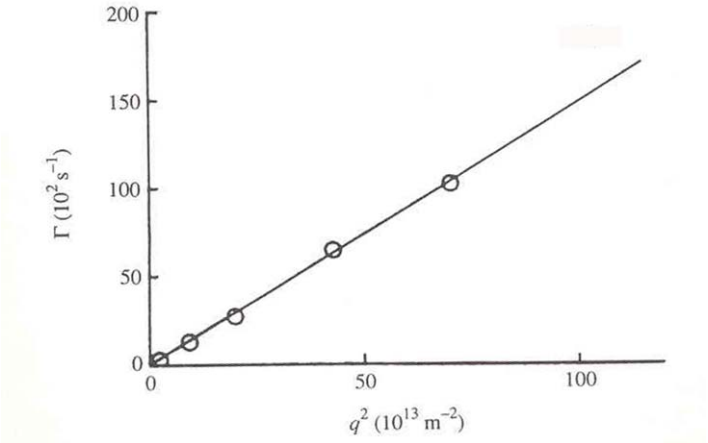

Figure 2.6. Linear dependence of the characteristic line width Γ on scattering vector q.

It should be noted that by the definition of $|g^{(1)}(q,t)|$, $G(D) = q^2\mathrm{G}(\Gamma)$, the translational diffusion coefficient distribution, is an intensity distribution. And, since $|g^{(1)}(q,t)|$ approaches unity as $t \to 0$, we have:

$$|g^{(1)}(\mathrm{q}\to 0, t\to 0)|=\frac{\left\langle E(q,0)E^{*}(q,t\to 0)\right\rangle}{\left\langle \mathrm{E(q,0)E}^{*}(q,0)\right\rangle}=\int_0^\infty G(\Gamma)\mathrm{d}\Gamma=\int_0^\infty G(D)dD=1 \quad (2\text{-}48)$$

The average diffusion coefficient <*D*> is defined as:

$$< D >=\int_0^\infty G(D)D\ dD \quad (2\text{-}49)$$

Further, the translational diffusion coefficient *D* may be related to the molecular friction factor *f* through the Stokes-Einstein relation:

$$D = k_B T / f \quad (2\text{-}50)$$

where k_B and *T* are the Boltzmann constant and the absolute temperature respectively. For a hard sphere with a radius of *R*, $f = 6\pi\eta R$, where η is the viscosity of the solvent. For a polymer coil, *R* is replaced by its hydrodynamic radius R_h, so that

$$R_h = \frac{k_B T}{6\pi\eta D} \quad (2\text{-}51)$$

2.3 Living Anionic Polymerization

2.3.1 Home-made high vacuum system

A new improved design of Rotaflo® high vacuum stopcock provides many significant benefits; it has excellent chemical resistance, can operate over a pressure range of +1 bar to 10^{-9} Torr and temperature range of -20ºC to 200ºC. With the advantages of this kind of needle-valve stopcock, we design a novel connector which is shown in Figure 2.7 to replace the break-seal connector in high vacuum system. This novel connector is easier to handle than break-seal and can be used repeatedly while break-seal only can be used one time. Based on this idea, we establish a Home Made High Vacuum System which is easier and faster to run than high vacuum system but still obtain the advantages of high vacuum system. Home-made high vacuum system includes high vacuum line and interchangeable glassware two major parts.

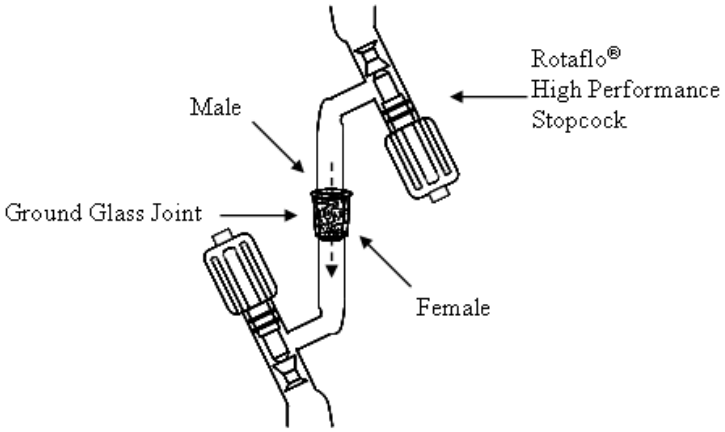

Figure 2.7. Novel connector in home made high vacuum system. A Rotaflo high performance stopcock is connected with a male or a female ground joint.

2.3.2 High vacuum line

The high vacuum line gives the reactors access to vacuum of 10^{-6} Torr or ultra-high purity grade argon with a typical outlet gauge pressure of 0.4 bar. It is used during the different purification processes of chemicals and glassware as described in next section. The line is shown schematically in Figure 2.8. The main parts of a high vacuum line are the rotary pump, diffusion pump, two liquid nitrogen cold traps and the stopcocks. The rotary pump is used in order to reduce the pressure of the system in a level of 10^{-3} Torr. After the diffusion pump is achieved, the pressure of system can be brought to a value around 10^{-6} Torr. Reactors and other glass apparatuses are jointed to the vacuum line through the lower ring *via* heavy wall PORTEX PVC high vacuum tubing.

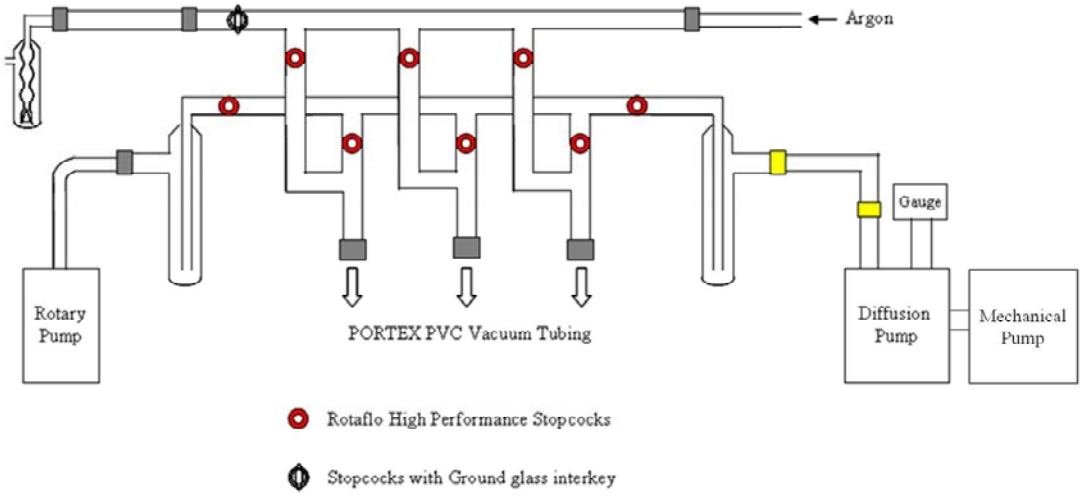

Figure 2.8. Home made high vacuum line with argon system.

2.3.3 Interchangeable glasswares

The interchangeable glassware apparatus used for monomer and solvent purification and for polymerization are shown in Figure 2.9.

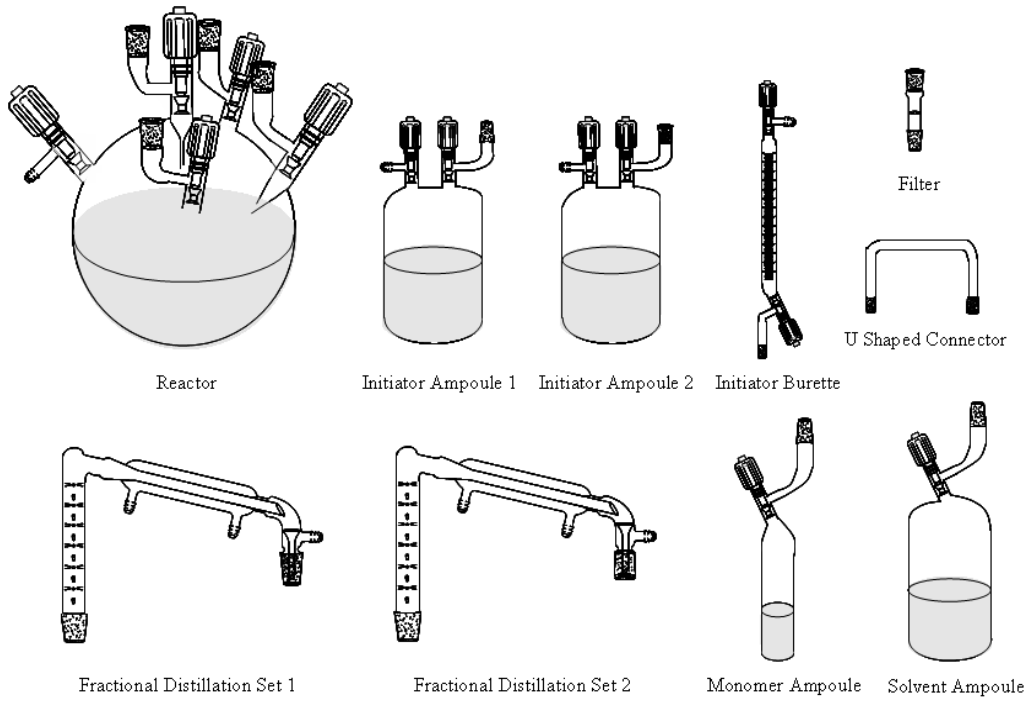

Figure 2.9. Interchangeable glassware apparatus.

Reactor: The reactor is a round bottom flask with 5 or 6 necks depends on what kind of target polymer is needed. Each neck contains a Rotaflo® high performance stopcocks and a ground glass socket. Solvent, monomer and initiator are connected to reactor by the novel connector shown in Figure 2.7.

Monomer ampoule: The monomer ampoule is made of a cylindrical flask with a Rotaflo® high performance stopcocks and a ground glass cone.

Solvent ampoule: The solvent ampoule is the similar with the monomer ampoule besides the volume of solvent ampoule is larger than which of the monomer ampoule.

Fractional distillation set 1: The fractional distillation set 1 is made of vigreux column, condenser and two ground glass cones which they are connected directly. It is used in the purification of solvent and monomer.

Fractional distillation set 2: The fractional distillation set 2 is the similar with factional distillation set 1 besides the ground glass cone in the receiver is replaced by a ground glass socket. Set 2 is used to transfer solvent and monomer to solvent and monomer ampoule in their purification process.

Initiator burette: The initiator burette is made of two Rotaflo® high performance stopcocks and a ground glass cone.

Initiator ampoule 1: The initiator ampoule 1 is made of a round flask with two Rotaflo high performance stopcocks and a ground glass cone.

Initiator ampoule 2: The initiator ampoule 2 is the similar with factional distillation set 1 besides the ground glass cone in the receiver is replaced by a ground glass socket.

Filter: The filter is made of sintered disc with a ground glass cone and a ground glass socket. It is used in the preparation of initiator to remove the precipitate and unreacted metal particles.

U shaped connector: The U shaped connector is made of a ground glass cone and a ground glass socket. It is used in the preparation of initiator.

2.3.4 Chemical purification

The purification methods of chemicals are followed the literatures except the need for changing to fit the home made high vacuum system.[16, 17]

THF (99.8%, Lab-Scan): THF is refluxed with sodium metal for 2 days in the setup before it is fractionally distilled into a solvent ampoule with a Rotaflo stopcock in the presence of potassium naphthalenide.

Benzene (99.7%, BDH): Benzene is usually purified by stirring repeatedly over concentrated sulfuric acid until the layer of sulfuric acid appears clear, then with D.I. water, dilute NaOH aqueous solution and D.I. water, followed by drying over $MgSO_4$ and CaH_2. Benzene is finally fractionally distilled into solvent ampoule in the presence of *n*-BuLi.

Hexane (99.0%, Lab-Scan): Hexane is purified in a manner similar to benzene.

Methanol (99.9%, Lab-Scan): Methanol is degassed 3 times before it is fractionally distilled into monomer ampoule.

Acidic Methanol (acidic acid and methanol with 1:1 v/v): Acidic methanol is purified in a manner similar to methanol.

Styrene (≥ 99%, 10-15 ppm 4-tert-butylcatechol inhibitor, Sigma-Aldrich): Styrene is dried over finely grounded CaH_2 for 2 days and then fractionally distilled into flask where a solution of dibutylmagnesium has been vacuum dried first. It stand at the room temperature with continuous stirring until a bright yellow-greenish color is developed. Further, styrene is fractionally distilled into a monomer ampoule and

about 3 times of purified THF is fractionally distilled into the monomer ampoule to form a styrene solution.

Isoprene (99%, Acros): Isoprene is dried over finely grounded CaH_2 for 2 days and then is fractionally distilled into flask where a solution of *n*-BuLi has been vacuum dried first. It is stirring with *n*-BuLi for 1 hr at 0 ^oC and then is fractionally distilled into a monomer ampoule. Further, 3 times of purified THF is fractionally distilled into the monomer ampoule to form an isoprene solution.

Propylene sulfide (99%, Acros): propylene sulfide is dried over finely grounded CaH_2 for 2 days and after after 3 time degassing, it is fractionally distilled into a ampoule, before purifed THF is fractionally disstilled for dilution.

2.3.5 Polymerization procedure

The detail of living anionic polymerization can be found elsewhere.[17-19] The outline of preparation of PS-*b*-PI diblock copolymer is followed:

The ampoules containing all necessary reagents, that is, the initiator and purified monomers are attached to the main reactor, as shown in Figure 2.10. The apparatus is attached to the vacuum line, checked for pinholes, flame dried, and pumped for 1 hr in order to remove the volatile species such as air and humidity. The rotary pump is used to reduce the pressure in the system in a level of 10^{-3} Torr before the diffusion pump is used. Then the solvent THF and monomer styrene are added in vacuum from the purified reservoirs. The apparatus is frozen with liquid nitrogen and degassed. A few drops of initiator, *sec*-butyllithium, are added first and is followed by the rinse of the reactor with the initiator solution. Because of the small amount of impurities in the reactor, the solution might be still colorless at the first few drops of initiator. Initiator solution is continuous added, and the rinse procedure is followed until the color of the solution suddenly turns to slight yellow. Then calculated amount of initiator is further added into the reactor under vigorous stirring. The reactor is set to bath at –78 ^oC in a liquid nitrogen/Acetone Dewar flask. The polymerization of styrene is left to reaction about 1 hr until all monomer is consumed. The second monomer isoprene is added sequentially and is left to reaction about 2 hrs to complete the polymerization. Afterwards, degassed methanol is added to quench the polymerization. For a typical polymerization the amount of solvent is chosen such that the final polymer concentration is about 5–10%, depending on the molecular weight of the polymer.

Figure 2.10. Assembled apparatus of home made high vacuum system.

The synthesis for the thiol-terminated polystyrene is very similar, regarding the propylene sulfide as a second monomer, but with very short block length. Usually, slightly excessive amount (~ 2 eq) is added for titration to ensure that each of the living polystyrene chain is ended with propylene sulfide, before purified acid methanol is finally added for chain termination.

2.3.6 Characterization

After synthesized, the polystyrene-*b*-polyisoprene diblock copolymers are characterized with the nuclear magnetic resonance (HNMR) as shown in Figure 2.11.

Vinyl proton peaks at 5.79 and 4.68 ppm confirm the 1,2- and 3,4- addition product for PI.[20] And the integration area ratio between "a" for polystyrene and "b, c and d" for polyisoprene can be used to estimate the molar fraction for each of the blocks (54 mol% or 64 wt% for PS block).

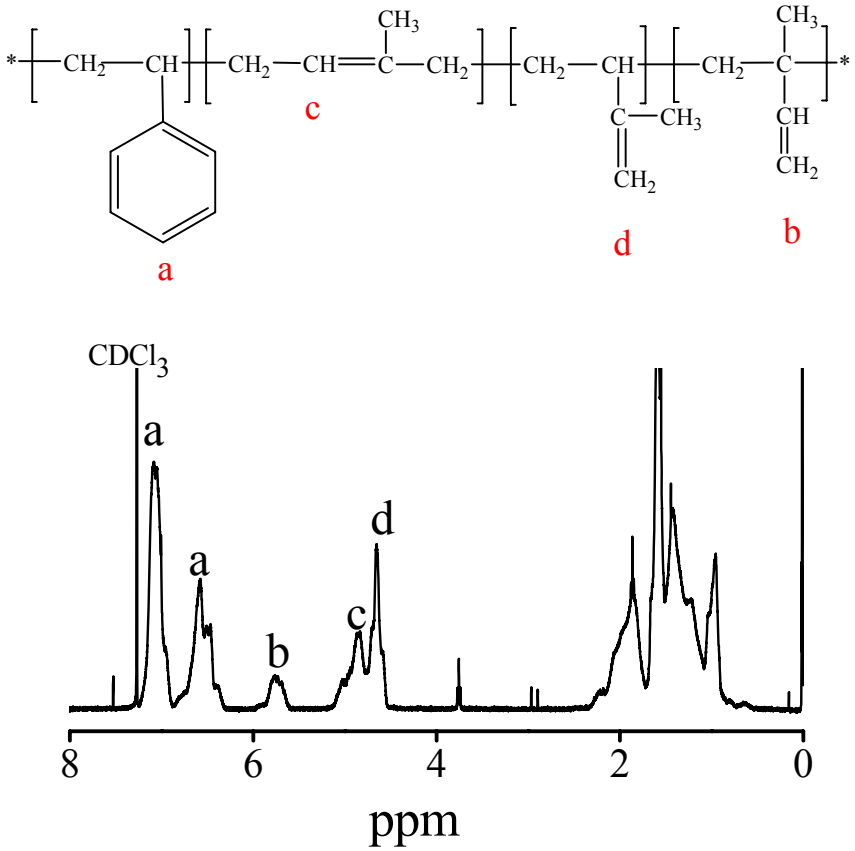

Figure 2.11. Proton NMR spectrum of PS-*b*-PI diblock copolymer in $CDCl_3$.

After the determination block copolymer composition, further characterization for molecular mass was carried with static light scattering (in Figure 2.12), where the refractive index increment for the PS-*b*-PI in THF was estimated by dndc = $dndc_{PS} \times f_{PS} + dndc_{PI} \times f_{PI} = 0.193 \times 0.64 + 0.148 \times 0.36 = 0.177$ ml/g where the dndc data for homopolymer polystyrene and polyisoprene are available from the Polymer Handbook. With a final weight average molecular mass $M_w = 4.6 \times 10^4$ g/mol determined by the zimm plot and weight fraction of 64% for PS block, the composition of block copolymer is written as: PS_{285}-*b*-PI_{245}.

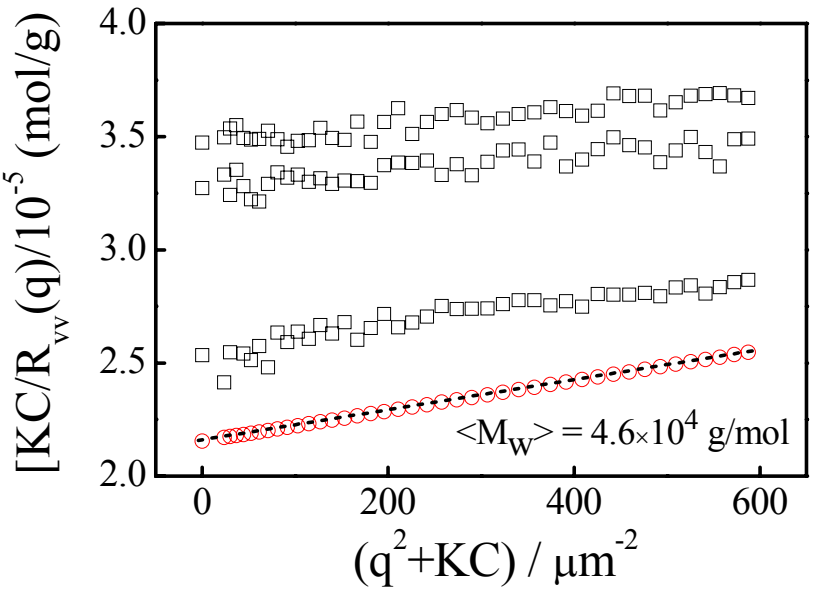

Figure 2.12. Zimm plot of PS-*b*-PI diblock copolymer in THF.

2.4 Nanopore Extrusion Setup

The nanopore extrusion experimental setup is illustrated in Figure 2.13. An SGE gastight syringe and a Whatman 20-nm filter were used. The nanopore filter has a double-layer structure of the membrane. The upper thick layer (59 μm) and the under thin layer (1 μm), respectively, contain 200- and 20-nm pores with pore number of ~ 9×10^8. On average, each small pore is covered by a large one. Such structures are confirmed by SEM images from both sides and cross-section (Figure 2.14). Micellar solution was stored in the syringe, with 20 nm nanopore filter connected. The solution after extrusion was collected into a pre-dust-free vial (typical volume of 1 mL) for further LLS measurement. The ultrafiltration experiment was performed at room temperature. The flow rate of each block copolymer micellar solution through the filter was controlled by a Harward-2000 syringe pump while the hydraulic pressure drop across the nanopore membrane for the ultrafiltration process was *in situ* measured by a high accuracy pressure sensor from ASCO.

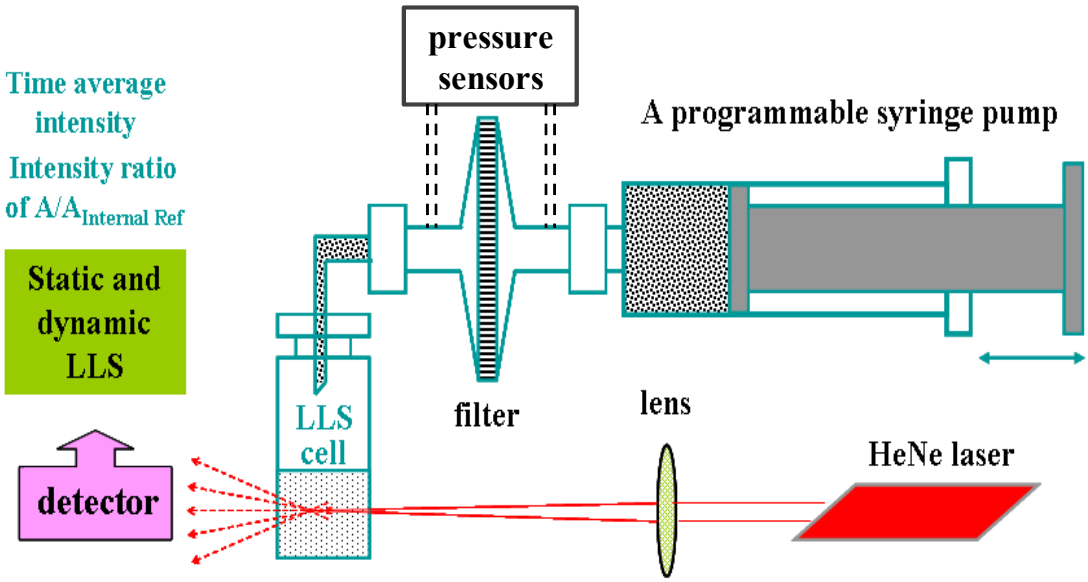

Figure 2.13. Illustration of nanopore extrusion experimental setup.

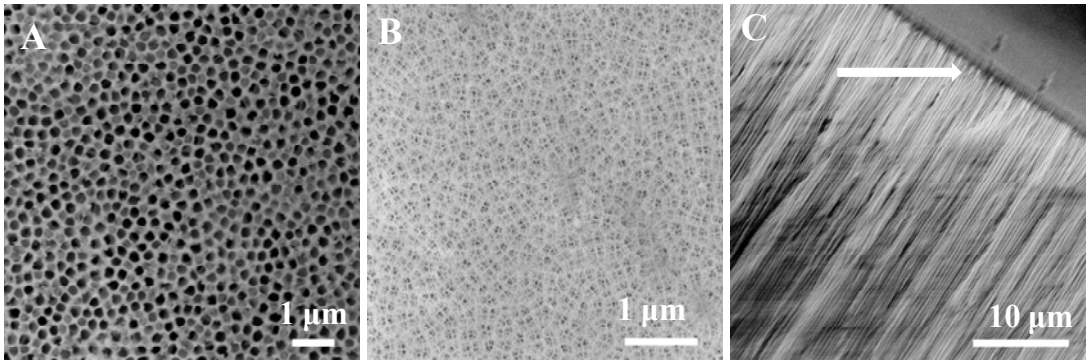

Figure 2.14. SEM images for the 20 nm nanopore membrane filters from (A) larger pore side view; (B) smaller pore side view; (C) cross-section side view.

2.5 References and Notes

(1) Berne, B. J.; Pecora, R., *Dynamic Light Scattering*. John Wiley & Sons Press: New York, 1972.

(2) Chu, B., *Laser Light Scattering: Basic Principles and Practice*. 2nd ed.; Academic Press: New York, 1991.

(3) Zimm, B. H., *J. Chem. Phys.* **1948,** 16, 1099.

(4) Cummins, H. Z.; Knable, N.; Yeh, Y., *Phys. Rev. Lett.* **1964,** 12, 150.

(5) Berne, B. J. E., *Dynamic Light Scattering: The Method and Some Applications*. Clarendon Press: Oxford, 1993.

(6) Brown, W. E., *Light Scattering: Principles and Development*. Clarendon Press: Oxford, 1996.

(7) Teraoka, I., *Polymer Solutions: An Introduction to Physical Properties*. John Wiley & Sons Press: New York, 2002.

(8) Zimm, B. H., *J. Chem. Phys.* **1948,** 16, 1099.

(9) Burchard, W., Light Scattering Techniques. In *Physical Techniques for Study of Food Biophymers*, Ross-Murphy, S. B., Ed. Blackie Academic & Professional: 1995.

(10) Berry, G. C., *J. Chem. Phys.* **1966,** 44, 4550.

(11) Guinier, A., *Ann. Phys.* **1939,** 12, 161.

(12) Guinier, A.; Fournet, G., *Small Angle Scattering of X-rays*. John Wiley: New York, 1955.

(13) Wu, C.; Chu, B., Light Scattering. In *Experimental Methods in Polymer Science*, Tanaka, T., Ed. Academic Press: San Diego, 2000.

(14) Sun, S. T.; Nishio, I.; Swislow, G.; Teraoka, I., *J. Chem. Phys.* **1980,** 73, 5971.

(15) Schmidt, M.; Stockmayer, W. H., *Macromolecules* **1984,** 17, 509-514.

(16) Armarego, W. L. F.; Chai, C. L. L., *Purification of Laboratory Chemicals*. 5th ed.; Butterworth Heinemann: Oxford, 2003.

(17) Hadjichristidis, N.; Iatrou, H.; Pispas, S.; Pitsikalis, M., *J. Polym. Sci. Part A: Polym. Chem.* **2000,** 38, 3211-3234.

(18) Uhrig, D.; Mays, J. W., *J. Polym. Sci. Part A: Polym. Chem.* **2005,** 43, 6179-6222.

(19) Szwarc, M., *Adv. Polym. Sci.* **1983,** 49, 1-177.

(20) Morton, M., *Anionic Polymerization: Principles and Practice*. Academic Press: New York, 1983.

Chapter 3
LLS and TEM Studies on Block Copolymer Spherical Micelles Swelling with Addition of Common Solvent

3.1 Introduction

The formation of block copolymer micelles with different morphologies has fascinated polymer researchers for more than two decades. There is no any slow-down sign in this still-booming field termed by some eyes-catching words like "self-assembly", "supramolecules", "nanoscience" or "nanotechnology", to name but a few. It is indeed important to study "disorder-to-order" and "order-to-order" phase transition in systems made of block copolymers, especially in melts and blends, and relate them to various interactions among polymer chains, different blocks, and solvent molecules. These block copolymer systems also have some potential applications such as drug carrier for cancer therapy,[1,2] templates to align metal and semiconductor nano-crystals into one-dimensional arrays.[3,4]

Various morphologies of block copolymer micelles in films and bulk have been widely studied.[5–9] The micelle formation is basically governed by the interaction among different blocks. In solutions, a selective solvent is often used to fine turn the association of the insoluble blocks, which involves the interactions between the solvent and different blocks; namely, the solubility difference. For neutral block copolymers in organic solvents, besides the loss of some translational and conformational entropies, the micelle morphology is mainly governed by a force balance among the core block attraction, the corona block repulsion, and the core–corona interfacial tension.[10] In general, such a force balance can be adjusted by tuning the copolymer molecular structure,[11,12] block composition,[13,14] copolymer concentration,[15] solvent composition,[8,16,17] and temperature.[18,19] There have already been some systematic studies on the morphological transitions of copolymer micelles among spheres, cylinders, and vesicles. The transition kinetics has also been found to depend on how the micelles are initially prepared.[20] The Bates group[21] observed a sequence of shapes from vesicles through cylinders to spheres of

poly(butadiene-*b*-ethylene oxide) (PB-*b*-PEO) diblock copolymers in water by changing the composition of the hydrophilic PEO block. Eisenberg and his coworkers[13-16,22] investigated the morphologies of poly(styrene-*b*-acrylic acid) (PS-*b*-PAA) ionic diblock copolymers in solvent mixtures of water and dimethylformamide. On the other hand, some experiments have also been devoted to the exploration of micelle morphologies in organic solvents, where the transitions from spheres to cylinders are induced by controlling the solution temperature[18] or applying an external pressure.[23,24]

More and more people realize that new cryogenic-transmission electron microscopy (cryo-TEM) is a powerful technique to freeze different morphologies of polymeric aggregate or surfactant micelles in dispersions.[6,8,21,25] However, not everyone is able to access a modern cryo-TEM, especially when organic solvents are used. Currently, many "novel" morphologies are still reported only based on TEM images without rigorous structural characterization in solutions. On the other hand, to our knowledge, there has been no systematic comparison between morphologies of polymeric micelles obtained in solutions by scattering methods and in cryo-TEM.

The micelle morphology also plays a role in block copolymer lithography, a promising potential approach for the fabrication of nano-scale materials and devices. It can lead to feature sizes down to 10–30 nm. External fields, such as electric[26,27] and magnetic fields,[28] shear,[29] and temperature gradients,[30] have been widely utilized to control the orientation and lateral ordering of the nano-scale domains in block copolymer films. Exposing copolymer films to good solvents could generate long-range equilibrium morphologies because of an increase in the chain mobility. [31] An in-depth understanding of the formation of equilibrium structures or kinetically trapped morphologies during solvent annealing requires not only a proper choice of solvents but also some judicious controls of experimental parameters, such as the vapor pressure, treatment time, and solvent extraction rate.

We previously measured the hydrodynamic force required to pull individual PS-*b*-PI chains out of each spherical micelle by forcing them through a 20-nm pore,[32] and found if the insoluble PS block is too long or the soluble PI block is too short, polymeric micelles cannot be disintegrated even under the fastest flow (200 mL/hr) available in our current setup. So we tried to swell those hard spherical micelles by addition of comment solvent THF in the solution. Before used for further

ultrafiltration of those swollen spherical micelles, LLS studies showed the presence of only spherical swollen micelles when the THF content increases and a final dissolution of the micelles into individual chains. The LLS results are consistent with thermodynamic expectation. Namely, as the solvent quality becomes better for both PS and PI, a larger core–corona interfacial area can be stabilized by the PI blocks. However, TEM imaging showed an unexplainable morphological transition from spheres through cylinders to flower-like structures when the TEM samples were prepared under ambient air at the room temperature. Such contradictive results obtained from TEM and LLS have forced us to look into the effect of the solvent evaporation rate on the TEM sample preparation. Our results reveal that different morphologies are obtainable by controlling the evaporation rate. This leads to a question "what morphologies do we want?" Our essential message is that there is no correlation between micelle structures in solutions and morphologies observed in TEM based on dilute solution-casted thin films, especially without an annealing at temperatures higher than the glass transition temperature. Therefore, one has to be careful or cautious to claim a novel morphology only based on TEM results.

3.2 Experimental Section

3.2.1 Sample preparation

Diblock copolymer PS_{170}-*b*-PI_{140} was synthesized by using high-vacuum living anionic polymerization, which was initiated by the use of *sec*-butyllithium in cyclohexane at 45 °C. The detailed synthetic procedure can be found elsewhere.[32] The resultant copolymer was characterized using size exclusion chromatography with a multi-angle laser light scattering detector, a combination of static and dynamic LLS, and proton nuclear magnetic resonance. The copolymer has a narrow size distribution with a polydispersity index of 1.06.

The solutions were prepared by adding a calculated amount of the copolymer into an appropriate volume of THF. After a complete dissolution of the copolymer into individual chains in THF, a calculated amount of *n*-hexane was added dropwise under stirring. The final THF content in the binary solvent mixture was in the range 3–25 vol%. In addition, a solution of the copolymer in pure *n*-hexane was also prepared, i.e., the 0 vol% THF content. In this study, the copolymer concentration was kept at 5.0×10^{-4} g/mL. Each resultant solution was remained at the room

temperature for more than two months to ensure that it reached its thermodynamic equilibrium state before use. Both THF and *n*-hexane were filtrated with a 0.45-μm hydrophobic polytetrafluoroethylene (PTFE) membrane filter (Millipore) before the sample preparation.

3.2.2. Laser light scattering

A commercial LLS spectrometer (ALV/DLS/SLS-5022F) equipped with a multi-τ digital time correlator (ALV5000) and a cylindrical 22-mW He-Ne laser (632.8 nm, Uniphase) as the light source was utilized to characterize the obtained copolymer micelles. Dust particles were removed by a filtration of each copolymer solution through a 0.45-μm PTFE membrane. All of the LLS experiments were performed at 25 °C. In static LLS, the weight-average molar mass, M_w, and the z-average root-mean-square radius of gyration, $<R_g^2>^{1/2}$, of polymer micelles in dilute solutions can be determined from the angular dependence of the excess absolute scattering intensity, known as the Rayleigh ratio $R_{vv}(q)$, according to

$$\frac{KC}{R_{vv}(q)} \approx \frac{1}{M_W}\left(1+\frac{1}{3}\left\langle R_g^2\right\rangle q^2\right)+2A_2C \tag{3-1}$$

where $K = 4\pi^2 n^2 (\mathrm{d}n/\mathrm{d}C)^2/(N_A\lambda_0^4)$, and $q = (4\pi n/\lambda_0)\sin(\theta/2)$ with N_A, n, θ, and λ_0 being the Avogadro number, the solution refractive index, the scattering angle, and the wavelength of the laser light in vacuum, respectively; C is the polymer concentration; and A_2 is the second virial coefficient.

In dynamic LLS, the Laplace inversion of each measured intensity–intensity time correlation function $G^{(2)}(t,q)$ in the self-beating mode gives a line-width distribution function $G(\Gamma)$. For a pure diffusive relaxation, Γ is related to the translational diffusion coefficient D by $\Gamma = Dq^2$ when $q \to 0$ and $C \to 0$. D is further related to the hydrodynamic radius R_h by the Stokes-Einstein equation, $R_h = k_B T/(6\pi\eta D)$, where k_B, T, and η are the Boltzmann constant, the absolute temperature, and the solvent viscosity, respectively.

3.2.3 TEM Imaging

The TEM imaging was performed on an FEI CM120 microscope operated at 120 kV. The TEM samples were prepared in three ways. They are named as the fast, normal, and slow evaporation. For the fast evaporation, the samples were prepared by placing 10-μL drops of the copolymer solutions onto carbon-coated copper grids, followed

by drying in ambient air with a hair dryer. For the normal evaporation, the copolymer solution droplets deposited on copper grids were dried naturally in air at room temperature. For the slow evaporation, a glass beaker was first filled with the binary solvent mixture that was used to make the copolymer solution. A solid support was placed in the beaker, with the top of the support kept above the surface of the liquid solvent. A copper grid was then transferred onto the support in the beaker. The beaker was hermetically covered and kept still for 30 min to let the top part of the beaker filled with the saturated vapor. A 10-μL drop of the copolymer solution was then placed onto the copper grid through a syringe, followed by drying in the solvent vapor overnight. Under the fast, normal, and slow evaporation conditions, the solution droplets on the copper grids were seen to disappear after a few seconds, ~3 min, and ~30 min, respectively. The as-prepared samples on copper grids were kept in a desiccator for 1–3 days before the TEM imaging.

3.3 Results and Discussion

Figure 3.1 shows that as the THF content increases from 0 to 19 vol%, the morphology has gradually developed from spherical to cigar-shaped micelles, then to worm-like cylindrical micelles, and finally to an exotic flower-like structures made of twisted long cylindrical micelles, where these samples for the TEM observation were prepared by depositing each PS-*b*-PI copolymer solution on copper grids and let it dry in ambient air at the room temperature. Such observed morphologies are reproducible and can be divided into five categories as a function of the THF content. Namely, (1) when the THF content is less than 10 vol%, only spherical micelles with an average size of ~30 nm are observed in TEM (Figure 3.1A); (2) in the range 11–14 THF vol%, spherical and cigar-shape micelles coexist (Figure 3.1B); (3) when the THF content increases to 15–18 vol%, worm-like long cylindrical micelles are clearly visible (Figure 3.1C); (4) Further increase of the THF content to 19–22 vol% results in a flower-like structure made of twisted long cylindrical micelles (Figure 3.1D); and (5) finally, as expected, polymeric micelles completely dissolve into individual copolymer chains in the solvent mixture when the THF content reaches ~22 vol% or higher. In general, a thin film made of block copolymer chains confined between the copolymer-substrate and copolymer-air interfaces can undergo both the

surface relaxation and reconstruction. The interfacial interaction between a polymer solution and a substrate, such as the wetting/dewetting effect, can also influence the morphology formation on a substrate. Note that in the current study, all the TEM samples are prepared on the copper grid coated with carbon so that the contribution of the interfacial interaction between the solution and substrate remains the same.

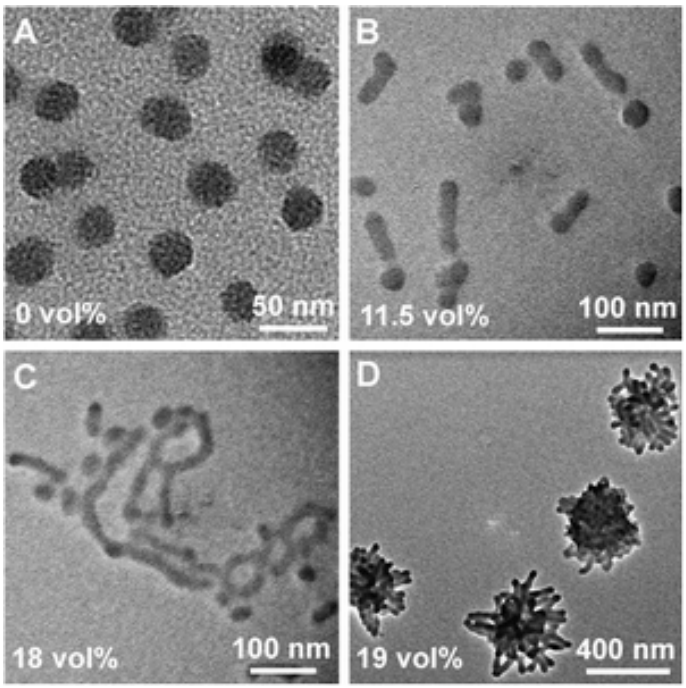

Figure 3.1. TEM images from samples prepared by casting a solution of copolymer PS_{170}-*b*-PI_{140} in different mixtures of *n*-hexane and THF: (A) pure *n*-hexane; (B) 11.5 vol% of THF; (C) 18 vol% of THF; and (D) 19 vol% of THF, where samples were prepared under a normal evaporation rate.

It is worth-noting that throughout such a morphological transition, the average diameters of spherical and cylindrical micelles remain similar (~26 nm) in TEM imaging. Initially, we were attracted by such a systematical morphological transition, especially the formation of the flower-like structure in which each loop on its periphery is clearly made of a twisted and folded cylindrical micelle when Figure 3.1D is enlarged. However, when really thinking about such a change, we found that such a phase transition contradicts our general understanding of the formation of polymeric micelles with different morphologies. Thermodynamically, when a common good solvent is added into a solvent selectively poor for one block, the solubility of that block increases so that the interfacial energy between the soluble

and insoluble blocks should decrease. In other words, the soluble blocks should be able to stabilize a larger interface area. The direction of increasing the interface area should follow the change from a lamellar structure to cylindrical micelles and then from cylindrical micelles to spherical micelles; namely, as the THF content increases, we would see the breakdown of long cylindrical micelles into small spherical micelles, not the other way around as shown in Figure 3.1. Such a contradiction led us to the current study; namely, using a combination of static and dynamic LLS to examine their morphologies in different solvent mixtures in the solution state.

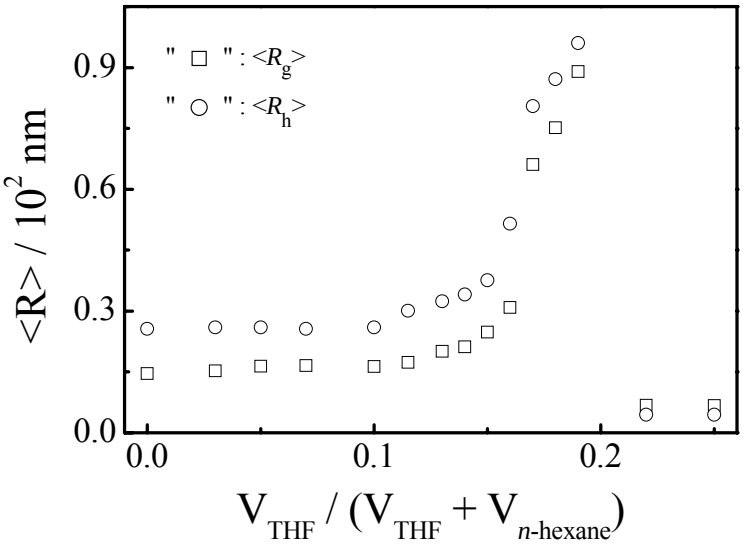

Figure 3.2. THF content dependent average hydrodynamic radius $<R_h>$ and radius of gyration $<R_g>$ of diblock copolymer in a mixture of THF and *n*-hexane

Figure 3.2 shows that both $<R_h>$ and $<R_g>$ of the copolymer micelles gradually increase with the THF content when it is below 15 vol%. Further increase of the THF content first leads to a sharp increase in both $<R_h>$ and $<R_g>$ and then followed by an abrupt drop when the THF content reaches ~22%, revealing the dissolution of each copolymer micelle into individual chains. Note that each LLS measurement was only performed after the copolymer solution reached a steady state that was assessed by monitoring the intensity of the light scattered from the solution as a function of time after the solvent mixing. Surprisingly, the equilibrating process is rather slow even in the solution, typically taking 1–2 months for each copolymer solution to reach its steady state in the solvent mixture. Literature search shows that

such a point has been overlooked in the past to some extent. Likely, some of previous studies might be conducted when the copolymer solution mixtures were not in their thermodynamically stable states. Apparently, the results in Figure 3.2 agree well with those from the TEM measurements; namely, the average size of the scattering subjects, measured in both static and dynamic LLS, presumably polymeric micelles according to the TEM imaging, increases as the THF content increases in the solvent mixture.

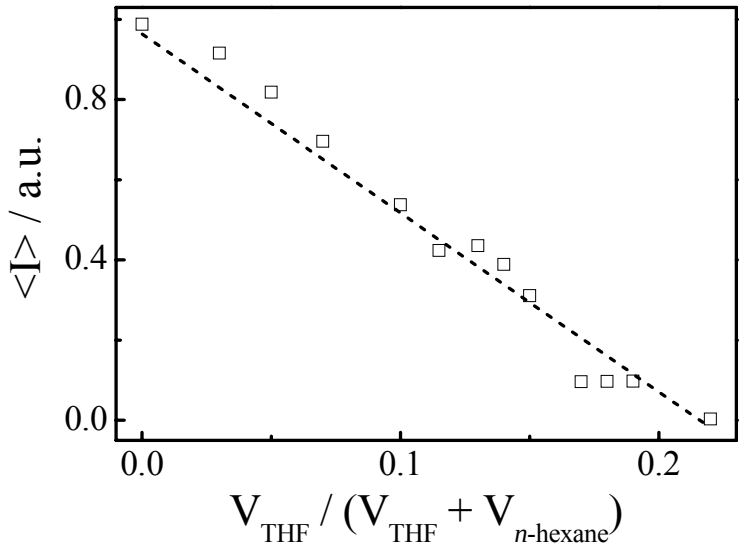

Figure 3.3. THF content dependent time-averaged scattered light intensity <*I*> of diblock copolymer in a mixture of THF and *n*-hexane, where scattering angle is 20^{o} and the dash line just guides eyes.

However, Figure 3.3 shows that the time-averaged intensity of the light scattered from the copolymer micelles in the solvent mixture decreases linearly as the THF content increases. Note that in eq 3-1, $R_{vv}(q) \sim \langle I \rangle \sim M_w$ when $q = 0$ and $C = 0$; and $M_w = \Sigma_i n_i M_i^2 / \Sigma_i n_i M_i$, where n_i and M_i are the number and molar mass of the *i*th scattering subject, respectively. Polymeric micelles are often narrowly dispersed so that $M_w \simeq M_{chain} N_{ass}$, where M_{chain} and N_{ass} are the average molar mass of the chains and the average number of the chains inside each micelle, respectively. For a given copolymer concentration, the decrease of <*I*> can be roughly related to the decrease of N_{ass} since M_{chain} is a constant. After correcting the value of differential refractive index increment (dn/dC) for each solvent mixture and extrapolating <*I*> to

$q = 0$, we can convert the THF content dependent $<I>_{q=0}$ to its corresponding M_w on the basis of eq 3-1 and then calculate N_{ass} since $N_{ass} = M_w/M_{chain}$.

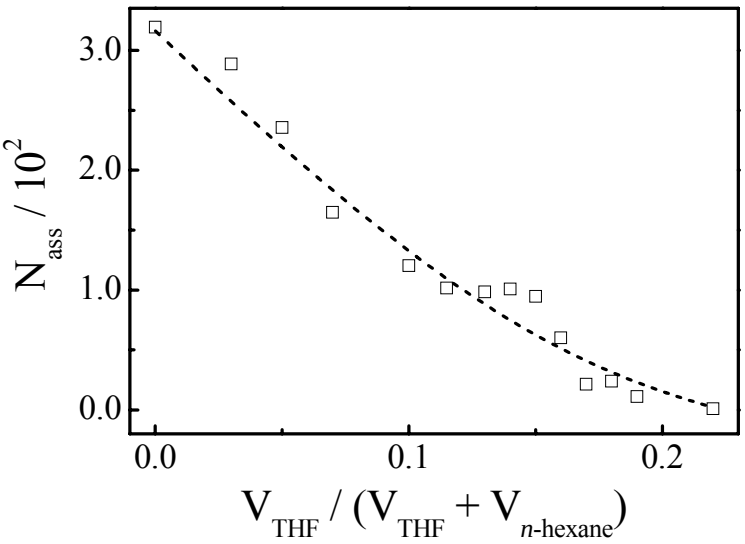

Figure 3.4. THF content dependent association number (N_{ass}) of diblock copolymer in a mixture of THF and *n*-hexane, where the dash line just guides eyes.

Figure 3.4 shows that N_{ass} gradually decreases from ~320 in pure *n*-hexane to ~30 in 19 vol% of THF, and finally becomes one when the THF content reaches ~22 vol%, where we did not subtract the critical association concentration (CAC) of the coplymer in the solvent mixture when calculating M_w because it is extremely low. In principle, the addition of a common good solvent into a selective solvent, in which a diblock copolymer forms spherical micelles, should result in the formation of smaller spherical micelles with a less number of chains inside each micelle if the two solvents are completely mixable because the decrease of the interfacial energy; namely, we would see smaller micelles and a decrease of N_{ass} when the THF content increases in the solvent mixture.

However, Figure 3.2 shows an opposite trend, i.e., the size increases. On the other hand, the increase of the size of the scattering subjects could be due to the fusion of spherical micelles together to form different morphologies, as shown in Figure 3.1. In contrast, a comparison of Figures 3.3 and 3.4 shows that N_{ass} decreases when $<R_g>$ and $<R_h>$ increases, clearly revealing that the size increase with the THF content in Figure 3.2 is not due to formation of cigar-shape or long cylindrical micelles or the flower-like structure in the copolymer solution. The only explanation should be the

preferential partition of THF in the PS core because it is an extremely good solvent for PS. To further illustrate possible structures of the chain aggregates in the solution, we calculate the THF content dependent ratio of $\langle R_g \rangle / \langle R_h \rangle$ because it directly reflects the mass distribution of the copolymer chains in space, i.e., the structure of the micelles.

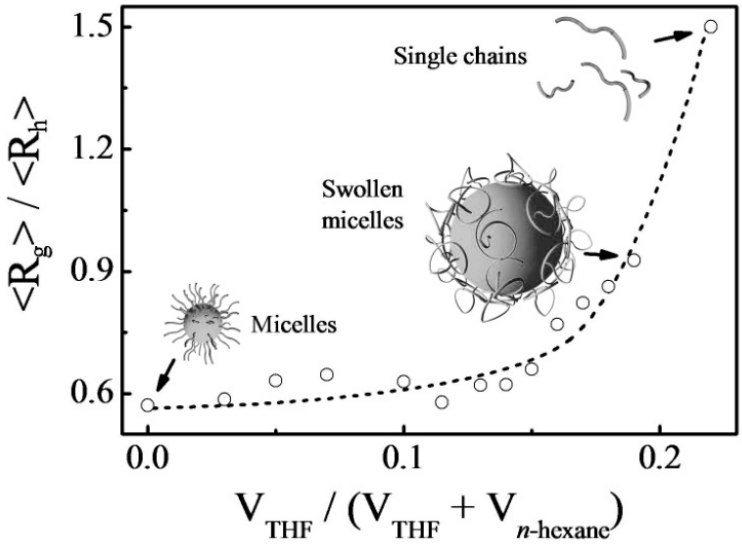

Figure 3.5. THF content dependence of ratio of average radius of gyration to average hydrodynamic radius $\langle R_g \rangle / \langle R_h \rangle$ of diblock copolymer in a mixture of THF and *n*-hexane, where the dash line just guides eyes

Figure 3.5 shows that $\langle R_g \rangle / \langle R_h \rangle$ slightly increases in the THF content range 0-15 vol%, but around ~0.6, even smaller than 0.774, predicted for a uniform solid sphere. Such a smaller $\langle R_g \rangle / \langle R_h \rangle$ value is expected for polymeric micelles with a dense core and a relatively loose shell; namely, the loose shell contributes more to $\langle R_h \rangle$ but less to $\langle R_g \rangle$ in comparison with a uniform sphere with an identical radius of $\langle R_h \rangle$. Further increase of the THF content in the range 17-19 vol% leads to a steep increase of $\langle R_h \rangle$ from ~35 to ~90 nm, indicating the swelling of individual copolymer micelles. Meanwhile, $\langle R_g \rangle / \langle R_h \rangle$ increases from 0.7 to 0.9, smaller than 1.0, a value predicted for a hollow sphere with an infinite thin wall. The increase of $\langle R_g \rangle / \langle R_h \rangle$ to ~0.9 indicates that the PS core of each micelle is highly swollen with THF, as schematically shown in Figure 3.5. Finally, when the THF content reaches ~22 vol%, both $\langle R_h \rangle$ and $\langle R_g \rangle$ drop to few nanometers (Figure 3.2) and $\langle R_g \rangle / \langle R_h \rangle$

increases to ~1.5-1.6, a value predicted for a random coiled chain in good solvent, clearly revealing that the completely dissolution of the micelles.

Further, we can estimate the THF content dependence of the average radius of the micelle core ($\langle R\rangle_{core}$), the shell thickness ($\Delta R_{shell} = \langle R_h\rangle - \langle R\rangle_{core}$) and the average chain density inside each micelle ($\langle\rho\rangle_{micelle} = M_w/(4\pi\langle R_h\rangle^3 N_A/3)$ by combining static and dynamic LLS results together. Previously, after assuming that a core-shell micelle has a uniform core and shell with different chain densities, we were able to estimate $\langle R\rangle_{core}$ from its $\langle R_g\rangle/\langle R_h\rangle$.[33]

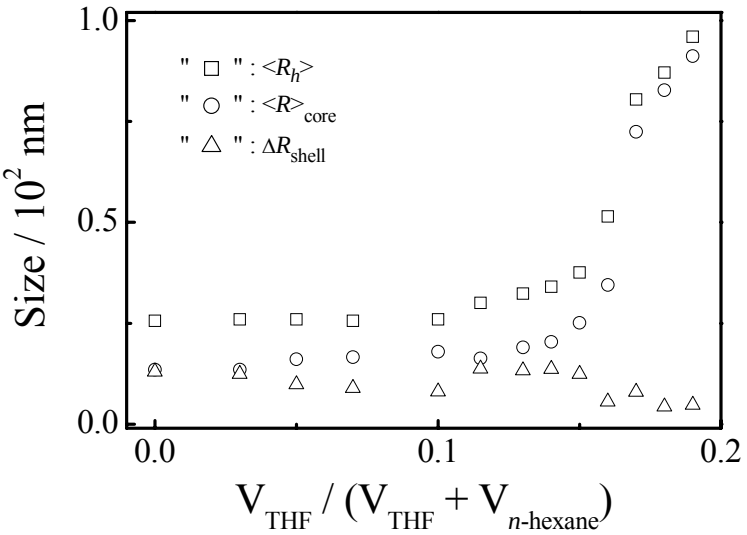

Figure 3.6. THF content dependence of average radius of the core ($\langle R\rangle_{core}$) and shell thickness (ΔR_{shell}) of spherical micelles in a mixture of THF and *n*-hexane, where we re-plot $\langle R_h\rangle$ just for comparison, especially in the high swollen state (19 vol% of THF)

Figure 3.6 shows that initially, the shell and the core have a similar size, but $\langle R\rangle_{core}$ increases while ΔR_{shell} slightly decreases as the THF content increases in the range 0-10 vol%. Further increase of the THF content leads to a much high degree of swelling of the core. The results in Figure 3.6 directly reveal that THF swells the PS core, presumably due to the preferential partition of THF inside the PS block, and the slight contraction of the stretched PI blocks in the shell when the core is large. A combination of Figures 3.2, 3.4 and 3.6, i.e., $\langle R\rangle_{core}$, ΔR_{shell} and N_{ass}, enables us to estimate the chain densities of the core and the shell ($\langle\rho\rangle_{core}$ and $\langle\rho\rangle_{shell}$), respectively from $M_{PS}N_{ass}/(4\pi\langle R_{core}\rangle^3 N_A/3)$ and $M_{PI}N_{ass}/[4\pi(\langle R_h\rangle^3 - \langle R\rangle_{core}^3)N_A/3]$.

Figure 3.7 shows a large decrease of $<\rho>_{core}$ as the THF content increases, further indicating that the core is gradually swollen and become less dense due to the preferential partition of THF in the core. Figure 3.7 also shows that $<\rho>_{shell}$ decreases in the same THF range. This is because the increase of the THF content leads to the decrease of N_{ass} and the increase of $<R_h>$, but ΔR_{shell} nearly remains constant.

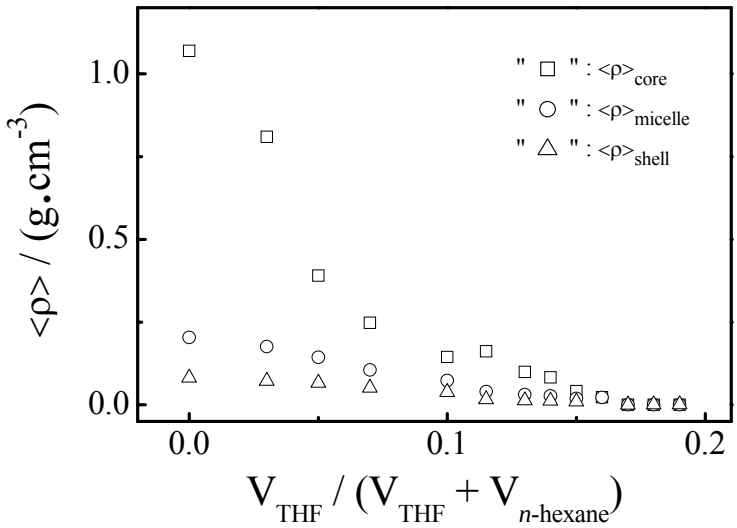

Figure 3.7. Variations of the average densities of the spherical micelle ($<\rho>_{micelle}$), its core ($<\rho>_{core}$) and shell ($<\rho>_{shell}$) as a function of the THF content

The above LLS results unambiguously demonstrate an expected PS-core-swelling process as a common good solvent (THF) is mixed with *n*-hexane (a solvent selectively poor for PS). During the swelling process, the morphology of the diblock copolymer micelles remains spherical. There is no surprising from the thermodynamic point of view. As the quality of the solvent mixture becomes better for the PS block, the interfacial energy between the PS core and PI shell reduces. As a result, the given amount of the PI blocks can stabilize a larger interfacial area, resulted from the preferential partition of THF in the PS core. The apparent disagreement between the TEM and LLS results leads us to conclude that those non-spherical morphologies must be formed during the TEM sample preparation. Actually, the control of the solvent evaporation was utilized to alternate the micelle morphology and the orientation and lateral ordering of the domains made of block copolymers.[34-39]

In order to test such an effect of the solvent evaporation rate, we purposely prepared the TEM samples in three different ways when the THF content is in the range 11 to 22 vol%; namely, 1) very quick evaporation in air by drying each sample with a hair dryer; 2) normal evaporation in ambient air at the room temperature; and 3) very slow evaporation in the saturated vapor of the solvent mixture. The procedures have been detailed in the Section of the TEM sample preparation.

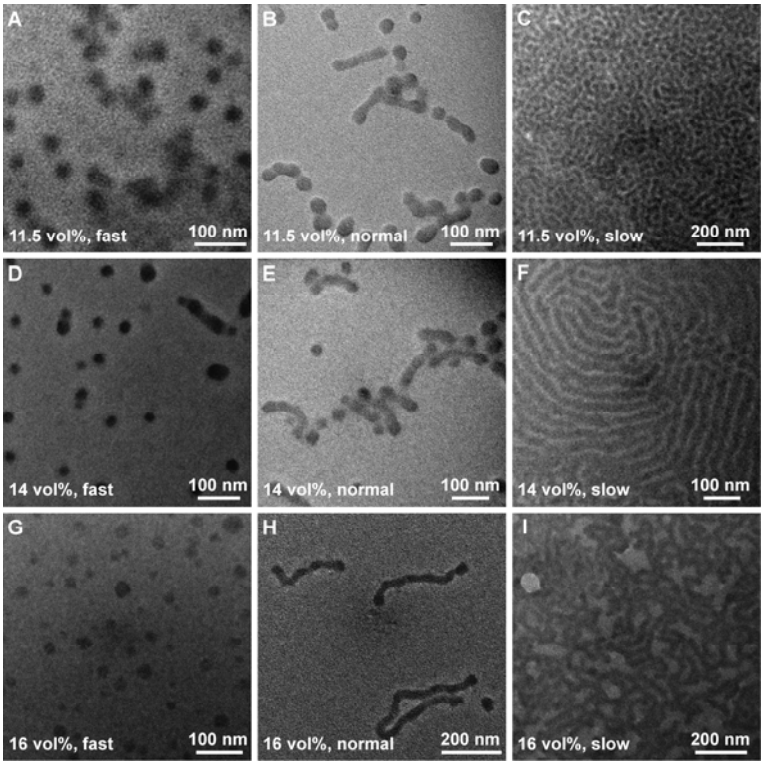

Figure 3.8. TEM images of micelle samples obtained from the solution containing 11.5 vol%, 14 vol% and 16 vol% THF under different solvent evaporation rates respectively

Figure 3.8 show that when the THF content is 11.5 vol%, 14 vol% and 16 vol%, the copolymer samples prepared with the normal evaporation rate show both spherical and cylindrical micelles (Figure 3.8B, 3.8E and 3.8H), while for higher THF contents, long cylindrical micelles are clearly formed. The cylindrical micelles in these samples have an average diameter of ~26 nm.

The effect of the evaporation rate is obvious, resulting in dramatically different micelle morphologies. As expected, the very quick evaporation rate enables us to frozen and capture spherical morphology of the micelles in the solutions with an average diameter of ~25 nm, especially when the THF content is relatively low

(Figure 3.8A). This is because individual micelles in the solution have no sufficient time to fuse together. In the presence of more THF, the copolymer chains are more mobile inside each spherical micelle in the solution so that it is easier for them to fuse together to form cigar-shape micelles. This is why for the samples prepared with 14 and 16 vol% THF, spherical micelles are dominant but a small amount of fused micelles are also observable (Figures 3.8D and 3.8G). Note that a considerable fraction of the spherical micelles are larger, presumably due to the fusion of several smaller ones together. On the other hand, the very slow evaporation results in the morphologies which are more close to the thermodynamically stable state in the copolymer melt; namely, long cylindrical micelles and even lamellar structure (Figures 3.8C, 3.8F and 3.8I). The cylindrical micelles or the lamellar structure in these samples have a slightly smaller average diameter or layer space of ~22 nm, which is reasonable because a cylindrical micelle has a less space-filling problem than a spherical one for a given diblock copolymer.

A comparison of the results of LLS and TEM, obtained with different evaporation rates, clearly shows that there are only spherical micelles in the copolymer solutions, which agrees with the reported phase diagram.[40] The cylindrical micelles and the flower-like structure (Figure 3.1) are formed during the drying process in the TEM sample preparation, which involves two important processes;[41,42] namely, the evaporation of solvent and the fusion of small spherical micelles. The boiling points of THF and *n*-hexane are 66 and 69 °C, respectively. After the copolymer solution is deposited on the copper grid, the two solvents start to evaporate with a similar rate.

The solvent evaporation is characterized by the evaporation time constant (τ_e), which can be controlled by the drying condition. The fusion of two spherical micelles together is governed by two characteristic times; namely, the interaction time (τ_i) and the fusion time (τ_f). τ_i is related to the diffusion time and the inter-micelle interaction distance; while τ_f mainly depends on the mobility (relaxation) of the chains in each micelle. When $\tau_i << \tau_f$, each micelle behaves like a tiny glass ball so that the fusion is kinetically prohibited and the micelles are stabilized by the viscoelastic effect.[43-47] During the solvent evaporation, small spherical micelles are pushed together so that τ_i increases. The addition of a common good solvent looses the core and increases the solubility of the PS blocks inside so

that τ_f decreases. This explains why small spherical micelles are fused together to form structures with different morphologies when THF is added in the copolymer solution. On the other hand, if $\tau_f >> \tau_e$, spherical micelles formed in the solution are frozen during the TEM sample preparation.

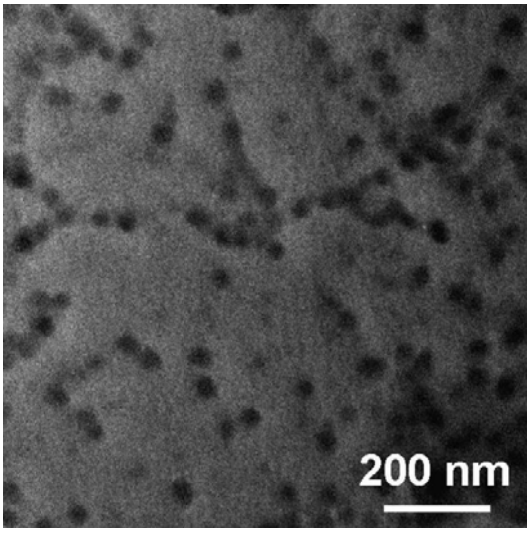

Figure 3.9. TEM image of a micelle sample prepared by freeze drying of a solution of copolymer in a mixture of *n*-hexane and THF (16 vol%)

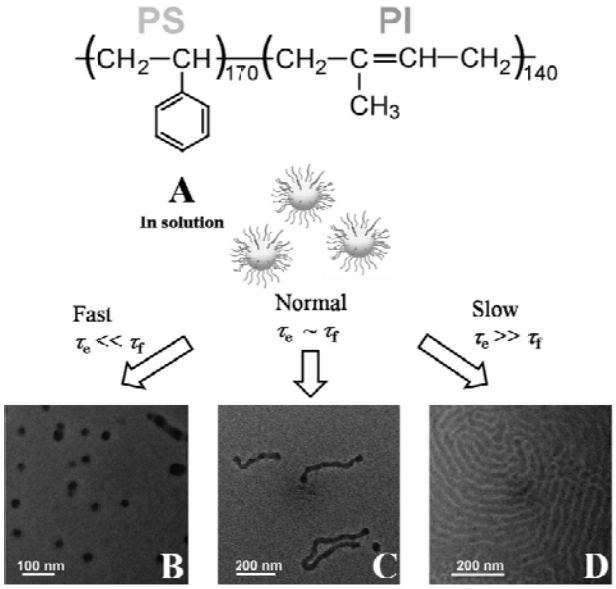

Figure 3.10. Schematic of solvent evaporation rate-induced morphological transition of diblock PS-*b*-PI micelles in a mixture of THF and *n*-hexane: (A) Spherical; (B) partially fused spherical micelles; (C) formation of cylindrical micelles; and (D) formation of long cylindrical micelles or lamellar structures.

Practically, in order to obtain a true morphology of polymeric micelles/aggregates in dispersion, one should use a Cryo-TEM or a combination of freeze drying of a solution and a normal room-temperature TEM. Namely, 1) placing a TEM copper grid on the bottom of a glass cell; 2) transfer a small amount (250 μL or less) of polymer solution into the cell to make sure that the grid is completely immerged in the solution; 3) inserting the glass cell into liquid nitrogen to quickly freeze the solution into a solid; 4) transferring the solution in its frozen solid state into a freeze-drying device; 5) removing solvent directly from its solid state to its vapor state without melting; and 6) imaging its morphology in a normal TEM at the room temperature after the solvent is completely removed. By following the above procedure, we were able to obtain the true spherical morphology of the polymeric micelles in the solvent mixture (16 vol% THF), as shown in Figure 3.9, without any visible cylindrical micelles. Figure 3.10 schematically summarizes our discussion about how diblock PS-*b*-PI micelles with different morphologies are formed in the solvent mixture and in the TEM sample preparation with different solvent evaporation rates.

3.4 Conclusion

A comparative study of the micelle formation of poly(styrene-*b*-isoprene) (PS_{170}-*b*-PI_{140}) diblock copolymer in different binary solvent mixtures of THF and *n*-hexane by laser light scattering (LLS) and the morphologies observed in transmission electron microscope (TEM) reveals that there are only spherical micelles in the solution. The addition of a common good solvent (THF) gradually swells the PS core so that the size of the micelles increases, and at the same time, gradually dissolves the micelles so that the average number of the chains inside each micelle decreases. The cigar-sharp and long cylindrical micelles as well as the exotic flower-like structure observed in TEM at the room temperature are simply formed during the solvent evaporation process in the TEM sample preparation. The formation of different morphologies is governed by the solvent evaporation rate and the micelle fusion and interaction times. Our current results clearly demonstrate that it is really necessary and vitally important to combine different methods, instead of using only a normal TEM to characterize the morphologies of block copolymer

micelles in solution, especially when computer simulations are compared with the morphologies generated from a copolymer solution. Fairly speaking, more and more people are realizing that it is really necessary to use cryogenic-transmission electron microscopy (cryo-TEM) to characterize different morphologies formed in polymer solutions. However, there still lack sufficient attention in this aspect, partially due to the fact that most of researchers are not able to access cryo-TEM at this moment, especially when organic solvents are used. Our current study serves as a further alarm to those who are interested in morphologies of block copolymers in solutions. We have demonstrated that, instead of cryo-TEM, one could use the freeze-drying method described in this paper to prepare TEM samples, which can lead to a better description of morphologies in solutions if it is done properly. It should be noted that the kinetic effect discussed here is not completely evil because we can play it to obtain some desired morphologies or nanostructures for various potential applications.

3.5 References and Notes

(1) O. Benny, O. Fainaru, A. Adini, F. Cassiola, L. Bazinet, I. Adini, E. Pravda, Y. Nahmias, S. Koirala, G. Corfas, R. J. D'Amato, J. Folkman, *Nat. Biotechnol* **2008**, *26*, 799.

(2) J. A. MacKay, M. N. Chen, J. R. McDaniel, W. G. Liu, A. J. Simnick, A. Chilkoti, *Nat. Mater* **2009**, *8*, 993.

(3) H. Wang, W. J. Lin, K. P. Fritz, G. D. Scholes, M. A. Winnik, I. Manners, *J. Am. Chem. Soc* **2007**, *129*, 12924.

(4) H. Wang, X. S. Wang, M. A. Winnik, I. Manners, *J. Am. Chem. Soc* **2008**, *130*, 12921.

(5) X. H. Yan, F. T. Liu, Z. Li, G. J Liu, *Macromolecules* **2001**, *34*, 9112.

(6) S. Jain, F. S. Bates, *Science* **2003**, *300*, 460.

(7) E. B. Zhulina, M. Adam, I. LaRue, S. S. Sheiko, M. Rubinstein, *Macromolecules* **2005**, *38*, 5330.

(8) J. Bang, S. Jain, Z. B. Li, T. P. Lodge, J. S. Pedersen, E. Kesselman, Y. Talmon, *Macromolecules* **2006**, *39*, 1199.

(9) T. Smart, H. Lomas, M. Massignani, M. V. Flores-Merino, L. R. Perez, G. Battaglia, *Nano Today* **2008**, *3*, 38.

(10) A. Halperin, M. Tirrell, T. P. Lodge, *Adv. Polym. Sci.* **1992**, *100*, 31.

(11) E. Minatti, P. Viville, R. Borsali, M. Schappacher, A. Deffieux, R. Lazzaroni, *Macromolecules* **2003**, *36*, 4125.

(12) N. Ouarti, P. Viville, R. Lazzaroni, E. Minatti, M. Schappacher, A. Deffieux, R. Borsali, *Langmuir* **2005**, *21*, 1180.

(13) L. F. Zhang, A. Eisenberg, *Science* **1995**, *268*, 1728.

(14) L. F. Zhang, A. Eisenberg, *J. Am. Chem. Soc.* **1996**, *118*, 3168.

(15) L. F. Zhang, A. Eisenberg, *Macromolecules* **1999**, *32*, 2239.

(16) Y. S. Yu, L. F. Zhang, A. Eisenberg, *Macromolecules* **1998**, *31*, 1144.

(17) H. Y. Huang, R. Hoogenboom, M. A. M Leenen, P. Guillet, A. M. Jonas, U. S. Schubert, J. F. Gohy, *J. Am. Chem. Soc.* **2006**, *128*, 3784.

(18) I. LaRue, M. Adam, M. Pitsikalis, N. Hadjichristidis, M. Rubinstein, S. S. Sheiko, *Macromolecules* **2006**, *39*, 309.

(19) P. Bhargava, Y. F. Tu, J. X. Zheng, H. M. Xiong, R. P. Quirk, S. Z. D. Cheng, *J. Am. Chem. Soc.* **2007**, *129*, 1113.

(20) K. Iyama, T. Nose, *Macromolecules* **1998**, *31*, 7356.

(21) Y. Y. Won, A. K. Brannan, H. T. Davis, F. S. Bates, *J. Phys. Chem. B* **2002**, *106*, 3354.

(22) H. W. Shen, L. F. Zhang, A. Eisenberg, *J. Am. Chem. Soc.* **1999**, *121*, 2728.

(23) Q. J. Chen, H. Zhao, T. Ming, J. F. Wang, C. Wu, *J. Am. Chem. Soc.* **2009**, *131*, 16650.

(24) F. Sterpone, G. Briganti, S. Melchionna, C. Pierleoni, *Langmuir* **2008**, *24*, 6067.

(25) Y. Talmon, *J. Colloid Interf. Sci.*, **1983**, *93)*, 366.

(26) T. Xu, Y. Q. Zhu, S. P. Gido, T. P. Russell, *Macromolecules* **2004**, *37*, 2625.

(27) K. Schmidt, H. G. Schoberth, M. Ruppel, H. Zettl, H. Hänsel, T. M. Weiss, V. Urban, G. Krausch, A. Böker, *Nat. Mater.* **2008**, *7*, 142.

(28) C. Osuji, P. J. Ferreira, G. P. Mao, C. K. Ober, J. B. Vander Sande, E. L. Thomas, *Macromolecules* **2004**, *37*, 9903.

(29) M .M. Mok, S. Pujari, W. R. Burghardt, C. M. Dettmer, S. T. Nguyen, C. J. Ellison, J. M. Torkelson, *Macromolecules* **2008**, *41*, 5818.

(30) D. E. Angelescu, J. H. Waller, D. H. Adamson, R. A. Register, P. M. Chaikin, *Adv. Mater.* **2007**, *19*, 2687.

(31) S. H. Kim, M. J. Misner, T. Xu, M. Kimura, T. P. Russell, *Adv. Mater.* **2004**, *16*, 226.

(32) L. Z. Hong, F. Jin, J. F. Li, Y. J. Lu, C. Wu, *Macromolecules* **2008**, *41*, 8220.

(33) Y. F. Tu, X. H. Wan, D. Zhang, Q. F. Zhou, C. Wu, *J. Am. Chem. Soc.* **2000**, *122*, 10201.

(34) S. H. Kim, M. J. Misner, T. Xu, M. Kimura, T. P. Russell, *Adv. Mater.* **2004**, *16*, 226.

(35) G. Kim, M. Libera, *Macromolecules* **1998**, *31*, 2569.

(36) G. Kim, M. Libera, *Macromolecules* **1998**, *31*, 2670.

(37) K. Fukunaga, H. Elbs, R. Magerle, G. Krausch, *Macromolecules* **2000**, *33*, 947.

(38) K. Fukunaga, T. Hashimoto, H. Elbs, G. Krausch, *Macromolecules* **2002**, *35*, 4406.

(39) A. Turturro, E. Gattiglia, P. Vacca, G. T. Viola, *Polymer* **1995**, *36*, 3987.

(40) A. K. Khandpur, S. Förster, F. S. Bates, I. W. Hamley, A. J. Ryan, W. Bras, K. Almdal, K. Mortensen, *Macromolecules* **1995**, *28*, 8796.

(41) H. G. Cui, Z. Y. Chen, K. L. Wooley, D. J. Pochan, *Macromolecules* **2006**, *39*, 6599.

(42) H G. Cui, Z. Y. Chen, S. Zhong, K. L. Wooley, D. J. Pochan, *Science* **2007**, *317*, 647.

(43) M. H. Siu, H. Y. Liu, X. X. Zhu, C. Wu, *Macromolecules* **2003**, *36*, 2103.

(44) M. H. Siu, C. He, C. Wu, *Macromolecules* **2003**, *36*, 6588.

(45) C. Wu, W. Li, X. X. Zhu, *Macromolecules* **2004**, *37*, 4989.

(46) H. W. Chen, Q. J. Zhang, J. F. Li, Y. W. Ding, G. Z. Zhang, C. Wu, *Macromolecules* **2005**, *38*, 8045.

(47) G. Z. Zhang, C. Wu, *Adv. Polym. Sci.* **2006**, *195*, 101.

Chapter 4
Nanopore Extrusion-Induced Transition from Spherical to Cylindrical Block Copolymer Micelles

4.1 Introduction

Cylindrical micelles made of soluble and insoluble segments have been attracting increasing attention owing to their many interesting applications. They can function as templates to align inorganic nanocrystals into one-dimensional arrays[1] and fabricate polymer–silica[2] and polymer–metal oxide nanowires.[3] Cylindrical micelles containing peptides have been shown to be able to direct the mineralization of hydroxyapatite with controlled crystalline orientations[4] and induce rapid differentiation of neural progenitor cells.[5] Moreover, cylindrical micelles are also useful for sustained drug release.[6] They have been demonstrated to persist in the circulation up to one week after intravenous injection, which is about ten times longer than the corresponding spherical ones.[7]

The formation of cylindrical micelles has typically been realized by designing the block copolymer molecular structures and varying the molecular weights of the soluble and insoluble segments.[8] The transition from spherical to cylindrical micelles can also be induced by changing the solvent and temperature. Moreover, some unconventional means for the preparation of cylindrical micelles have recently been demonstrated, including kinetic control,[9] the use of interfacial instabilities,[10] and aromatic oxidation.[11] Herein we report on a new and facile method for transforming spherical to cylindrical micelles. The transformation is achieved by extruding the spherical micelles through nanoscale pores (Figure 4.1a). The extrusion process allows for continuous and large-scale production of cylindrical micelles.

4.2 Results and Discussion

We used polystyrene-*b*-polyisoprene (PS_{170}-*b*-PI_{140}) diblock copolymer with a polydispersity index of 1.06.[12,13] We previously measured the force required to pull individual chains out of each spherical micelle formed in pure *n*-hexane.[13] In this experiment, the copolymer was first dissolved in tetrahydrofuran (THF). *n*-hexane was then added dropwise under stirring until the concentration of THF was reduced to 2.8 vol%. The final concentration of the copolymer was 5×10^{-4} g/mL. The copolymer solution was kept at room temperature for more than 3 months before use. Our extrusion setup is composed of an SGE gas tight syringe and a Whatman 10-mm-diameter membrane. The membrane has a double layer structure.[13,14] One layer is 59-μm thick and contains 200-nm pores, and the other layer is 1-μm thick and contains 20-nm pores. On average, each small pore is covered by a large pore, with a pore density of $\sim 5 \times 10^{8}$ cm^{-2}. During the extrusion operation, the membrane was positioned with the large-pore layer facing the incoming solution. The flow rate of the copolymer solution through the membrane was controlled with a Harvard PHD 2000 syringe pump. The extrusion was performed at room temperature. The variation of temperature will alter the solvent quality. Our results show that the workable range for the extrusion to produce cylindrical micelles is ~2–6 vol% of THF. If the interaction of the PS blocks in the core is too strong, it will be difficult to push the spherical micelles through the nanopores. If the interaction is too weak, no spherical micelles will be formed.

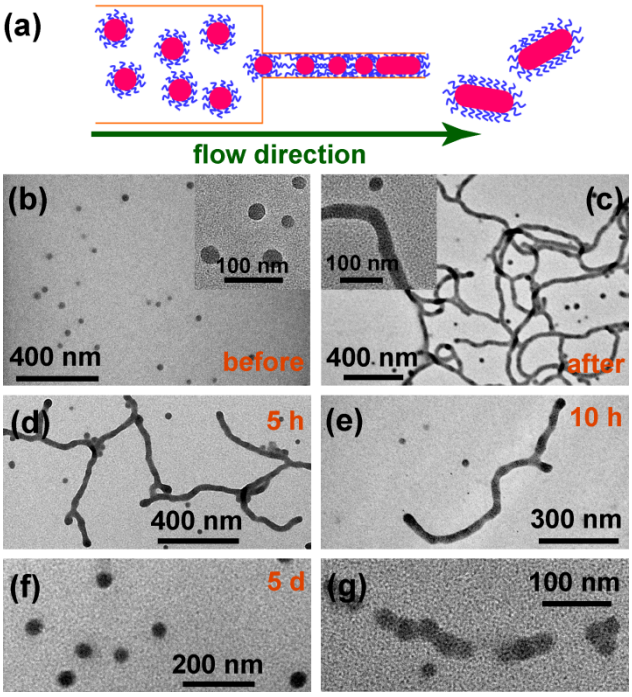

Figure 4.1. (a) Schematic showing the extrusion process. (b) TEM (FEI CM120) image of the micelles before the extrusion. (c) TEM image of the micelles obtained after the extrusion. The insets are the corresponding zoomed-in images (FEI Tecnai T20). (d–f) TEM images of the micelles obtained at 5 h, 10 h, and 5 d, respectively, after the extrusion. (g) High-magnification TEM image acquired right after the extrusion. The flow rate of the copolymer solution is 40 mL/h. The micelle solutions were directly dropcast on carbon film-supported copper grids and dried in air.

Transmission electron microscopy (TEM) imaging was performed to characterize the copolymer micelle morphologies. Figure 4.1b shows a representative TEM image of the micelles formed in the initial solution. All of the micelles are spherical. After the micelle solution was extruded through the membrane, a number of cylindrical micelles were observed (Figure 4.1c). They are entangled together, with lengths of up to several micrometers. The average diameters of the spherical and cylindrical micelles measured from their high-magnification TEM images (Figure 4.1b,c, insets) are (28 ± 5) and (33 ± 4) nm, respectively. They are nearly the same within the experimental uncertainties.

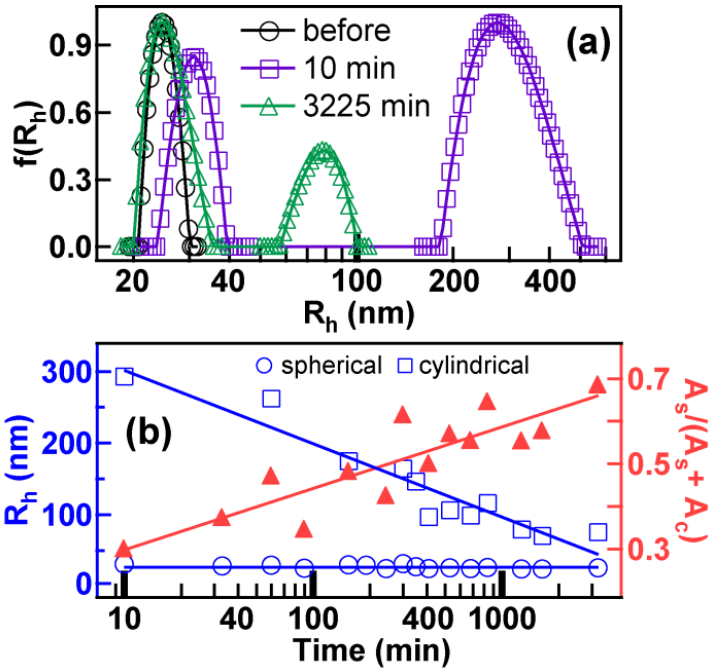

Figure 4.2. (a) Normalized hydrodynamic radius distributions $f(R_h)$ obtained before and at 10 and 3225 min after the extrusion. The solution flow rate is 40 mL/h. (b) Left axis: dependence of the hydrodynamic radii of the spherical (circles) and cylindrical (squares) micelles on the elapsed time after the extrusion. Right axis: dependence of the contribution of the spherical micelles (triangles) on the elapsed time. A_s and A_c are the peak areas of the spherical and cylindrical micelles on the $f(R_h)$ plots, respectively. The lines are guides to the eye.

Dynamic light scattering (DLS) was also carried out to probe the copolymer micelles. An ALV 5022F spectrometer equipped with a time correlator and a He–Ne laser (632.8 nm, 22 mW) was used. The scattering signal was detected at an angle of 20°. From each measured intensity–intensity time correlation function, a hydrodynamic radius distribution $f(R_h)$ can be obtained.[13] The relative peak area changes on $f(R_h)$ can approximately reflect the changes in the relative amounts of different scattering objects. Figure 4.2a shows the $f(R_h)$ curves obtained before (black) and after (purple) the extrusion. Only one peak is present before the extrusion. The hydrodynamic radius at the peak maximum is 25 nm (Supporting Information). The shell thickness and the core radius are estimated to be 13 and 12 nm, respectively.[15] This peak corresponds to the spherical micelles. In contrast, two peaks are present after the extrusion. One is peaked at 31 nm and narrow, and the other is centered at 275 nm and broad. According to the TEM observations (Figure 4.1b,c), these two

peaks correspond to the spherical and cylindrical micelles, respectively. Because of their entanglement and large length distribution, the scattering peak associated with the cylindrical micelles is relatively broad.

The diameter of the small pores of the membrane is smaller than that of the spherical micelles. During the extrusion process, the spherical micelles are squeezed into the nanopores by the flowing liquid. The confinement in the nanopores induces the fusion of the spherical micelles into the cylindrical ones, which are thereafter pushed out of the nanopores (Figure 4.1a).

The mixture solvent used in our experiments is thermodynamically favorable for the formation of the spherical micelles. The cylindrical micelles formed through the extrusion changed gradually into the spherical micelles. This transformation was monitored with DLS (Figure 4.2) and TEM (Figure 4.1). The hydrodynamic radius of the cylindrical micelles decreased from 300 to 70 nm within 2 d after the extrusion, while that of the spherical micelles stayed around 27 nm. The contribution of the spherical micelles to the total scattering signal increased steadily as a function of time (Figure 4.2b). TEM imaging shows the undulation in diameter along the length axis of the cylindrical micelles. The undulation evolved into pearl-necklace-like nanostructures and then into spherical micelles (Figure 4.1g). The entire transformation process was complete after about 5 d. In addition, most cylindrical micelles possess thicker spherical end caps (Figure 4.1d). In comparison, the spherical end caps are observed to be similar in diameter to the cylindrical micelles in a previous study with PS-*b*-PI copolymers,[16] where the morphological change is induced by the change in temperature and thus the solvent quality. In our experiments, the solvent quality remained constant before and after the extrusion. Further studies are required to understand the transformation process in our experiments.

4.3 Conclusion

In conclusion, nanopore extrusion-induced transition from spherical to cylindrical micelles has been demonstrated. The production of cylindrical micelles using this extrusion process is simple, and scalable. We are going to apply this preparation method to other block copolymers and develop methods for crosslinking the cylindrical micelles[17] into nanofibers during their production. We believe our method

will open enormous opportunities for the applications of copolymer nanofibers in composite materials and biotechnology.

4.4 References and Notes

(1) (a) Wang, H.; Wang, X. S.; Winnik, M. A.; Manners, I. *J. Am. Chem. Soc* 2008, *130*, 12921–12930. (b) Wang, H.; Lin, W. J.; Fritz, K. P.; Scholes, G. D.; Winnik, M. A.; Manners, I. *J. Am. Chem. Soc* 2007, *129*, 12924–12925.

(2) Yuan, J. Y.; Xu, Y. Y.; Walther, A.; Bolisetty, S.; Schumacher, M.; Schmalz, H.; Ballauff, M.; Müller, A. H. E. *Nat. Mater.* 2008, *7*, 718–722.

(3) Wang, H.; Patil, A. J.; Liu, K.; Petrov, S.; Mann, S.; Winnik, M. A.; Manners, I. *Adv. Mater.* 2009, *21*, 1805–1808.

(4) Hartgerink, J. D.; Beniash, E.; Stupp, S. I. *Science* 2001, *294*, 1684–1688.

(5) Silva, G. A.; Czeisler, C.; Niece, K. L.; Beniash, E.; Harrington, D. A.; Kessler, J. A.; Stupp, S. I. *Science* 2004, *303*, 1352–1355.

(6) Tan, J. P. K.; Kim, S. H.; Nederberg, F.; Appel, E. A.; Waymouth, R. M.; Zhang, Y.; Hedrick, J. L.; Yang, Y. Y. *Small* 2009, *5*, 1504–1507.

(7) Geng, Y.; Dalhaimer, P.; Cai, S. S.; Tsai, R.; Tewari, M.; Minko, T.; Discher, D. E. *Nat. Nanotechnol.* 2007, *2*, 249–255.

(8) (a) Won, Y.-Y.; Davis, H. T.; Bates, F. S. *Science* 1999, *283*, 960–963. (b) Wang, X. S.; Guerin, G.; Wang, H.; Wang, Y. S.; Manners, I.; Winnik, M. A. *Science* 2007, *317*, 644–647. (c) Gädt, T.; Ieong, N. S.; Cambridge, G.; Winnik, M. A.; Manners, I. *Nat. Mater.* 2009, *8*, 144–150.

(9) Cui, H. G.; Chen, Z. Y.; Zhong, S.; Wooley, K. L.; Pochan, D. J. *Science* 2007, *317*, 647–650.

(10) Zhu, J. T.; Hayward, R. C. *J. Am. Chem. Soc* 2008, *130*, 7496–7502.

(11) Baram, J.; Shirman, E.; Ben-Shitrit, N.; Ustinov, A.; Weissman, H.; Pinkas, I.; Wolf, S. G.; Rybtchinski, B. *J. Am. Chem. Soc* 2008, *130*, 14966–14967.

(12) Hadjichristidis, N.; Iatrou, H.; Pispas, S.; Pitsikalis, M. *J. Polym. Sci. Part A: Polym. Chem.* 2000, *38*, 3211–3234.

(13) Hong, L. Z.; Jin, F.; Li, J. F.; Lu, Y. J.; Wu, C. *Macromolecules* 2008, *41*, 8220–8224.

(14) Jin, F.; Wu, C. *Acta Polym. Sin.* 2005, 486–490.

(15) Tu, Y. F.; Wan, X. H.; Zhang, D.; Zhou, Q. F.; Wu, C. *J. Am. Chem. Soc.* 2000, *122*, 10201–10205.

(16) LaRue, I.; Adam, M.; Pitsikalis, M.; Hadjichristidis, N.; Rubinstein, M.; Sheiko, S. S. *Macromolecules* 2006, *39*, 309–314.

(17) Read, E. S.; Armes, S. P. *Chem. Commun.* 2007, 3021–3035.

Chapter 5

Extrusion of Spherical Micelles Made of Block Copolymer through a Small Cylindrical Pore: Mechanism of Sphere-to-Cylinder Transition and the Effect of THF Content and Extrusion Flow Rate

5.1 Introduction

Amphiphilic block copolymers in selective solvent self-assemble into colloidal nanostructures, in a similar way as small molecule surfactants.[1] There are a variety of morphologies including spheres, cylinders, vesicles, flower-like structure, toroidal structure, and the beautiful multicompartment micelles[2-9]. Under equilibrium state, the morphologies are determined by a fine balance of interfacial tension, chain stretching within the micelle core, and repulsion among the soluble shell.[2, 10, 11] When this force balance is disturbed, the aggregation morphology may transform from one into another. Because the size and shape of the block copolymer micelles can profoundly influence the further application in material science[12] and drug delivery,[13, 14] a great interest has been focused on the precise control of the micelle morphologies. The wormlike block copolymer micelles are particularly useful. They can function as templates to align inorganic nanocrystals into one-dimensional array[15] and fabricate polymer-silica[16] and polymer-metal oxide nanowires.[17] Moreover, they can be useful for sustained drug release with longer circulation time and such 1-D object can orient and stretch in a flowing stream in a manner that is ideal for flow-intensive drug delivery applications.[18] Over the last few decades, the micelle morphological transitions in solutions have been realized by changing the block copolymer composition,[2, 5, 7, 10] polymer concentration,[19] solvent composition[20] and temperature,[21, 22] or by the addition of homopolymer.[23] In contrast to these bottom-up approaches, realized by controlling thermodynamic factors, methods by controlling the kinetic factors can also lead to various morphologies. Shear rate has been proved effective to induce possible morphology transformation not only for small molecule surfactants,[24-27] but also for the polymeric surfactants.[28-31] Winnik's group[28] found the spherical hybrid micelles with quantum dots aggregated to form stable wormlike networks under rapid stirring. More recently, Moffitt and

coworkers[29, 32] produced variable flow-induced morphologies including cylinders and vesicles in a gas-liquid microfluidic reactor, where exclusively spherical morphology are found for the off-chip condition. Those morphologies should be only kinetically trapped intermediate states, but not globally equilibrated or thermodynamically favorable. In a review by Hanward and Pochan[33] summarized the popular processing approaches that provide new levels of tailorability to the structures and encapsulated contents of block copolymer assemblies in solution.

Previously, we have found a novel sphere-to-cylinder transition induced by nanopore extrusion of the block copolymer spherical micelles in the solution.[34] Here we further study the detail mechanism for such a transition, by using block copolymers with different composition, polymer micelle solution with different THF (common solvent) content and different nanopore extrusion flow rate. Interesting, when perusing the aim of continuous production of the nanofibers via nanopore extrusion, another unexpected phenomenon is found: the production of fibers via nanopore extrusion of the spherical micelles is not continuous but related to how much volume of micelle solution that have been extruded. By measuring the hydraulic pressure right before the 20 nm nanopores membrane during the extrusion process, the mechanism of nanopore extrusion induced sphere-to-cylinder transition and the question that why nanofibers cannot be continuously produced can finally be elucidated. After considering the influence of polymer adsorption in the nanopore, we further investigated the influence of THF content and the flow rate during the extrusion to the sphere-to-fiber transition as well as the nanofibers dissociation kinetics. This approach provides a convenient morphological control by further extrusion through nanopores of the spherical micelles.

5.2 Experimental Section

5.2.1 Sample preparation

Polystyrene-*b*-polyisoprene (PS-*b*-PI) diblock copolymer, $(St)_{285}$-*b*-$(Iso)_{245}$ and $(St)_{285}$-*b*-$(Iso)_{100}$ (subscripts refer the polymerization degrees of each block) was synthesized using the high-vacuum living anionic polymerization initiated by *sec*-butyllithium in THF at -78 ^{o}C for PS block and 0 ^{o}C for PI block. The synthetic details were well-documented in literature.[35, 36] The copolymer was characterized by gel permeation chromatography, a combination of static and dynamic light scattering,

and proton nuclear magnetic resonance. The copolymer is narrowly distributed with a polydispersity index of 1.06.

The micellar solutions were prepared by first dissolving the copolymer in THF and then adding dropwise different amounts of *n*-hexane under stirring with final mass concentration of 0.5 mg/mL. Each final solution was kept at 25 ^{o}C for more than one month before nanopore extrusion (ultrafiltration) to ensure the formation of stable polymeric micelles. A combination of static and dynamic laser light scattering measurements enables us to accurately characterize such formed polymeric micelles in terms of their size and structure before the ultrafiltration and the retention of polymeric micelles during the ultrafiltration.

5.2.2 Nanopore extrusion

An SGE gastight syringe and a Whatman 20-nm filter were used. The double-layer structure of the membrane was well-characterized.[37] The upper thick layer (59 μm) and the under thin layer (1 μm), respectively, contain 200- and 20-nm pores with pore number of ~ 9×10^8. On average, each small pore is covered by a large one. Such structures are confirmed by SEM images from both sides and cross-section. Micellar solution was stored in the syringe, with 20 nm nanopore filter connected. The solution after extrusion was collected into a pre-dust-free vial (typical volume of 1 mL) for further LLS measurement. The ultrafiltration experiment was performed at room temperature. The flow rate of each block copolymer micellar solution through the filter was controlled by a Harward-2000 syringe pump while the hydraulic pressure drop across the nanopore membrane for the ultrafiltration process was *in situ* measured by a high accuracy pressure sensor from ASCO.

5.2.3 Laser light scattering

A commercial LLS spectrometer (ALV/DLS/SLS-5022F) equipped with a multi-τ digital time correlator (ALV5000) and a cylindrical 22 mW He-Ne laser (λ_0 = 632 nm,Uniphase) as the light source was used. In static LLS, we can obtain the weight-average molar mass (M_w) and the *z*-average root-mean-square radius of gyration ($<R_g^2>^{1/2}$) of polymeric micelles in a dilute solution with a concentration of *C* from the angular dependence of the excess absolute scattering intensity, known as the Rayleigh ratio $R_{vv}(q)$, by

$$\frac{K(C-CMC)}{R_{vv}(q)} \approx \frac{1}{M_w}(1+\frac{1}{3}\langle R_g^2\rangle q^2)+2A_2(C-CMC) \qquad (5\text{-}1)$$

where C and CMC are the polymer and critical micelle concentrations, respectively; $K = 4\pi^2 n^2(\mathrm{d}n/\mathrm{d}C)^2/(N_A\lambda_0^4)$ and $q = (4\pi n/\lambda_0)\sin(\theta/2)$ with N_A, n, θ, and λ_0 being the Avogadro number, the solvent refractive index, the scattering angle, and the wavelength of the laser light in vacuum, respectively; and A_2 is the second virial coefficient. In dynamic LLS, the Laplace inversion of each measured intensity-intensity time correlation function $G^{(2)}(t,q)$ in the self-beating mode can lead to a line-width distribution $G(\Gamma)$. For a pure diffusive relaxation, Γ is related to the translational diffusion coefficient D, i.e., $\Gamma = Dq^2$ at $q \rightarrow 0$ and $c \rightarrow 0$, or further to the hydrodynamic radius R_h by the Stocks-Einstein equation, $R_h = k_B T/6\pi\eta D$, where k_B, T and η are the Boltzmann constant, the absolute temperature and the solvent viscosity, respectively. Note that for block copolymer micelles in solution with a very low CMC, C - $CMC \approx C$ and the time-average scattering intensity $\langle I\rangle$ is dominated by large polymeric micelles. The retention of polymeric micelles by small pores can be calculated from the micelle concentrations (C_0 and C) before and after the ultrafiltration, which are related to $\langle I\rangle$, namely, $(C_0 - C)/C_0 \approx (\langle I_0\rangle - \langle I\rangle)/\langle I_0\rangle$.

5.2.4 TEM imaging

The Transmission electron microscopy (TEM) imaging was performed on an FEI CM 120 microscpe operated at 120 kV. 10 μL of the polymer solutions was placed onto carbon-coated copper grids, followed by drying in ambient air with a hair dryer. The length distribution of the generated fibers was measured with Adobe Acrobat from many TEM images.

5.3 Results and Discussion

Table 5.1 shows the four diblock copolymers PS-*b*-PI prepared by anonic polymerization for study of the nanopore extrusion of the spherical micelles. When dissolving in the *n*-hexane, a selective good solvent for polyisoprene block, the block copolymer would self-assemble into spherical micelles, except for the last one. After been prepared for more than one month, the spherical micelles were used for nanopore extrusion. It has been found previously that spherical micelles in *n*-hexane

from PS_{180}-*b*-PI_{500} can pass through the 20 nm nanopores, with different retention at different flow rate while that from PS_{170}-*b*-PI_{140} are fully blocked by the nanopore [36] And similar to PS_{170}-*b*-PI_{140}, spherical micelles prepared in pure *n*-hexane from PS_{285}-*b*-PI_{245}, which has a high PS fraction with even longer chain length, could not pass through the 20 nm nanopores and further extrusion would rupture the nanopore membranes. Another PS-*b*-PI copolymer with even higher PS fraction, PS_{285}-*b*-PI_{100} self-assembles into cylindrical micelles, instead of spherical morphology in the pure *n*-hexane and hence will not be further discussed.

Table 5.1. Polystyrene weight fraction, average hydrodynamic radius, the ratio of average radius of gyration over hydrodynamic radius and diameters from TEM imaging of the block copolymer micelles in *n*-hexane for block copolymers with different block composition used for nanopore extrusion.

Diblock Copolymer	PS fraction / %	$\langle R_h \rangle$ / nm	$\langle R_g \rangle / \langle R_h \rangle$	Diameter from TEM / nm	Notes
PS_{180}-*b*-PI_{500}	35	28	0.71	19	Pass
PS_{170}-*b*-PI_{140}	65	26	0.56	30	Block
PS_{285}-*b*-PI_{245}	64	30	0.60	42	Block
PS_{285}-*b*-PI_{100}	81	--	--	--	--

Note: for the composition of PS_{285}-*b*-PI_{100}, the block copolymer self-assembles into cylindrical micelles in *n*-hexane, instead of spherical micelles, so the corresponding characteristic parameters are not given.

When the spherical micelles from PS_{285}-*b*-PI_{245} in *n*-hexane were swollen with common solvent THF, extrusion of those swollen spherical micelles resulted in a similar sphere-to-cylinder transition. So we would like to investigate the mechanism for such a commonly exist sphere-to-cylinder transition, by using the micelles from block copolymer PS_{285}-*b*-PI_{245} and their dependence on the swelling (that is the THF content) of the spherical micelles and extrusion flow rate.

First, the spherical micelles in solution with different THF content from 3 to 27% was carefully studied before used for further nanopore extrusion by using a combination of LLS and TEM. Without THF addition, the block copolymer micelles

take spherical morphology with $\langle R_h \rangle$ of 30 nm and $\langle R_g \rangle$ of 18 nm. Figure 5.1 shows that both $\langle R_h \rangle$ and $\langle R_g \rangle$ of the copolymer micelles keep almost constant with the THF content below 13 vol%, then increase with further addition of THF, indicating the gradual swelling of the spherical micelles, and finally abruptly decrease at THF content of ~ 25%, revealing the dissolution of each copolymer micelles into individual chains. Similar tendency has been reported for PS_{170}-*b*-PI_{140} in *n*-hexane/THF mixture solvents.[38] The micelles morphologies are further confirmed with TEM images, with all samples prepared in fast drying condition. As shown in Figure 5.2, only spherical micelle morphology was observed. And the diameters for the spheres in dry state are close to 41 nm.

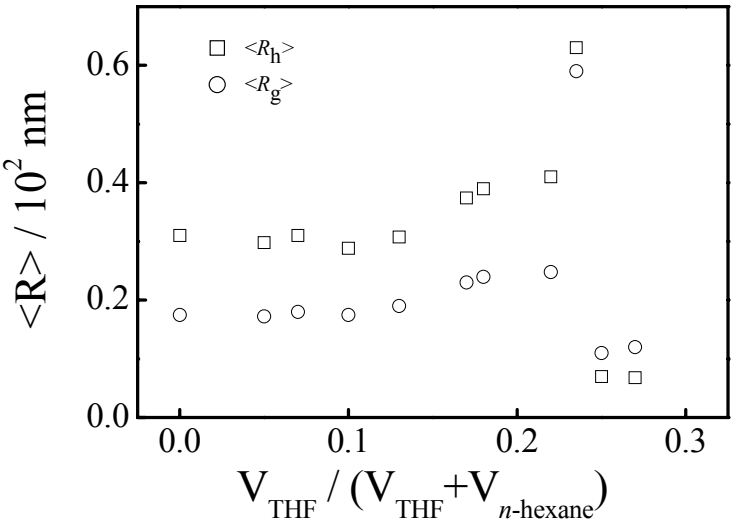

Figure 5.1. THF content dependence of average hydrodynamic radius $\langle R_h \rangle$ and radius of gyration $\langle R_g \rangle$ of diblock copolymer micelles in a mixture of THF and *n*-hexane with polymer concentration of 0.5 mg/mL.

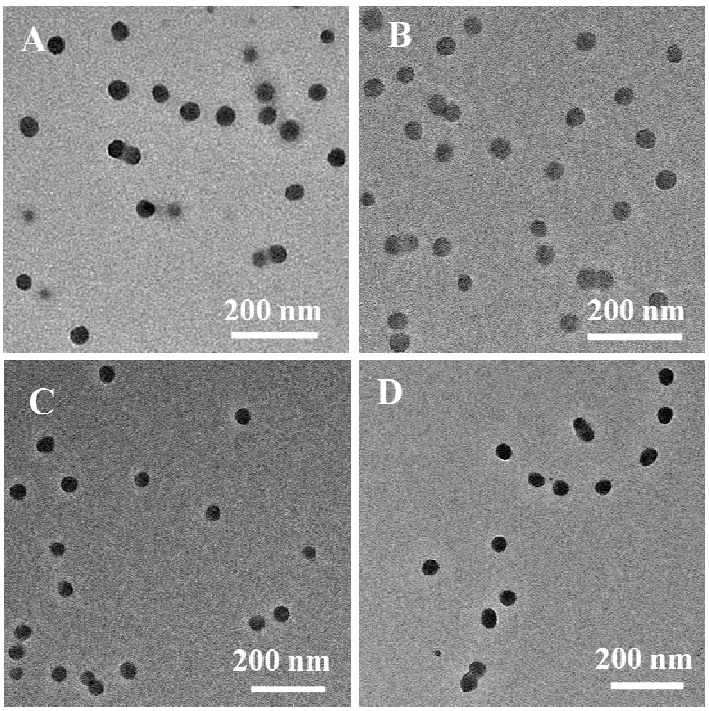

Figure 5.2. TEM images for block copolymer PS_{285}-*b*-PI_{245} micelles in a mixture of THF and *n*-hexane solution with different THF content prepared in fast drying condition: (A) 0 vol%, average diameter: 42.9 ± 3.8 nm; (B) 5 vol%, 40.3 ± 4.3 nm; (C) 10 vol%, 41.7 ± 3.7 nm; and (D) 13 vol%, 45.4 ± 3.3 nm.

5.3.1 Sphere-to-cylinder transition mechanism

When using these spherical micelles for nanopore extrusion, we found micelles in *n*-hexane/THF with THF content below 10% could still be fully blocked by the 20 nm nanopore membrane, and further extrusion of the micellar solutions would finally result in the rupture of membrane. This indicates that the micelles in solution with THF content less than 10% are still too hard to be deformed or dissociated. So we started with micelles in *n*-hexane/THF with 10 vol% THF for the extrusion experiment. Consistent with our observation of nanopore extrusion of PS_{170}-*b*-PI_{140} micelles in *n*-hexane/THF solution,[34] large amount of nanofibers with width close the sphere diameter and length of few micrometers were found in the solution after nanopore extrusion. The scattering intensity of the solution was measured at scattering angle of 20^{o}, and it decayed slowly with time, indicating the nanofibers dissociation after extrusion since wormlike morphology is not thermodynamic stable. Starting with the idea to vastly produce the 1-D nanofibers in such a simple and fast way, we found another unexpected observation: that the generation of nanofibers

from nanopore extrusion was not continuous, but related with the volume of filtration solution through the nanopore membrane. Figure 5.3 shows both the hydrodynamic radius distribution and representative TEM images for the micellar solution before and after extrusion at flow rate of 20 mL/hr. At the filtration volume of 1-6 mL, many nanofibers were observed with a large hydrodynamic radius peak $\langle R_h \rangle$ at ~110 nm. But at filtration volume of 7 mL or more, only sticky spheres with $\langle R_h \rangle$ of 33 nm were observed, quite similar to the spherical micelles prior to extrusion.

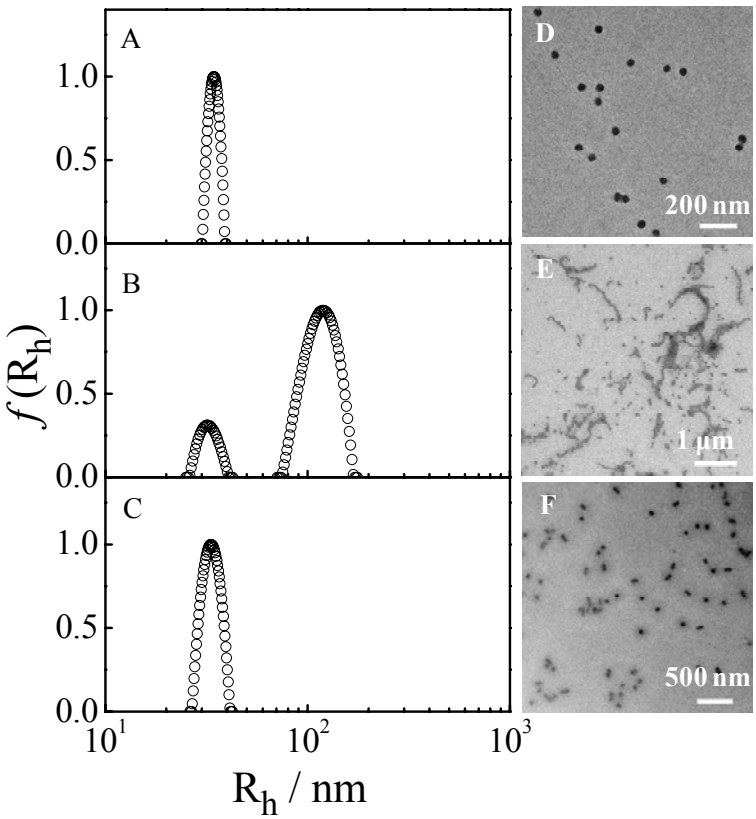

Figure 5.3. Hydrodynamic radius distribution and representative TEM images of micellar solution before nanopore extrusion (A, D); immediately after nanopore extrusion at filtration volume of 2 mL (B, E); and immediately after nanopore extrusion at filtration volume of 7 mL (C, F) for micellar solutions with 10% THF content at flow rate of 20 mL/hr. The polymer mass concentration in the solution is 0.5 mg/mL.

To exclude the possibility of nanopores rupture, the filter membrane after micelle extrusion was recycled, by washing with vast THF solvent also at 20 mL/hr and dried at 50 ^{o}C overnight for next extrusion cycle. Two parameters are considered for the sphere-to-fiber transition process: average hydrodynamic radius $\langle R_h \rangle$ and $\langle I \rangle_0 / \langle I \rangle_\infty$ value for the solution after extrusion. $\langle I \rangle_0$ and $\langle I \rangle_\infty$ stand for the scattering

intensity of solutions immediately (t = 0) after extrusion and extremely long time (t = ∞) after extrusion, etc., after reaching the thermodynamically stable spherical morphology, respectively. Since the generated nanofibers dissociate in the solution, the measured $\langle I \rangle$ decays and it is difficult for reliable sampling of the DLS autocorrelation function within limited time if the dissociate kinetics is fast. So the obtained $\langle R_h \rangle$ might be inaccurate. Since, $\langle I \rangle \sim KCM$, then $\langle I \rangle_0 / \langle I \rangle_\infty \sim M_{fiber}/M_{sphere}$, we can use this ratio as a parameter of sphere-to-cylinder transition extent. Figure 5.4A shows the filtration volume dependence of sphere-to-fiber transition extent with the same 20 nm nanopore filter membrane for micellar solution with 10% THF content. The same filter membrane was recycled for two more extrusion cycles. For the earlier 3-6 mL, nanofibers were generated for all three trials with $\langle I \rangle_0 / \langle I \rangle_\infty$ about 4-8. But after that, the $\langle I \rangle_0 / \langle I \rangle_\infty$ value approached to one unit, indicating the absence of nanofibers in the solution after nanopore extrusion. We would like to define the filtration volume during which $\langle I \rangle_0 / \langle I \rangle_\infty$ value is large than one to be "active" filtration volume. Such "active" filtration volume varies a little for different extrusion cycles. Similar investigations for micelles with another THF content 18% was also carried out, with sphere-to-cylinder transition extent, $\langle I \rangle_0 / \langle I \rangle_\infty$, about 10-20 before dropping off to one unit. The retention ratio decreases to zero from the first milliliter to the last milliliter. Since the recycled filter membrane shares similar results as the new one for the sphere-to-cylinder transition, it is unlikely for the rupture of the nanopore membrane during the extrusion process. To find out the reason why the production of nanofibers induced by nanopore extrusion is non-continuous, and its relation to filtration volume, we carefully measured the hydraulic pressure drop across the nanopore membrane for the micelle extrusion process. The pressure sensor is connected with a multimeter for voltage readout, where the relationship between the pressure and voltage has been established in advance.[39] As shown in Figure 5.4B, the measured hydraulic pressure before nanopore membrane during the nanopore extrusion, first increases, probably due to accumulation of micelles at the pore entrance (the evidence is that there are micelle retention by the nanopore at earlier filtration volume), but then decreases to a extremely low value, which is even much smaller than the hydraulic pressure for the pure solvent mixture flow through the same filter membrane at the same flow rate, and finally levels off. We further investigated the flow rate dependence of measured

hydraulic pressure for THF/*n*-hexane mixture (10% THF content) through the same filter membrane before and after the micelle extrusion (after pressure drops to the lowest value), as shown in Figure 5.5. It is clear that the filter membrane that after micelle extrusion has completely different properties for liquid transport compared with that before micelle extrusion in each cycle. For example, the pressure at 100 mL/hr for the pristine filter before used for micelle extrusion was 41 kPa, while for the same filter membrane after micelle extrusion, the value dropped to ~ 0.2 kPa. After precluding the possibility of filter membrane rupture during extrusion, we believe that the much lower hydraulic pressure is a result of lubrication effect induced by the polymer brushes adsorbed on the nanopore surface. We have discussed the enhancement of fluid flow through nanopores induced by polymer brushes adsorbed on the nanopore wall previously and suggested that low density polymer brushes on the surface increase the fluidic resistance, while dense polymer brushes significantly decrease the fluidic resistance.[40] When using a 20 nm filter membrane which has been previously saturated adsorbed with PS-*b*-PI polymer in THF solution for further nanopore extrusion of the spherical micelles, just as expected, no nanofibers were observed and the measured hydraulic pressure across the 20 nm filter membrane was also much lower than that for a new filter membrane with the same liquid. The lubrication effect for liquid transport induced by a thin film of polymer brushes[41] or small molecule surfactants[42, 43] has been much investigated before, despite a lack of definite physical explanation.

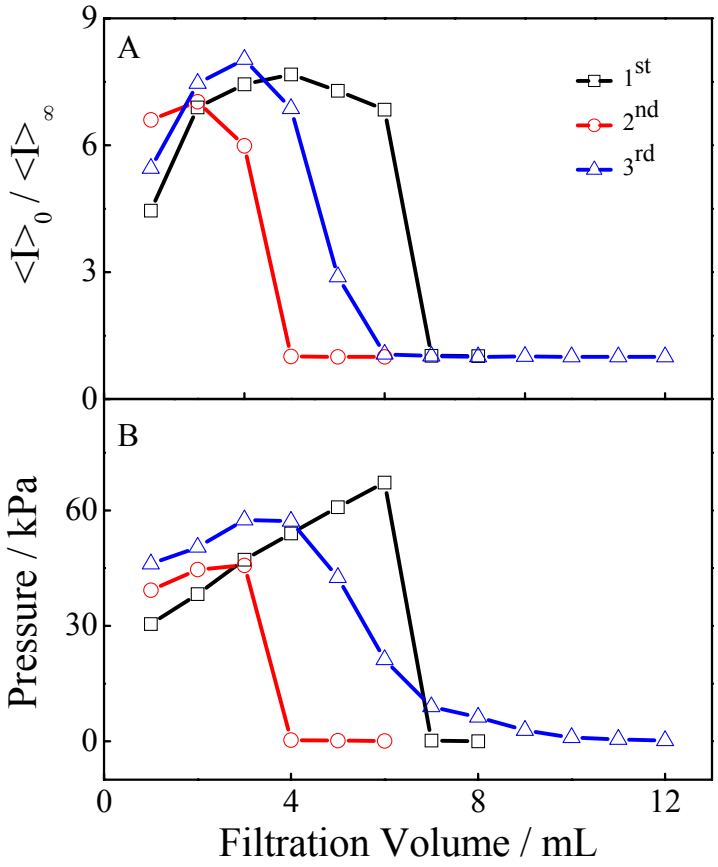

Figure 5.4. Filtration volume dependence of A) sphere-to-fiber transition extent, $\langle I\rangle_0/\langle I\rangle_\infty$ value and B) measured hydraulic pressure drop across the filter membrane during the micelles extrusion from the nanopores with flow rate, 20 mL/hr, THF content, 10% and block copolymer mass concentration, 0.5 mg/mL. The same filter membrane has been recycled by rinsing with vast THF solvent and drying at 50 ^{o}C overnight and then used for next cycle of extrusion.

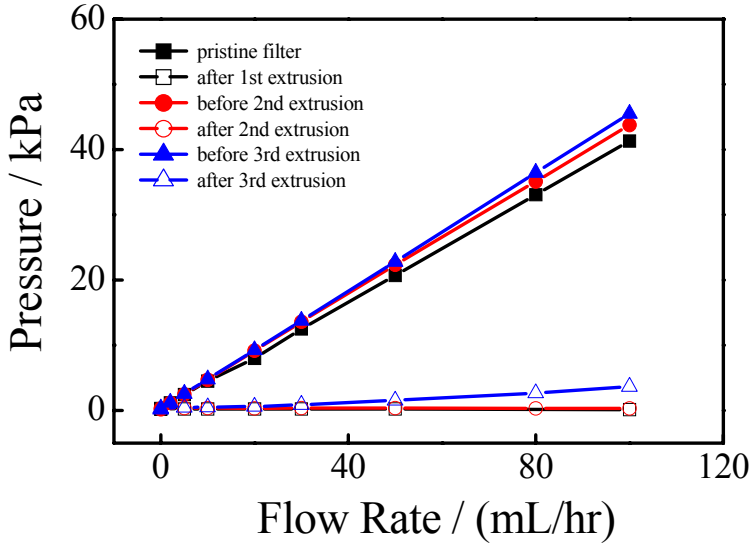

Figure 5.5. Measured hydraulic pressure curves with flow rate for THF/*n*-hexane (10% THF content) transport through the same nanopore membrane before and after micelles extrusion (after the measured hydraulic pressure drops to the lowest value). The same filter membrane has been recycled and used for three cycle's extrusion.

In case of the nanopore extrusion of spherical micelles, the interaction inside the nanopore changes from the liquid with pore wall surface to the spherical micelles corona with nanopore wall surface. When the nanopore wall is bare, and a large spherical micelle enters into the pore, the micelle should feel great resistance for further movement. One of the reasons is that since their size is larger than the pore, the micelles have to be deformed and the consequent severe normal compression by the surrounding pore wall can bring lateral friction forces. Another reason is that the slight affinity interaction (PI block has stronger affinity than the PS block to the pore wall) between the polymer segments and the pore wall can further retard the smooth travelling of the micelles in the pore. However, when polymer adsorption starts and polymer brushes physisorb on the wall, the interaction between micelles corona and pore wall bearing polymer brushes has to be reconsidered carefully. Previous studies showed normal forces between surfaces bearing either adsorbed or grafted polymer chains in good solvent are monotonically repulsive with the polymer surface coverage even at very long separation.[44, 45] Such repulsion forces, originated from excluded volume effect, allow weak mutual interpenetration between brushes, so that the interface remains fluid, with high relaxation rate, and presents little resistance to the shearing motion, finally a striking reduction of frictional force when two surfaces slide against each other.[46] The efficiency of polymer brushes in reducing frictional force is a function of compression strength, sliding velocity as well as solvent quality.[47] Dense polymer brushes and high compression facilitate the lubrication. In our case when polymer brushes form on the pore wall, the spherical micelles enter into the pore, and are strongly repulsed and compressed by the surrounding pore wall bearing polymer brushes. Similar to the sliding of surfaces bearing polymer brushes, the spheres in the small channel stand very weak resistance when they travel in the pores, either by sliding or rolling. Such lubrication effect by polymer brushes terminates the accumulation of spheres and micelles coalescence at the pore entrance. To validating our assumption for the polymer brushes lubrication during the spherical micelles extrusion, we need to prove the presence of polymer brush layer on the

surface of the nanopore wall. However, it is rather difficult, if not impossible, to investigate the polymer brush layer adsorbed on the wall inside the nanopore. Instead, we characterized the surface of the aluminum oxide nanopore membrane surface before and after nanopore extrusion with the attenuated total reflectance infrared spectroscopy (ATR-IR) and the Time of Flight Secondary Ion Mass Spectrometry (TOF-SIMS). The filter membrane that after nanopore extrusion was washed with large volume of THF to remove any possible unbound free polymer chains before been dried and subjected to surface characterization. The corresponding data was provided in the appendix part of the thesis (Figure 5.S1and S2).

Here we finally are able to propose a model to elucidate the speculation for the nanopore extrusion induced sphere-to-cylinder transition and reason that why the transition is non-continuous, but related with polymer adsorption on the surface of nanopore wall. As the extrusion starts, the solvent liquid would flow from the 200nm side to the 20nm side, bringing along the spherical micelles in the solution. Since the diameter of the spherical micelles is larger than the 20 nm, they cannot automatically enter into pores, but stay at the entrance of the smaller channel. As more and more spheres accumulate at the funnel location, which block the areas for the liquid flow, the real liquid velocity at the funnel location becomes very large. Spheres may either enter into the pores separately driven by the higher velocity flow before they are fused together, or fuse with each other at the pore entrance if they are soft enough, before they enter into the pore. In the former case, only spheres similar to that before extrusion should be found in the solution after extrusion while in the latter case, long wormlike fibers can be observed in the solution after extrusion. Here we would like to introduce two time scale to explain the criteria for the formation of wormlike micelles as presented in Scheme 5.1. Say one sphere is already located at the entrance of the 20 nm channel, we define the time for this sphere to leave the location and travel through the 20 nm channel under the liquid flow to be t_1, and the time for the next sphere in the solution to arrive at the entrance to be t_2. If $t_1 > t_2$, accumulation of the spheres at the 20 nm pore entrance would happen. Given that the spherical micelles are soft enough, intermicellar fusion may happen before they enter into the pore. On the other hand, if $t_1 < t_2$, namely, the sphere can leave the entrance and enter into the funnel before the next sphere arrives, spherical micelles then can pass through the 20nm channel by a one-by-one fashion. For a micelle extrusion process with fixed flow rate, t_2 should be constant, which only depending on the

micelle number concentration and flow rate, while t_1 is strongly dependent on the efficiency of friction reduction by the polymer brushes on the wall. At the very beginning, the first sphere arrives at the entrance of the 20 nm channel, because of the large size, the spheres could not enter into the smaller pore, so t_1 is extremely long. But as the accumulation goes on, the effective liquid flow velocity becomes much larger and the sphere is driven by increasing hydrodynamic force. If the size discrepancy is not large or if the sphere can be easily deformed before intermicelles fusion happens, micelles can still pass through the nanopore separately, with shorter time t_1. Because of the continuous adsorption of polymer, especially the polyisoprene block on the pore surface, the polymer brushes lubrication effect may take effect, consequently with much less t_1. With $t_1 < t_2$, spherical micelles can pass through the nanopores without a stop at the pore entrance.

As for the recycling of the filter membranes, extrusion of spherical micelles could still induce the sphere-to-cylinder transition. We believe that the thin polymer brushes layer bounded on the nanopore wall would undergo micro-phase separation during drying treatment, since T_g of PI block is much lower than the annealing temperature,[48, 49] and the re-exposure of the aluminum oxide surface to the solution can hinder the lubrication effect caused by the polymer brushes.

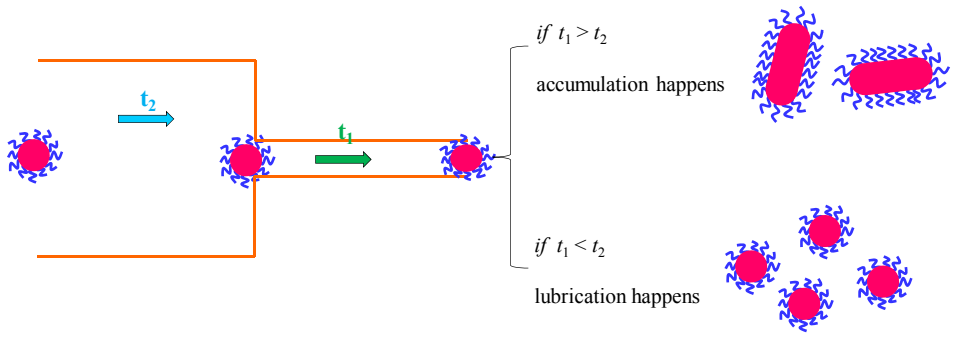

Scheme 5.1. Schematic showing the nanopore extrusion induced sphere-to-fiber transition mechanism with proper micelle softness.

On the basis of above analysis, several alternative mechanisms for the morphology transformation after nanopore extruded can be ruled out. The first is the common shear-induced structure formation.[24, 25] Colloidal particles can aligned into rod-like micelles in extensional flow, as long as the extension rate is higher than the critical rate γ_c, estimated by $1/T_D \sim k_BT/(\eta a^3)$, where k_B, T, η and a denote the Boltzman constant, absolute temperature, solution viscosity and particle size.[50] And

further increase in shear rate activates shear-induced particle breakup, which competes with the shear-induced coalescence process. To eliminate this possible mechanism, we first assume the failure of continuous wormlike micelles generation is the consequence of the too high shear rate during extrusion. Because of the accumulation of spheres at the pore entrance, the real shear rate inside the 20 nm could be much higher than the initial value 4×10^5 s^{-1} at flow rate of 20 mL/hr. So when the nanofibers could not be produced at filtration volume of 8 mL, for example, we slowed down the extrusion flow rate so that the real shear rate could be possibly relocated in the "active" range. However, no matter how slow of flow rate we applied, nanofibers could not be observed any more. Such contradictory verifies that our previous assumption is not correct.

Another mechanism that solvent composition might be changed after aluminum oxide nanopore ultrafiltration has been proved not correct. We carried out the ultrafiltration of pure solvent mixture at different flow rate in the absence of polymer. No evident chemical composition difference could be found (Figure 5.S3), indicating the adsorption of solvent molecules on the pore surface is limited, if exists. The influence of gas bubbles trapped inside the nanopore membrane was also considered. After nanofibers could not be produced, gas bubbles were introduced by a "T" structure into the micellar solution with various gas/solution ratios. No differences were found from the solution after extrusion. Finally, reversal nanopore extrusion of micellar solution, with extrusion flow from the 20 nm pores side to the 200 nm pores side were conducted (Figure 5.S4). Just as expected, no nanofibers (occasionally few nanofibers) were found in the solution after extrusion. This result ensures the importance of the funnel structure for the accumulation of spheres. However, accumulation of the spheres at the pore entrance is not the sufficient condition for the formation of wormlike micelles. We have discussed that spherical micelles from PS_{170}-*b*-PI_{140} and PS_{285}-b-PI_{245} in *n*-hexane are almost blocked, and further extrusion of those spheres would not result a sphere-to-cylinder transition, but the rapture of the 20 nm nanopore membranes. That's to say, the softness of the spherical micelles are also important for the transition. It should be sufficiently soft for intermicelle fusion occurred in the nannopore under external compression, but sufficiently hard so that the micelles won't be disintegrated into unimers by the external hydrodynamic force. And such micelle softness can be carefully tuned by the incorporation of good solvent THF into the micelle solution.

5.3.2 Effect of THF content and extrusion flow rate

Figure 5.6 shows the representative TEM images of cylindrical micelles produced immediately after nanopore extrusion at flow rate of 20 mL/hr with different THF content. In Figure 5.6A (10 vol%) and 6D (22 vol%), short cylindrical micelles with length from 100 nm to few micron as well as many spherical micelles are found while in Figure 5.6B (13 vol%) and 6C (17 vol%), many more long cylindrical micelles and only few spherical micelles are observed. The influence of THF content of the spherical micelles solution to the sphere-to-cylinder transition can be understood in terms of the above argument of the transition mechanism. With lower THF content, both the intercoronal repulsion and core density can be very high. Although these spherical micelles can be blocked by the small pore with $t_1 > t_2$, they are still too hard to be deformed to enter into the nanopores under high hydrodynamic force and the activation energy for micelle coalescence, E_{a1} is too high to be overcome by extrusion compression, leading to the rapture of the nanopore membrane in the end. When further increasing THF content, these spherical micelles are swollen, with continuous increase of the estimated micelle core $<R>_{core}$,[38] contributing to a significant decrease in E_{a1}. In this case, soft spherical micelles can be squeezed into the nanopores. Due to such an intermediate value of E_{a1}, sufficiently low for the compression induced micelle fusion to be activated but sufficiently high to significantly inhibit the reverse fission, a large number of high-energy cylindrical micelles will be kinetically trapped, as indicated in Figure 6B and 6C for THF content of 13 vol% and 17 vol%, respectively. The insets shown in Figure 6 indicate that the obtained cylindrical micelles with 10 vol% THF has undulated structures while those with 13 vol% and 17 vol% have smooth surface. On the other hand, further increase of THF content can decrease E_{a1} too much, making the reverse micelles fission process also significant. So for THF content of 22%, only some short cylinders are found immediately after extrusion.

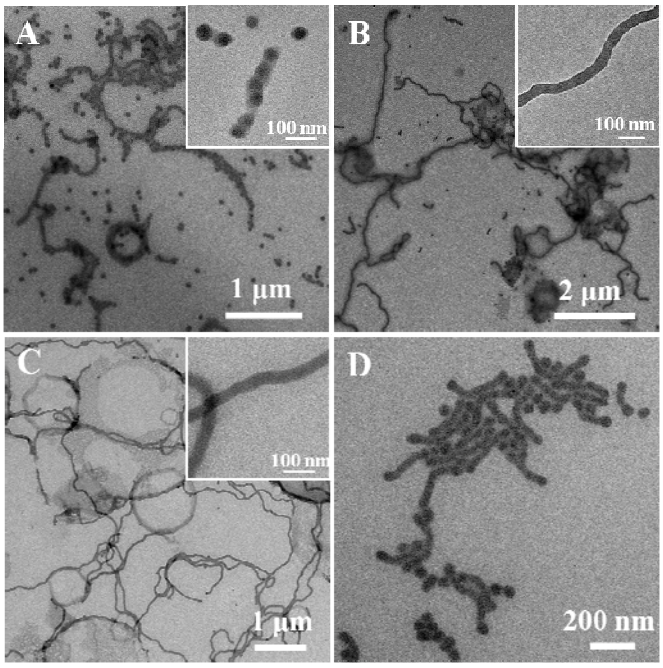

Figure 5.6. TEM images for the cylindrical micelles immediately after nanopore extrusion at fixed flow rate of 20 mL/hr with different THF content. A) 10 vol%; B) 13 vol%; C) 17 vol%; D) 22 vol%.

We further investigate the effect of different extrusion flow rate on the sphere-to-cylinder transition, using the same nanopore membrane within the filtration volume during which cylindrical micelles can be effectively produced. The extrusion process started with lower flow rate, 5 mL/hr and ended with 100 mL/hr with total filtration volume of 5 mL. The sphere-to-cylinder transition extent, $\langle I\rangle_0/\langle I\rangle_\infty$ value, and the average hydrodynamic radius, $\langle R_h\rangle_0$ immediately after extrusion with different flow rate are presented in Figure 5.7A and 7B, respectively. The sphere-to-cylinder transition reaches its highest extent ~ 50 for micelles with THF content of 13 vol% while the average hydrodynamic radius reaches the highest value ~ 170 nm with 17 vol%. We also find both $\langle I\rangle_0/\langle I\rangle_\infty$ and $\langle R_h\rangle_0$ increase slightly first and then decreases slightly with increasing flow rate. Such a tendency could be understood from the aspect of the sphere-to-cylinder transition mechanism. The effect of flow rate always have two sides: with constant spherical micelles number concentration, lower flow rate benefits the accumulation of spheres at the pore entrance, but the weak compression might not be enough to overcome the micelle coalescence activation energy; on the other hand, higher flow rate brings strong compression, but the strong hydrodynamic force doesn't benefit the spheres accumulation at the pore entrance. Thus an intermediate flow rate that balances the

spheres accumulation and compression leads to the highest sphere-to-cylinder transition extent. TEM images show there is no big difference for the wormlike micelles produced at different flow rate.

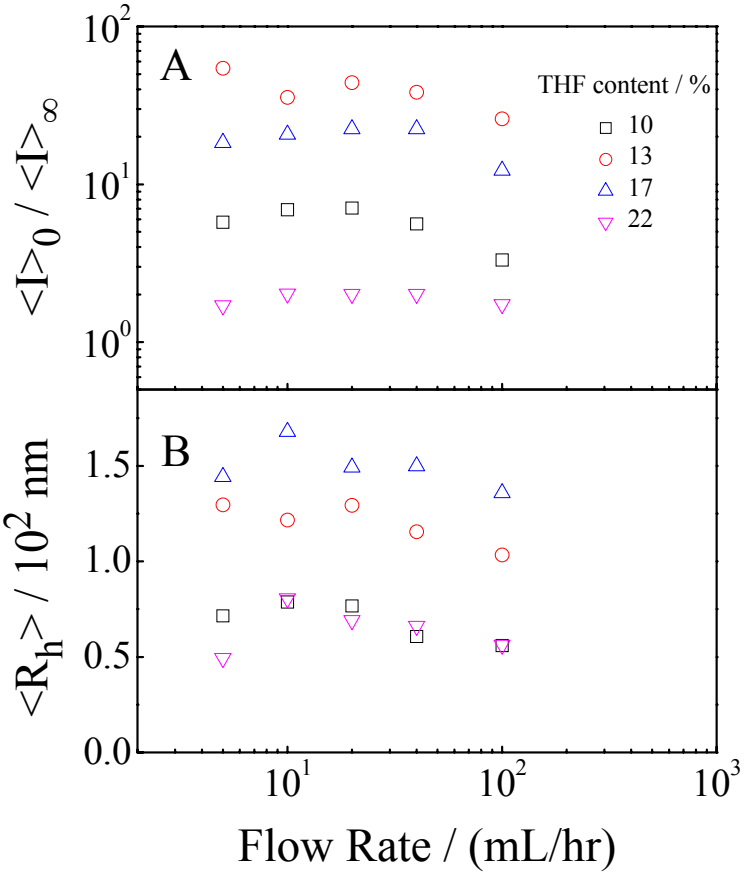

Figure 5.7. A) Sphere-to-cylinder transition extent, $\langle I\rangle_0/\langle I\rangle_\infty$ value, and B) average hydrodynamic radius, $\langle R_h\rangle_0$ immediately after extrusion for micelles with different THF content. The extrusion experiments started at 5 mL/hr, and ended with 100 mL/hr, with total filtration volume of 5 mL within the same filter membrane.

5.3.3 Nanofibers dissociation kinetics

Since the generated cylindrical micelles are not globally favored, but only kinetically trapped high-energy metastable state, dissociation starts as soon as they leave the nanochannel confinement. Such a cylinder-to-sphere reversal transition can last from minutes to weeks, depending on different solution conditions. Since the micelle morphologies from the normal TEM images could be largely influenced by the methods and technique for the TEM samples preparation on the copper grid,[38] we resort to the measured scattering intensity decay of the micelles solution to study the relaxation kinetics of the cylinder-to-sphere transition in the solution. Figure 5.8

describes the scattering intensity decays after extrusion with different THF content and flow rate. Note that the scattering intensity is proportional to the square of the molar mass of a scattering subject. Therefore, LLS is very sensitive to long cylindrical micelles and the decay of $\langle I \rangle$ indicates the breaking down of cylindrical micelles into shorter ones. For THF content of 17%, the cylinder-to-sphere transition processes last for one week before all the cylinders return to spherical micelles. We found that all decay traces in Figure 5.8 can be fit reasonably well with biexponential functions based on nonlinear least squares:

$$\langle I \rangle = A \exp(-t / \tau_1) + B \exp(-t / \tau_2) \tag{5-2}$$

where A and B are fractional contributions of the fast and slow decay times from the fit, τ_1 and τ_2 , which are probably not physically meaningful, although they characterize the distribution of decay times in the collected samples. Mean decay times for each fit were further calculated using:

$$\bar{\tau} = \frac{A}{A+B}\tau_1 + \frac{B}{A+B}\tau_2 \tag{5-3}$$

Figure 5.9 shows the calculated mean relaxation time for the cylinder-to-sphere transition is dependent on THF content, but not extrusion flow rate. It is known that the rate of the dissociation is determined by the energy barrier for the cylinder-to-sphere phase transition. And such activation energy, as discussed before, is only dependent on block copolymer intermicellar and intramicellar chain dynamics, which can be strongly tuned by the THF content in the solution.

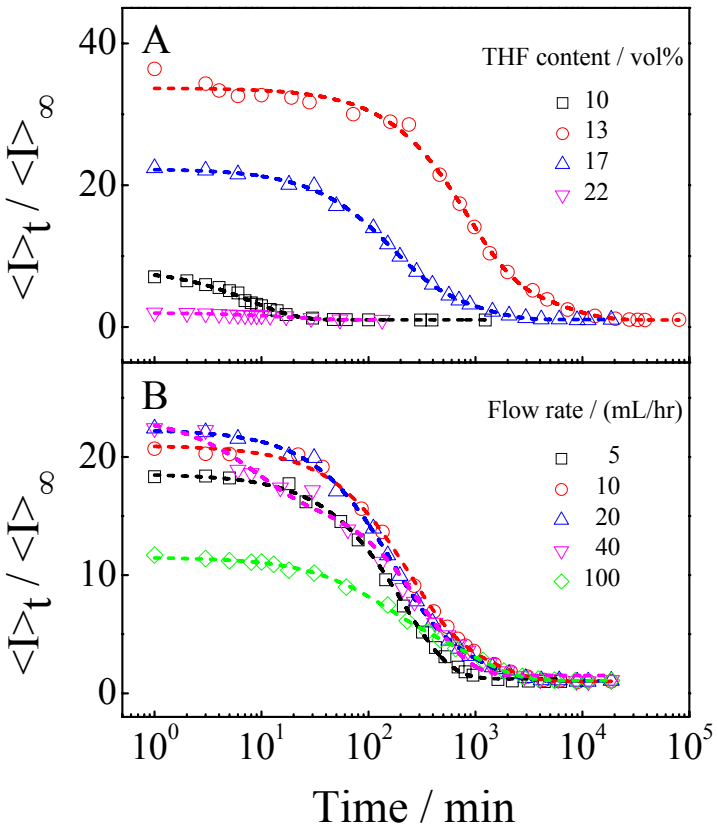

Figure 5.8. Time dependence of average scattering intensity ratio ($\langle I\rangle_t/\langle I\rangle_\infty$) of the cylinder-to-sphere transition A) for different THF content at the flow rate of 20 mL/hr and B) at different flow rate for micelle solution with THF content of 17 vol%. The dash lines are bi-exponential fitting for the data.

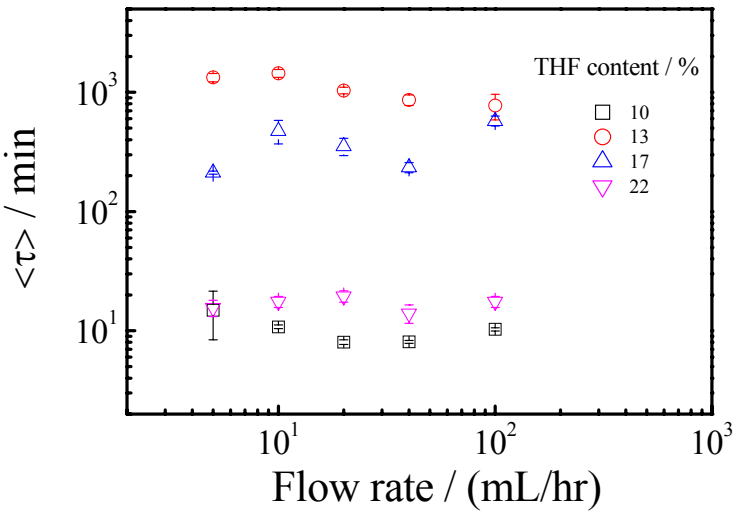

Figure 5.9. Flow rate and THF content dependence of the cylinder-to-sphere transition kinetics after nanopore extrusion.

5.4 Conclusion

We have demonstrated that the spherical micelles can be transferred to wormlike micelles after extrusion through 20 nm nanopores. The mechanism for such transition does not directly relate with shear rate, or the nanoconfinement, but the accumulation of soft spherical micelles at the entrance of the 20 nm pores and further intermicellar fusion. The size of the spherical micelles in the solution should be larger than that of the nanopore diameter so that they can be stuck at the pore entrance for further sphere accumulation. Another important parameter for further production of wormlike is the spherical micelles softness: soft enough so that the intermicellar fusion can happen before they each enter into the pores and hard enough so that the spheres won't be disintegrated under shear flow. Such intermediate softness is carefully tuned by THF content in the *n*-hexane/THF mixture solvent. We further found the formation of the wormlike micelles is not continuous, but also related to the polymer adsorption on the pore surface. To make the production of nanofibers from nanopore extrusion continuous, proper nanopore wall surface modification is needed to depress the adsorption of polymer on the wall. We further study effect of the THF content of the micelle solution and nanopore extrusion flow rate to the sphere-to-cylinder transition. Besides the cooperative information for the nanofiber dissociation kinetics from the LLS measurement, further investigations of nanofibers dissociation mechanism are still needed. In short, this approach provides a convenient micelle morphological control by further extrusion through nanopores of the spherical micelles and opens up new opportunities for processing control of functional colloidal nanostructures for the applications of block copolymer hybrid cylindrical micelles in nanotechnology and medicine.

5.4 References and Notes

(1) Riess, G., *Prog. Polym. Sci.* **2003,** 28, 1107-1170.

(2) Zhang, L.; Eisenberg, A., *Science* **1995,** 268, 1728-1731.

(3) Won, Y. Y.; Davis, H. T.; Bates, F. S., *Science* **1999,** 283, 960-963.

(4) Discher, B. M., *Science* **1999,** 284, 1143-1146.

(5) Jain, S.; Bates, F. S., *Science* **2003,** 300, 460-464.

(6) Pochan, D. J.; Chen, Z.; Cui, H.; Hales, K.; Qi, K.; Wooley, K. L., *Science* **2004,** 306, 94-97.

(7) Zhulina, E. B.; Adam, M.; LaRue, I.; Sheiko, S. S.; Rubinstein, M., *Macromolecules* **2005,** 38, 5330-5351.

(8) Moughton, A. O.; Hillmyer, M. A.; Lodge, T. P., *Macromolecules* **2012,** 45, 2-19.

(9) Groschel, A. H.; Schacher, F. H.; Schmalz, H.; Borisov, O. V.; Zhulina, E. B.; Walther, A.; Muller, A. H. E., *Nat. Commun.* **2012,** 3, 710.

(10) Zhang, L.; Eisenberg, A., *J. Am. Chem. Sci.* **1996**, 3168-3181.

(11) Zhulina, E. B.; Borisov, O. V., *Macromolecules* **2012,** 45, 4429-4440.

(12) Stewart, S.; Liu, G., *Angew. Chem. Int. Ed.* **2000,** 6, 340-344.

(13) Tan, J. P. K.; Kim, S. H.; Nederberg, F.; Appel, E. a.; Waymouth, R. M.; Zhang, Y.; Hedrick, J. L.; Yang, Y. Y., *Small* **2009,** 5, 1504-1507.

(14) Geng, Y.; Dalhaimer, P.; Cai, S.; Tsai, R.; Tewari, M.; Minko, T.; Discher, D. E., *Nat. Nanotechnol.* **2007,** 2, 249-255.

(15) Wang, H.; Wang, X. S.; Winnik, M. A.; Manners, I., *J. Am. Chem. Sci.* **2008,** 130, 12921-12930.

(16) Richman, E. K.; Brezesinski, T.; Tolbert, S. H., *Nat. Mater.* **2008,** 7, 712-717.

(17) Wang, H.; Patil, A. J.; Liu, K.; Petrov, S.; Mann, S.; Winnik, M. A.; Manners, I., *Adv. Mater.* **2009,** 21, 1805-1808.

(18) Kim, Y.; Dalhaimer, P.; Christian, D. A.; Discher, D. E., *Nanotechnology* **2005,** 16, S484-S491.

(19) Zhang, L.; Eisenberg, A., *Macromolecules* **1999**, 2239-2249.

(20) Bang, J.; Jain, S.; Li, Z.; Lodge, T. P.; Pedersen, J. S.; Kesselman, E.; Talmon, Y., *Macromolecules* **2006,** 39, 1199-1208.

(21) LaRue, I.; Adam, M.; Pitsikalis, M.; Hadjichristidis, N.; Rubinstein, M.; Sheiko, S. S., *Macromolecules* **2006,** 39, 309-314.

(22) Bhargava, P.; Tu, Y.; Zheng, J. X.; Xiong, H.; Quirk, R. P.; Cheng, S. Z. D., *J. Am. Chem. Sci.* **2007,** 129, 1113-1121.

(23) Ouarti, N.; Viville, P.; Lazzaroni, R.; Minatti, E.; Schappacher, M.; Deffieux, A.; Borsali, R., *Langmuir* **2005,** 21, 1180-1186.

(24) Rehage, H.; Wunderlich, I.; Hoffmann, H., *Progr. Colloid & Polym. Sci.* **1986,** 59, 51-59.

(25) Turner, M. S.; Cates, M. E., *J. Phys.: Condens. Matter* **1992,** 4, 3719-3741.

(26) Keller, S. L.; Boltenhagen, P.; Pine, D. J.; Zasadzinski, J. A., *Phys. Rev. Lett.* **1998**, 2725-2728.

(27) Vasudevan, M.; Buse, E.; Lu, D. L.; Krishna, H.; Kalyanaraman, R.; Shen, A. Q.; Khomami, B.; Sureshkumar, R., *Nat. Mater.* **2010,** 9, 436-441.

(28) Zhang, M.; Wang, M. F.; He, S.; Qian, J. S.; Saffari, A.; Lee, A.; Kumar, S.; Hassan, Y.; Guenther, A.; Scholes, G.; Winnik, M. A., *Macromolecules* **2010,** 43, 5066-5074.

(29) Wang, C. W.; Sinton, D.; Moffitt, M. G., *J. Am. Chem. Sci.* **2011,** 133, 18853-18864.

(30) Rychkov, I., *Macromol. Theory Simul.* **2005,** 14, 207-242.

(31) Yu, H. Z.; Jiang, W., *Macromolecules* **2009,** 42, 3399-3404.

(32) Wang, C. W.; Bains, A.; Sinton, D.; Moffitt, M. G., *Langmuir* **2012**.

(33) Hayward, R. C.; Pochan, D. J., *Macromolecules* **2010,** 43, 3577-3584.

(34) Chen, Q.; Zhao, H.; Ming, T.; Wang, J.; Wu, C., *J. Am. Chem. Sci.* **2009,** 131, 16650-16651.

(35) Hadjichristidis, N.; Iatrou, H.; Pispas, S.; Pitsikalis, M., *J. Polym. Sci. Part A: Polym. Chem.* **2000,** 38, 3211-3234.

(36) Hong, L.; Jin, F.; Li, J.; Lu, Y.; Wu, C., *Macromolecules* **2008,** 41, 8220-8224.

(37) Jin, F.; Wu, C., *Phys. Rev. Lett.* **2006,** 96, 237801.

(38) Zhao, H.; Chen, Q.; Hong, L.; Zhao, L.; Wang, J.; Wu, C., *Macromol. Chem. Phys.* **2011,** 212, 663-672.

(39) The gas that might be trapped in the fitler membrane could influence the pressure measured. Hence during every extrusion experiment, the gas bubbles have to be carefully removed. Fitler membrane conneted with syringe was positioned upward, just like in a medical injection, and micelles solution were slowly injected to remove macroscopic gas bubbles trapped in the membrane.

(40) Chen, Q.; Wu, C., 2013, *in preparation*.

(41) Zhu, Y.; Granick, S., *Macromolecules* **2002,** 35, 4658-4663.

(42) Zhu, Y.; Granick, S., *Langmuir* **2002,** 18, 10058-10063.

(43) Cheikh, C.; Koper, G., *Phys. Rev. Lett.* **2003,** 91.

(44) de Gennes, P. G., *Adv. Colloid Interface Sci.* **1987,** 27, 189-209.

(45) Taunton, H. J.; Toprakcioglu, C.; Fetters, L. J.; Klein, J., *Macromolecules* **1990,** 23, 571-580.

(46) Klein, J.; Kumacheva, E.; Mahalu, D.; Perahia, D.; Fetters, L. J., *Nature* **1994,** 370, 634-636.

(47) Schorr, P. A.; Kwan, T. C. B.; Kilbey, S. M.; Shaqfeh, E. S. G.; Tirrell, M., *Macromolecules* **2003,** 36, 389-398.

(48) Rotella, C. Ultrathin Polymer Films Probed by Dielectric Relaxation Spectroscopy: Interfacial Effects. 2011.

(49) Rotella, C.; Napolitano, S.; Wuebbenhorst, M., *Macromolecules* **2009,** 42, 1415-1417.

(50) Doi, M.; Edwards, S. F., *The Theory of Polymer Dynamics*. Clarendon: Oxford, 1986.

Chapter 6

How Long Cylindrical Micelles Formed after Extruding Block Copolymer in a Selective Solvent through a Small Pore Fragment back into Spherical Ones

6.1 Introduction

It has been known that amphiphilic block copolymer chains in a solvent only selectively good for one block can assemble into thermodynamically stable spherical or cylindrical micelles or aggregates into kinetically controlled vesicle-like, toroidal and multi-compartment micellar structures,[1-7] depending on their molecular structures. These colloids might have a range of potential applications, including as catalyst supports and drug delivery carriers. Due to each specific application requires a specially designed structure, it is important to understand how each structure is formed and their structure-property relationship. In general, these structures are determined by a balance among the interfacial tension, interaction between collapsed blocks inside the insoluble core, and repulsion between the soluble blocks in the shell.[8-10] The disturbance of such a balance often leads to a transition of one structure to another.

In the last few decades, the control of micelle morphology has been realized by adjusting the composition of block copolymers,[9-12] polymer concentration,[13] solvent composition,[14] temperature,[15,16] or by adding different amounts of homopolymer of the insoluble block.[17] On the kinetically controlled side, varying the shear rate is effective in inducing a morphological transformation of small molecule surfactants[18-21] or polymeric surfactants (amphiphilic block copolymers).[22-25] Recently, Wang et al.[23] used flow to induce a range of morphologies, including cylinders, Y-junctions, bilayers and networks in a gas-liquid micro-fluidic reactor, where spherical micelles are exclusively formed in the off-chip condition. Therefore, their prepared morphologies must be kinetically trapped intermediate metastable states.

Besides many studies on these phenomenal morphology transitions from one into another, some detailed kinetics and mechanism were also revealed. For example,

Burke et al.[26] investigated the sphere-to-rod and rod-to-sphere transitions of polystyrene-*b*-poly(acrylic acid) (PS-*b*-PAA) by a sudden change of the solvent composition by using the solution turbidity and transmission electron microscopy (TEM) measurements. Denkeva et al.[27] examined the solvent-composition-jumping induced sphere-to-rod transition of poly(ethylene oxide)-*b*- poly(propylene oxide)-*b*-poly(ethylene oxide) (PEO-*b*-PPO-*b*-PEO) by using dynamic light scattering and cryo-TEM. Shen et al.[28] reported a crystallization induced sphere-to-cylinder transition of poly(ferrocenyldimethylsilane)-*b*-poly(2-pyridine) (PFS-*b*-P2VP) by using TEM, wide-angle X-ray scattering (WAXS) and laser light scattering (LLS).

However, most of these kinetic studies of the morphology transition induced by the solvent quality change were qualitative. Thus, further quantitative studies are necessary to elicit the mechanisms of these morphology transitions. Guerin et al.[29] recently investigated the mechanism of the fragmentation induced by sonication of long cylindrical micelles made of diblock copolymer poly(isoprene-*b*-ferrocenyldimethylsilane) (PI-*b*-PFS) in a selective solvent. After a comparison of the weight distribution and average length of the micelles obtained from the TEM measurements with those calculated from computer simulation, they found that the fragmentation of a cylindrical micelle follows a Gaussian scission model with a scission rate higher at its central and lower at its ends. They further speculated that biological fibers might also follow a similar mechanism if they were subjected to sonication.

Previously, we found a novel sphere-to-cylinder transition induced by extruding a dispersion of spherical micelles made of diblock copolymer through a small cylindrical pore in a properly chosen solvent mixture.[30] By monitoring the hydraulic pressure change during the extrusion and the solution property differences before and after the extrusion measured by LLS and TEM, we elucidated its mechanism.[31] In these experiments, we also found that such obtained cylindrical micelles were very slowly fragmenting into individual spherical micelles, which is unexpected because we thought that these cylindrical micelles should immediately return to their original thermodynamically stable spherical state. Such a transition after the extrusion was qualitatively studied in different solvent mixtures by LLS. In the current study, we like to have some quantitative understanding of this slow cylinder-to-sphere transition by using a combination of experimental measurements and computer

simulations. The transition is different from previous studies; namely, here thermodynamic conditions of the solution are identical before and after the extrusion and there is no external energy input.

6.2 Experimental Section

6.2.1 Preparation of long cylindrical micelles

Using the extrusion of small spherical micelles made of diblock copolymer chains to produce long cylindrical micelles has been previously reported.[30,31] The outline procedure is as follows. First, a dispersion of spherical micelles made of polystyrene-*b*-polyisoprene diblock copolymer (PS_{285}-*b*-PI_{245}) (subscripts refer the polymerization degrees of each block) was prepared in a mixture of THF and *n*-hexane (13:87 v/v%). After being stored for a sufficient long time to reach its thermodynamically stable state at room temperature, the dispersion of spherical micelles was extruded with a flow rate of 20 mL/hr through small cylindrical pores (20 nm in diameter and 1,000 nm in length purchased from Whatman) by using a 10-mL gastight syringe and a Harvard-2000 syringe pump. The dispersion after the extrusion was collected for both LLS and TEM characterizations.

6.2.2 Laser light scattering (LLS)

A commercial LLS spectrometer (ALV/DLS/SLS-5022F) equipped with a multi-τ digital time correlator (ALV5000) and a cylindrical 22 mW He-Ne laser (λ_0 = 632 nm, Uniphase) as the light source was used. In dynamic LLS, the Laplace inversion of each measured intensity-intensity time correlation function $G^{(2)}(t,q)$ in the self-beating mode can lead to a line-width distribution $G(\Gamma)$. For a pure diffusive relaxation, Γ is related to the translational diffusion coefficient D, i.e., $\Gamma = Dq^2$ at $q \rightarrow 0$ and $c \rightarrow 0$, or further to the hydrodynamic radius R_h by the Stocks-Einstein equation, $R_h = k_B T/6\pi\eta D$, where k_B, T and η are the Boltzmann constant, the absolute temperature and the solvent viscosity, respectively. In static LLS, when $q<R_g^2>^{1/2} < 1$, where $<R_g^2>^{1/2}$ is the *z*-average root-mean- square radius of gyration, we can obtain the weight-average molar mass (M_w) and the $<R_g^2>^{1/2}$ of polymeric micelles in a dilute solution with a concentration of C from the angular dependence of the excess absolute scattering intensity, known as the Rayleigh ratio $R_{vv}(q)$, by

$$\frac{KC}{R_{vv}(q)} \approx \frac{1}{M_w}(1+\frac{1}{3}\langle R_g^2\rangle q^2) + 2A_2C \qquad (6\text{-}1)$$

where C is polymer concentration (g/mL); $K = 4\pi^2 n^2 (dn/dC)^2/(N_A\lambda_0^4)$ and $q = (4\pi n/\lambda_0)\sin(\theta/2)$ with N_A, n, θ, and λ_0 being the Avogadro number, the solvent refractive index, the scattering angle, and the wavelength of the laser light in vacuum, respectively; $P(q)$ is the form factor; and A_2 is the second virial coefficient. In a very dilute solution/dispersion, the correction of $2A_2C$ can be ignored. For a scattering subject much smaller than the observation length ($1/q$), $P(q) \simeq 1 - \langle R_g^2 \rangle q^2/3$; but for a long cylindrical micelle, we have

$$P(q) = \frac{2}{qL}\int_0^{qL} \frac{\sin(qL)}{qL} d(qL) - [\frac{2}{qL}\sin(\frac{qL}{2})]^2 \quad (6\text{-}2)$$

according to the Holter-Casassa analysis for rod-like micelles.[32,33] Further, a weight-average Zimm-Schulz distribution as follows can be used to accommodate long thin cylinders with a uniform diameter but different lengths,[34] i.e.,

$$w(L) = \frac{b^{z+1}}{z!} L^z e^{-bL} \quad (6\text{-}3)$$

where $b = (z+1)/L_w$ and $z = 1/[(L_w/L_n)-1]$ with L_n and L_w are the number- and weight-averaged contour length of the cylinders, respectively.

6.2.3 Transmission electron microscopy (TEM)

The TEM imaging was obtained using an FEI CM 120 microscope operated at 120 kV. For each measurement, ~10 μL of the micelle dispersion was placed onto a carbon-coated copper grid and then dried in ambient air with a hair dryer. The length distribution of the cylindrical micelles after the extrusion was measured over many TEM images using Adobe Acrobat.

6.2.4 Computer simulation

Using the Monte Carlo simulation, we performed a trial "scission" of the connection between two adjacent spherical micelle units on each cylindrical micelle. The samples employed in the simulation were constructed on the basis of the initial length distribution experimentally obtained from the TEM analysis. By giving each cylindrical micelle a certain chance or a certain "reaction" rate to break up in each Monte Carlo cycle, we are able to trace the evolution of the length distribution of the cylindrical micelles and then compare them with that from the TEM analysis.

6.3 Results and Discussion

Previously, we found that long thin cylindrical micelles after the extrusion are severely inter-crossed in the TEM images so that it was difficult to distinguish one from another. In the current study, we used a solvent mixture of *n*-hexane and isopropanol (8:1, v/v) to "freeze" and dilute the micelle dispersion after the extrusion before carrying out the sample preparation for the TEM analysis. This is because isopropanol is a poor solvent for both PS and PI and completely miscible with *n*-hexane. Here, the composition of the solvent mixture is properly and optimally chosen because a higher content of isopropanol leads to visible aggregates of spherical micelles before the extrusion, while a lower content of isopropanol cannot "freeze" those cylindrical micelles after the extrusion for the TEM analysis. Using this method, long cylindrical micelles obtained after the extrusion are stable in the solvent mixture, reflected in a constant measured scattering intensity even after months and the TEM images.

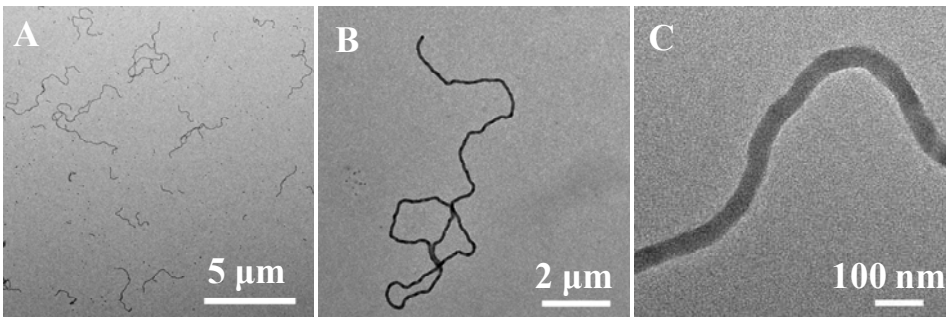

Figure 6.1. Representative TEM images with different magnifications of cylindrical micelles just after extruding small spherical micelles in a solvent mixture of THF and *n*-hexane (13:87 v/v%) through small cylindrical pores (20 nm × 1,000 nm).

Figure 6.1 shows that besides those long cylindrical micelles with a diameter of ~ 40 nm and a length over micrometers, there are also many small spherical and short cylindrical micelles in the dispersion after the extrusion, indicating that the extrusion-induced sphere-to-cylinder transition is not 100%. In addition, under the dispersion conditions, spherical micelles are thermodynamically favored while worm-like cylindrical micelles are only kinetically trapped and in a metastable state. In principle, the transition back to spherical micelles would start as soon as cylindrical micelles leave the cylindrical pores. However, we surprisingly and experimentally found that such a cylinder-to-sphere transition in the dispersion after

the extrusion lasted from minutes to weeks, depending on the dispersion conditions. For example, the transitions in the solvent mixtures of THF and *n*-hexane (22:78 and 17:83, v/v%) were completed in ~10 min and 1 day, respectively. In the current study, we typically used a solvent mixture of THF and *n*-hexane (13:87, v/v%), to slow down the transition so that we are able to study its morphological change in details by using a combination of LLS and TEM.

6.3.1 LLS studies of cylinder-to-sphere transition

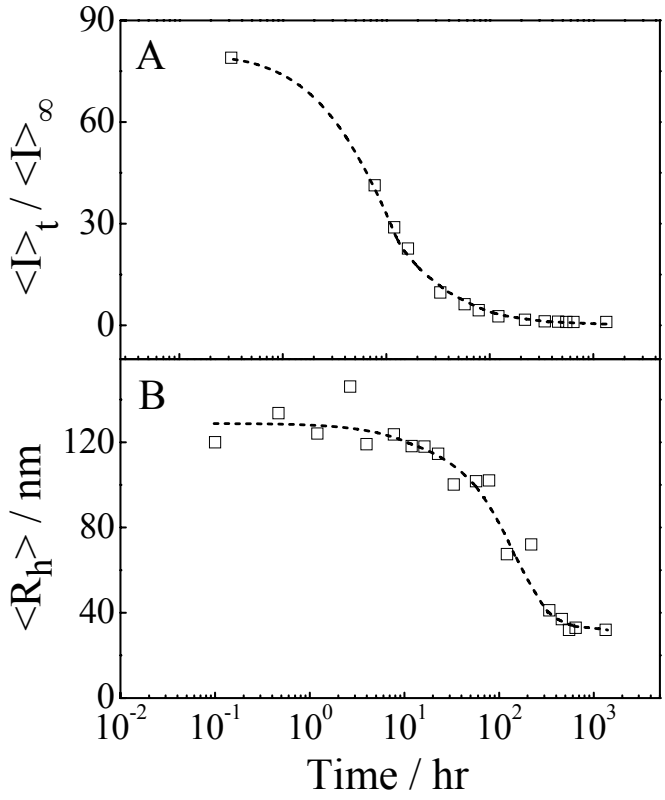

Figure 6.2. Time dependence of average intensity ratio ($<I>_t$ /$<I>_\infty$) of scattered light at q → 0 and average hydrodynamic radius $<R_h>$ during cylinder-to-sphere transition, where long cylindrical micelles were obtained from extrusion of small spherical micelles prepared in a solvent mixture of THF and *n*-hexane (13:87, v/v%).

Figure 6.2 shows that the measured average intensity of the scattered light gradually decays ~80 times, and at the same time, the average hydrodynamic radius decreases from ~140 nm to ~30 nm two weeks after the extrusion. Note that the scattering intensity is proportional to the square of the molar mass of a scattering subject. Therefore, LLS is very sensitive to longer cylindrical micelles. The decay of

<*I*> in Figure 6.2 indicates the breaking down of longer cylindrical micelles into shorter ones and eventually into small spherical micelles. Such a process can be reasonably represented with a bi-exponential function using the nonlinear least-squares fitting with no specific physical meanings about the two relaxation modes.

In literature, Winnik and his coworkers[29,35] characterized long cylindrical micelles made of crystalline-coil diblock copolymers, such as PFS-*b*-PI and PFS-*b*-P2VP, in dispersions using static LLS on the basis of the Holtzer-Casassa model (eq. 2) for thin and rigid rods with a long persistence length, in which both average molar mass and length of cylindrical micelles (denoted as M_w^{SLS} and L_w^{SLS}) were obtained. On the other hand, long cylindrical micelles made of coil-coil diblock copolymers, such as PS-*b*-PI, were also studied by static LLS,[36,37] where only the average linear density was estimated from the Holtzer-Casassa fitting because those cylindrical micelles are too long and too broadly distributed in length.

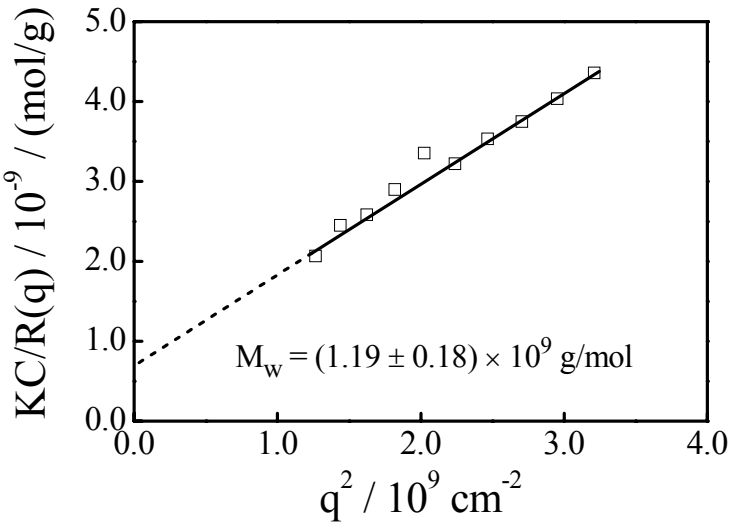

Figure 6.3. Plot of KC/R(q) versus q^2 of long cylindrical micelles in dispersion just after their formation in extrusion of small spherical micelles through small cylindrical pores (20 nm).

Figure 6.3 shows that the extrapolation of $KC/R(q)$ to $q \rightarrow 0$ yields M_w = (1.19 ± 0.18) × 10^9 g/mol, where copolymer concentration is 5 × 10^{-4} g/mL and d*n*/d*c* = 0.20 mL/g.[38] On the other hand, we can plot the data as $qR(q)/\pi KC$ over q. The value of $qR(q)/\pi KC$ approaches a constant even at a very low q, indicating the presence of some extremely long rods.[39] Thus, rather than applying eq. (6-2) to the data analysis, we only use the data of $P(q)$ in the high q region to estimate the average molar mass

per unit length of cylindrical micelles, i.e., the average linear density ($<\rho>_{linear}$), as shown in Figure 6.4. Note that its value (2.51 ± 0.06) × 10^5 g/mol/nm is fairly close to that (1.55-2.65 × 10^5 g/mol/nm) reported for cylindrical micelles made of PS-*b*-PI in *N*,*N*-dimethylacetamide.[36]

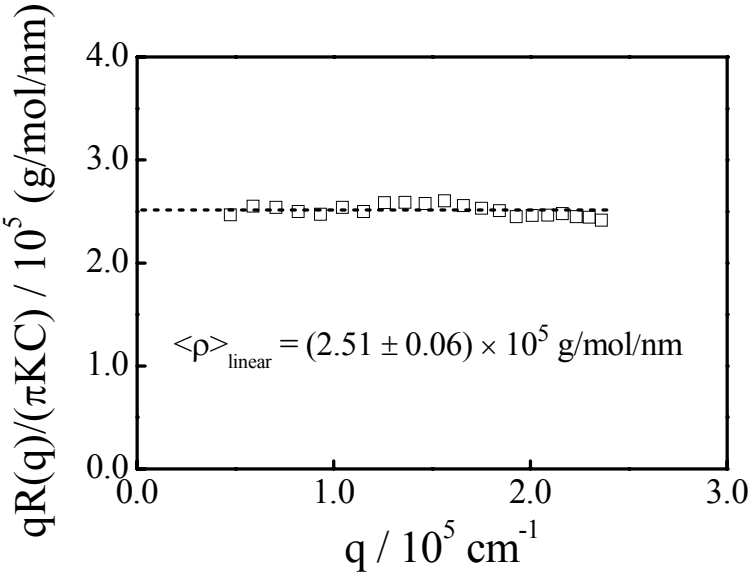

Figure 6.4. Plot of qR(q)/πKC versus q of long cylindrical micelles in dispersion just after their formation in extrusion of small spherical micelles through small cylindrical pores (20 nm).

Further dividing $<\rho>_{linear}$ by the average molar mass of diblock copolymer chains results in the average aggregation number per unit length ($<n>$ ~ 5.4 ± 0.1 nm^{-1}). Therefore, we are able to estimate the weight-average length of long cylindrical micelles ($L_{w,0}$) just after the extrusion from $M_w/<\rho>_{linear}$, i.e., $L_{w,0}$ = $M_w/<\rho>_{linear}$ = 4.7 ± 0.1 μm. Using such a strategy, we estimated the time dependent weight-average length of cylindrical micelles ($L_{w,t}$) until most of cylindrical micelles were broken down to small spherical ones. It is worth-noting that LLS only measures averaged values, and at a later stage of the transition, the dispersion contains lots of small spherical micelles so that the measured values does not reflect true parameters of remaining long cylindrical micelles. Besides, the cylinder-to-sphere transition continues during the LLS measurement, which further brings uncertainties for the estimated L_w from LLS. Therefore, we used TEM to analyze the time dependent average contour length of cylindrical micelles. As mentioned before, for TEM measurements, we used a mixture of *n*-hexane and isopropanol to "freeze" and dilute cylindrical micelles.

6.3.2 TEM studies of cylinder-to-sphere transition

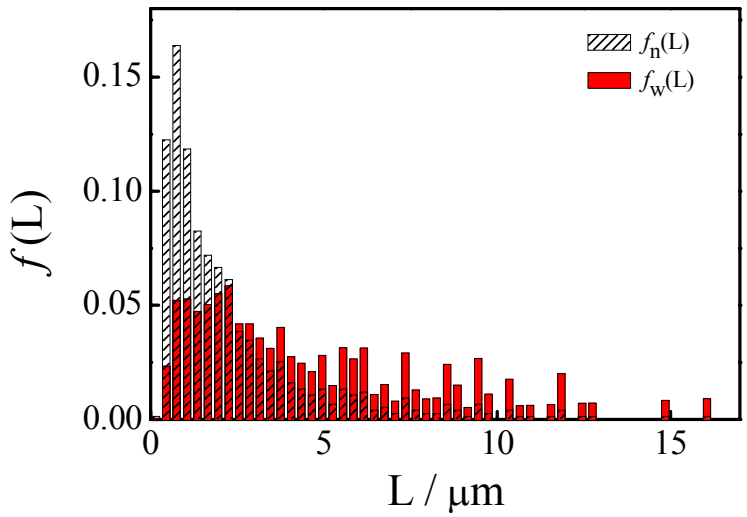

Figure 6.5. TEM characterization of number and weight distribution of length of cylindrical micelles just after their formation in extrusion of small spherical micelles through small cylindrical pores (20 nm).

Figure 6.5 reveals that cylindrical micelles have a very broad length distribution, ranging from hundreds of nanometers to tens micrometers after measuring more than 600 micelles in TEM images. Considering that small spheres and short cylinders can potentially influence our statistical analysis, we only analysis those cylindrical micelles with a length longer than 400 nm, i.e., those made of ten or more spherical micelles. Such a procedure is also applied to the time dependent TEM analysis. Figure 6.5 shows that the number distribution highlights shorter cylindrical micelles with a peak at ~0.7-0.8 μm. To compare the TEM and LLS results, we also calculated the weight distribution of length of cylindrical micelles, $f_w(L)$, by using

$$f_w(L_i) = \frac{L_i N_i}{\sum_i L_i N_i} \tag{6-4}$$

where N_i is the number of cylinders with a length of L_i, which is also plotted in Figure 6.5.

Figure 6.6 shows time dependent TEM images of cylindrical micelles in the dispersion. In comparison with Figure 6.1 (just after the extrusion, i.e., t = 0), the average length of cylindrical micelles becomes shorter and more spherical micelles are visible. After two weeks, only spherical micelles are observable in the TEM images. Using these TEM images, we characterized time-dependent number

distribution of length of cylindrical micelles and calculated the number- and weight-average lengths (L_n and L_w) of cylindrical micelles at different dissociation times, which are summarized in Table 1.

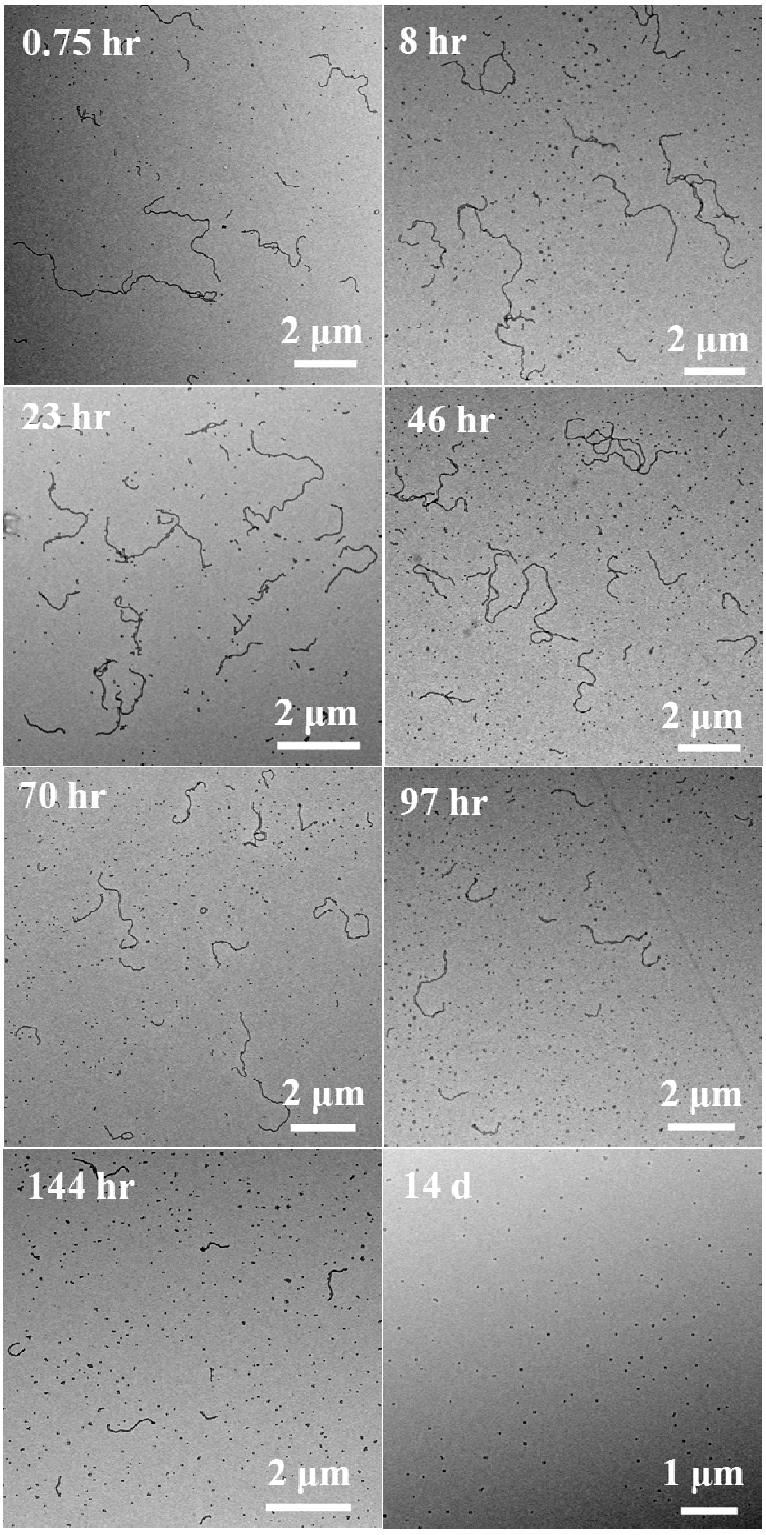

Figure 6.6. TEM images of cylindrical micelles during cylinder-to-sphere transition.

Table 6.1. TEM estimated number- and weight-average length of cylindrical micelles at different times during cylinder-to-sphere transition after extrusion.

Dissociation time / hr	0	0.75	8	23	46	70	97	144
L_n / μm	2.3	2.3	2.2	2.0	1.9	1.6	1.4	1.0
L_w / μm	4.6	4.3	4.2	3.5	3.4	2.8	2.2	1.4
L_w/L_n	2.0	1.9	2.0	1.7	1.7	1.7	1.5	1.4

Figure 6.7 shows that the weight-average length of cylindrical micelles from TEM gradually decreases due to the cylinder-to-sphere transition; while that from LLS decreases much faster. Note that just after the extrusion but before the transition, the results from TEM and LLS agree well with each other. The discrepancy between the results of TEM and LLS during the transition is understandable since LLS characterizes an average size over all the scattering subjects in the dispersion, including lots of small spherical and fragmented short cylindrical micelles; while in the current TEM study, we only selectively measure cylindrical micelles longer than 400 nm, similar as what we did in the computer simulation as follows.

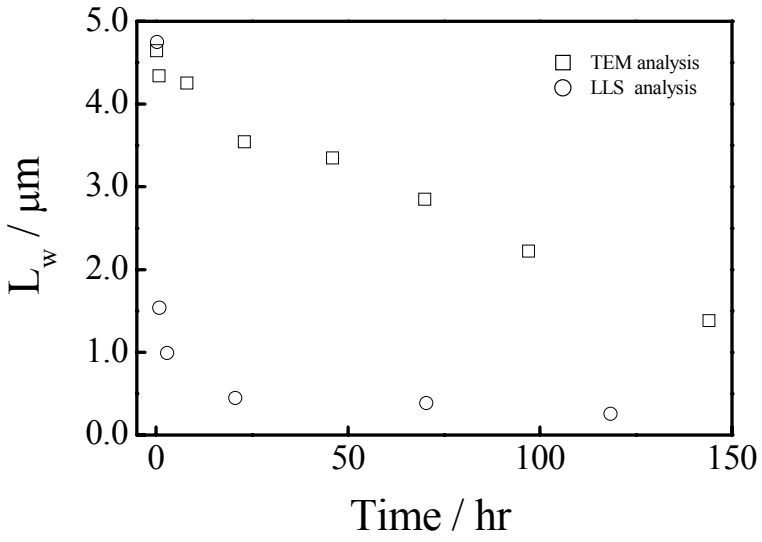

Figure 6.7. Plot of the micelles weight-average length as a function of time, estimated from TEM images analysis and LLS analysis.

6.3.3 Computer simulations

In the past, the degradation of polymer chains under a shear stress has been extensively studied, including the effects of the ultrasonication, freeze-thaw cycles or elongation force generated by a flow field.[40-43] The main purpose of these previous studies were to unearth the fracture mechanism, which led to different models to account for different distributions of fracture sites along the chain. For example, using computer simulations, Ballauff and Wolf[44] calculated the resultant molar mass distribution of polymer chains under models of random, Gaussian, and central scissions. Later, Tanigawa et al[42] studied the degradation mechanism of double-stranded nucleic acids under sonication by comparing the changes of the measured and calculated molar mass distributions from gel permeation chromatography coupled with a low-angle LLS detector and the computer simulation, respectively.

Our cylinder-to-sphere transition is similar to polymer degradation if we regard each long cylindrical micelles are made of many small spherical subunits that are temporarily connected by sufficiently strong physical interaction, while in a polymer chain monomers are linked together by much stronger chemical bonds. This is why the thermal fluctuation is sufficient to drive the cylinder-to-sphere transition with no external stimulus. In our simulation, some specificities and assumptions were added to previous models as follows. First, each long cylindrical micelle can rupture into shorter segments that will not be able to recombine back into a longer one because the thermodynamically stable state is individual spherical micelles. Namely, each cylindrical micelle with a length L_i (made of i spherical micelles, subunits) can split into two shorter ones with j and i-j subunits with scission rate constant of k_{ij}. Second, the degradation follows the first-order reaction with respect to the concentration of micelles. Third, the transition (scission) is a thermodynamically controlled process, driven by the total free energy change, where the entropy part includes the configuration entropy of long cylindrical micelles as a flexible “chain”, depending on its length; while the enthalpy part contains the time-dependent repulsion in the shell. For the sake of simplicity, we adopted a power-law between its contour length and fracture time. Fourth, we defined individual spherical micelles as a final thermodynamically stable state on the basis of our experimental results, which is different in the simulated degradation of a polymer chain where individual monomers are not the final state. In our simulation, we exclusively studied the

fragmentation of those cylindrical micelles made of ten or more spherical micelle subunits so that we can compare the TEM and simulated results. In the Monte Carlo simulation, we first made initial cylindrical micelles with a length distribution obtained from TEM analysis and then used three different fundamental "scission" models to study the scission kinetics.

In the end-scission mode (I), small spherical micelles are breaking off from the ends of a cylindrical micelle with i subunits so that the scission rate constant k_{ij} of the subunits is independent of its length, but related to time, where

$$k_{ij} = k_0\ t^Y \qquad if\ \ j = 1,\ or\ \ i - 1 \tag{6-5}$$

where k_0 is the initial breaking rate constant, depending on the temperature and the micelle dispersion conditions and Y is a constant, describing the time dependent scission rate constant. In the random-scission model (II), each scission site has an identical probability to break so that the scission rate constant k_{ij} is dependent of the micelle length and time, i.e.,

$$k_{ij} = k_0 (i-1)^X t^Y \qquad if\ \ \ 0 < j < i \tag{6-6}$$

where X is a constant, describing the length dependent scission rate constant. In the Gaussian- scission model (III), the probability of scission sites is Gaussian distributed with its highest probability located in the middle of a cylindrical micelle and an adjustable deviation σ_j as

$$k_{ij} = k_0 (i-1)^X t^Y \frac{1}{\sigma_j \sqrt{2\pi}} \exp[-(j - \frac{i}{2})^2 / 2\sigma_j^2] \qquad if\ \ \ 0 < j < i \tag{6-7}$$

where $\sigma_j = iR$. As $\sigma_j \rightarrow 0$ or ∞, the model becomes to the central- or random-scission model. More quantitatively, $R < 0.05$ and > 10 are two limits.

Using the experimentally determined initial length distribution (Figure 6.5), we simulated the cylinder-to-sphere transition by using the above three scission models and calculated the time-dependent weight-average length. Figure 6.8 summaries our simulated results. It is clear that the simulated and measured weight-average length have a similar relaxation behavior. Note that both X and Y are physically meaningful and account for the length and time dependences, respectively, and R defines the location range of the scission site along a given cylindrical micelle. The best fittings of our experimentally measured L_w lead to $Y = 0.5$ for Model I; $X = 0.9$ and $Y = 0.2$ for Model II; and $X = 0.9$, $Y = 0.2$ and $R = 0.35$ for Model III. Figure 6.8 shows that both the random and Gaussian scission models agree with the experimental results

well but not the end-scission model.

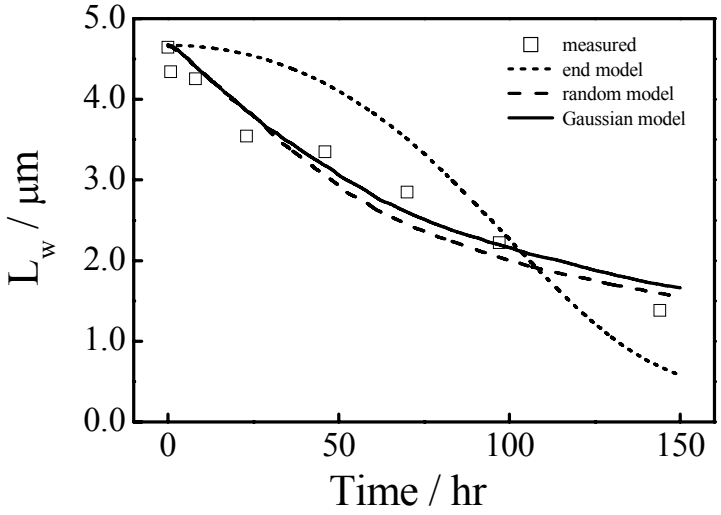

Figure 6.8. Time dependence of simulated weight-average length (L_w) of cylindrical micelles during cylinder-to-sphere transition under thermal fluctuation by using end-scission model (Y = 0.5), random-scission model (X = 0.9 and Y = 0.2) and Gaussian-scission model (X = 0.9, Y = 0.2 and R = 0.35), where experimental results from TEM analysis are also plotted for comparison and time is measured with Monte Carlo cycles by same ratio.

Note that in literature polymer chains degradation and cylindrical micelles fragmentation led to a plateau that is much higher than the molar mass of monomers or larger than the size of individual spherical micelles even under a strong and long-time sonication. While in the current study, nearly all cylindrical micelles were fragmented into small spherical micelles at the end. An attentive reader can find the population of spherical micelles in the images of Figure 6.6 steadily increases with the time. If the fragmentation exclusively was governed by the random- or Gaussian-model, we would not be able to see such an increase of small spherical micelles. To explain such a discrepancy between Figures 6.6 and 6.8, let us go back to see how long cylindrical micelles are formed in the extrusion. As shown in Figure 6.9, each cylindrical micelle contains a string of partially interconnected "pearls" (spherical micelles), presumably due to the compression and forced fusion of small spherical micelles inside the long cylindrical pore. Such formed cylindrical micelles are different from the conventional PS core–PI shell micelles formed via the self-assembly in solution.[35,45] This is why an external force is not required to fragment our cylindrical micelles.

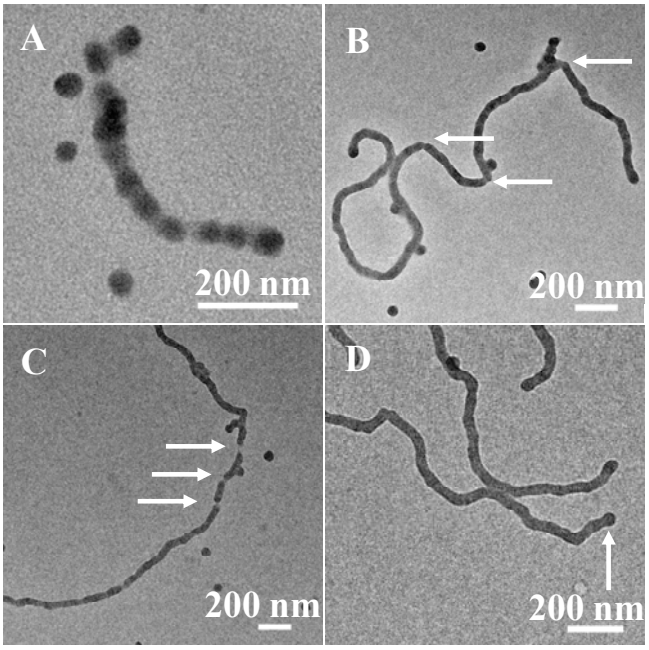

Figure 6.9. TEM images of (A) "pearl-like" structure; (B) and (C) "defects" and "breaking sites"; and (D) "budding" at ends of a cylindrical micelle.

In comparison with the classic Rayleigh-instability,[46-48] in which the surface tension breaks a cylindrical fluid stream into droplets, different contributions to the total free energy in the transition of micelle morphology is more complicated. Considering a cylindrical micelle as a breakable chain, a simple calculation of its length-dependent configuration entropy indicates that it prefers a scission in the middle.[49] Figure 6.9B shows some observable defects marked by arrows in a cylindrical micelle. Long cylindrical micelles finally fragment into few shorter segments, as shown in Figure 6.9C by arrows. If only considering the surface tension, we would expect that each spherical micelle would tend to break off at the ends of a cylindrical micelle, similar to the Rayleigh instability description. Further, Figure 6.9D shows a cap that is slightly thicker at each end of a cylindrical micelle (also marked by arrow).

Our current experimental results finally lead us to a scission mechanism that combines the Gaussian- and end-scissions, wherein we assume that the scission probability at the two ends is higher; while the probability at other places follows the Gaussian distribution. A parameter of p is introduced to weight the end scission probability. Therefore, the reaction rate constant of the jth subunit along a cylindrical micelle is expressed by a piecewise function as

$$k_{ij} = \begin{cases} pk_0(i-1)^X t^Y & \text{if } j = 1, \text{ or } i-1 \\ k_0(i-1)^X t^Y \dfrac{1}{\sigma_j\sqrt{2\pi}} \exp[-(j-\dfrac{i}{2})^2 / 2\sigma_j^2] & \text{otherwise} \end{cases} \quad (6\text{-}8)$$

Using the Arrhenius equation estimation, we know that the slight free energy preference of k_BT, 2 k_BT, 3 k_BT, or 4 k_BT for the end scission leads to p = 2.7, 7.4, 20 or 54. The simulation results in the weight distribution of cylindrical micelle length and its corresponding weight average length, which are summarized and compared with the TEM analysis in Figure 6.10. It shows that the measured and simulated weight distributions of length of cylindrical micelles agree well with each other when p = 20 was used, i.e., if the end scission has 3 k_BT free energy preference. The value of X = 0.9 reflects that the scission rate constant is nearly a linear function of the micelle length, consistent with previous studies of polymer degradation. On the other hand, the positive value of Y = 0.2 reveals that the scission rate constant slightly increases with time, which is different from the polymer degradation or the fragmentation of cylindrical micelles under a shear force. Such a time dependent scission rate constant might be explained as follows. The thermal fluctuation agitates each cylindrical micelle to move in the dispersion and constantly change its conformation to create some kinks and defects between two fused and adjacent spherical micelles. The thermal agitation of shorter cylinders should be easier than that of long ones, causing more kinks and defects per unit length for shorter cylinders. As the fragmentation proceeds, each cylindrical micelle becomes shorter so that the scission rate constant becomes larger.

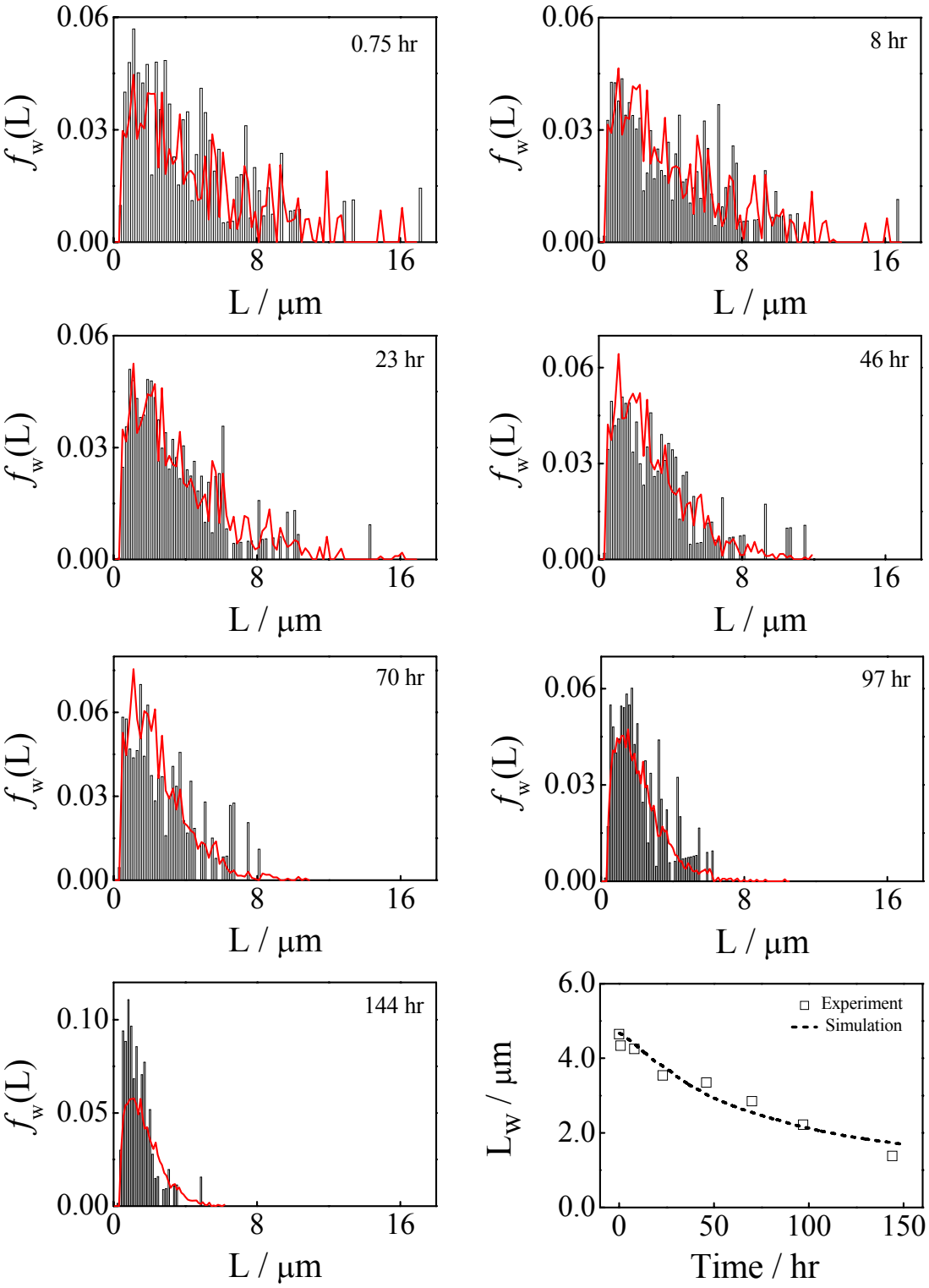

Figure 6.10. Time dependence of weight distribution of length of cylindrical micelles, where black bars: TEM results; red curves: simulation results, and bottom right figure compares calculated and measured weight average lengths with best fitting parameters ($X = 0.9$, $Y = 0.2$, $R = 0.35$, and $p = 20$).

6.4 Conclusion

Extruding small spherical micelles made of polystyrene-*b*-polyisoprene (PS-*b*-PI) diblock copolymer in a proper mixture of THF and *n*-hexane through smaller cylindrical pores can generate long cylindrical micelles with a uniform diameter of 40 nm and a broadly distributed length. The TEM analysis shows that the weight-average length is about 4.6 μm. The thermal fluctuation agitates each cylindrical micelle to undergo a cylinder-to-sphere transition and fragment into individual thermodynamically stable spherical micelles. The fragmentation rate strongly depends on the solvent composition, ranging from minutes to days. A comparison of measured and simulated weight average length reveals that the transition kinetics is governed by a model that combines both the Gaussian-scission model with its highest scission preference located in the middle of a cylinder and the end-scission model with a higher scission rate at the two ends of a cylinder. Our current study indicates that the scission rate constant is nearly proportional to the micelle length and slightly increases with the time. We can conclude that the scission mechanism of long cylindrical micelles formed after the extrusion with the spherical phase as its thermodynamically stable state is different from those previously observed under an external shear force for long cylindrical micelles formed via the self-assembly of amphiphilic block copolymers in a selective solvent, where the thermodynamically stable state is the cylindrical phase.

6.5 References and Notes

(1) Lazzari, M.; Liu, G.; Lecommandoux, S., *Block Copolymers in Nanoscience*. WILEY-VCH, Weinheim, 2006.

(2) Gohy, J. F., *Adv. Polym. Sci.* **2005,** 190, 65-136.

(3) Riess, G., *Progr. Polym. Sci.* **2003,** 28, 1107-1170.

(4) Pochan, D. J.; Chen, Z. Y.; Cui, H. G.; Hales, K.; Qi, K.; Wooley, K. L., *Science* **2004,** 306, 94-97.

(5) Li, Z. B.; Kesselman, E.; Talmon, Y.; Hillmyer, M. A.; Lodge, T. P., *Science* **2004,** 306, 98-101.

(6) Moughton, A. O.; Hillmyer, M. A.; Lodge, T. P., *Macromolecules* **2012,** 45,

2-19.

(7) Groschel, A. H.; Schacher, F. H.; Schmalz, H.; Borisov, O. V.; Zhulina, E. B.; Walther, A.; Muller, A. H. E., *Nat. Commun.* **2012,** 3. 710-719.

(8) Zhulina, E. B.; Borisov, O. V., *Macromolecules* **2012,** 45, 4429-4440.

(9) Zhang, L.; Eisenberg, A., *Science* **1995,** 268, 1728-1731.

(10) Zhang, L.; Eisenberg, A., *J. Am. Chem. Soc.* **1996**, 3168-3181.

(11) Jain, S.; Bates, F. S., *Science* **2003,** 300, 460-464.

(12) Zhulina, E. B.; Adam, M.; LaRue, I.; Sheiko, S. S.; Rubinstein, M., *Macromolecules* **2005,** 38, 5330-5351.

(13) Zhang, L.; Eisenberg, A., *Macromolecules* **1999**, 2239-2249.

(14) Bang, J.; Jain, S.; Li, Z.; Lodge, T. P.; Pedersen, J. S.; Kesselman, E.; Talmon, Y., *Macromolecules* **2006,** 39, 1199-1208.

(15) LaRue, I.; Adam, M.; Pitsikalis, M.; Hadjichristidis, N.; Rubinstein, M.; Sheiko, S. S., *Macromolecules* **2006,** 39, 309-314.

(16) Bhargava, P.; Tu, Y.; Zheng, J. X.; Xiong, H.; Quirk, R. P.; Cheng, S. Z. D., *J. Am. Chem. Soc.* **2007,** 129, 1113-1121.

(17) Ouarti, N.; Viville, P.; Lazzaroni, R.; Minatti, E.; Schappacher, M.; Deffieux, A.; Borsali, R., *Langmuir* **2005,** 21, 1180-1186.

(18) Rehage, H.; Wunderlich, I.; Hoffmann, H., *Progr. Coll. Polym. Sci.* **1986,** 59, 51-59.

(19) Turner, M. S.; Cates, M. E., *J. Phys.: Condens. Matter* **1992,** 4, 3719-3741.

(20) Keller, S. L.; Boltenhagen, P.; Pine, D. J.; Zasadzinski, J. A., *Phys. Rev. Lett.* **1998**, 2725-2728.

(21) Vasudevan, M.; Buse, E.; Lu, D. L.; Krishna, H.; Kalyanaraman, R.; Shen, A. Q.; Khomami, B.; Sureshkumar, R., *Nat. Mater.* **2010,** 9, 436-441.

(22) Zhang, M.; Wang, M. F.; He, S.; Qian, J. S.; Saffari, A.; Lee, A.; Kumar, S.; Hassan, Y.; Guenther, A.; Scholes, G.; Winnik, M. A., *Macromolecules* **2010,** 43, 5066-5074.

(23) Wang, C. W.; Sinton, D.; Moffitt, M. G., *J. Am. Chem. Soc.* **2011,** 133, 18853-18864.

(24) Rychkov, I., *Macromol. Theory Simul.* **2005,** 14, 207-242.

(25) Yu, H. Z.; Jiang, W., *Macromolecules* **2009,** 42, 3399-3404.

(26) Burke, S. E.; Eisenberg, A., *Langmuir* **2001,** 17, 6705-6714.

(27) Denkova, A. G.; Mendes, E.; Coppens, M. O., *J. Phys. Chem. B* **2009,** 113, 989-996.

(28) Shen, L.; Wang, H.; Guerin, G.; Wu, C.; Manners, I.; Winnik, M. A., *Macromolecules* **2008,** 41, 4380-4389.

(29) Guerin, G.; Wang, H.; Manners, I.; Winnik, M. A., *J. Am. Chem. Soc.* **2008,** 130, 14763-14771.

(30) Chen, Q.; Zhao, H.; Ming, T.; Wang, J.; Wu, C., *J. Am. Chem. Soc.* **2009,** 131, 16650-16651.

(31) Chen, Q.; Wang, J.; Wu, C., **2013**, in preparation.

(32) Holter, A., *J. Polym. Sci.* **1955,** 17, 432-434.

(33) Casassa, E. F., *J. Am. Chem. Soc.* **1956,** 78, 3980-3985.

(34) Zimm, B. H., *J. Chem. Phys.* **1948,** 16, 1099-1117.

(35) Wang, X.; Guerin, G.; Wang, H.; Wang, Y.; Manners, I.; Winnik, M. A., *Science* **2007,** 317, 644-647.

(36) Liu, G. J.; Li, Z.; Yan, X. H., *Polymer* **2003,** 44, 7721-7727.

(37) LaRue, I.; Adam, M.; da Silva, M.; Sheiko, S. S.; Rubinstein, M., *Macromolecules* **2004,** 37, 5002-5005.

(38) The largest radius of gyration of the cylindrical micelles solution was estimated to be about 600 nm and it was impossible to exactly satisfy the $q R_g < 1$ for our LLS apparatus. We use the data from 15^o to 25^o to roughly estimate the overall weight-average molecular mass for the long cylinders.

(39) Schmidt, M.; Paradossi, G.; Burchard, W., *Macromol. Chem. Rapid Commun.* **1985,** 6, 767-772.

(40) Basedow, A. M.; Ebert, K. H., *Adv. Polym. Sci.* **1977,** 22, 83-148.

(41) Ballauff, M.; Wolf, B. A., *Adv. Polym. Sci.* **1988,** 85, 1-31.

(42) Tanigawa, M.; Suzuto, M.; Fukudome, K.; Yamaoka, K., *Macromolecules* **1996,** 29, 7418-7425.

(43) Tayal, A.; Khan, S. A., *Macromolecules* **2000,** 33, 9488-9493.

(44) Ballauff, M.; Wolf, B. A., *Macromolecules* **1981,** 14, 654-658.

(45) Won, Y. Y.; Davis, H. T.; Bates, F. S., *Science* **1999,** 283, 960-963.

(46) Chen, J. T.; Zhang, M. F.; Russell, T. P., *Nano Letters* **2007,** 7, 183-187.

(47) Fan, P. W.; Chen, W. L.; Lee, T. H.; Chiu, Y. J.; Chen, J. T., *Macromolecules* **2012,** 45, 5816-5822.

(48) Huang, Y. C.; Fan, P. W.; Lee, C. W.; Chu, C. W.; Tsai, C. C.; Chen, J. T., *ACS Appl. Mater. Interfaces* **2013,** 5, 3134-3142.

(49) Glynn, P. A. R.; Van Der Hoff, B. M. E.; Reilly, P. M., *J. Macromol. Sci. Chem.* **1972,** A6, 1653-1664.

Chapter 7
Nanoparticle-Loaded Cylindrical Micelles from Nanopore Extrusion of Block Copolymer Spherical Micelles

7.1 Introduction

Amphiphilic block copolymers in solution can self-assemble into colloidal nanostructures including spheres, cylinders, vesicles as well as those aggregates with more complex structures.[1-5] Although these nanostructures are very fascinating, they are quite limited when thinking about their applications in material science, nanotechnology or nanomedicine. Then the incorporation of functional components into the polymer architecture is preferred. Inorganic/polymer hybrid materials recently have attracted overwhelming interests not only for their ability to combine the advantageous optical, electronic, magnetic, and photocatalytic properties of the constituent materials, but also for the synergistic interactions between the dopant and polymer matrix.[6-8] Functional metal nanoparticles, such as gold nanoparticles, magnetic nanoparticles, and quantum dots have been widely investigated for their promising applications in targeted cancer imaging, therapy, biomedicine, biosensors as well as traditional catalysis because of their excellent physical and chemical properties.[9-12] Further encapsulation of those nanoparticles within amphiphilic polymer micelles in solution phase have been realized, commonly using a "precipitation" processing route.[13-20] In this method, water is added to a solution of amphiphilic block copolymers and hydrophobic nanoparticles initially dispersed in a good solvent for both materials. As a result of simultaneous desolvation of both the nanoparticles and the hydrophobic block of the amphphilic block copolymers, nanoparticles are incorporated into the cores of the final copolymer micelles. However, this method is only limited in spherical hybrid micelles, because further desolvation of the hydrophobic block would not easily result in the hybrid cylindrical micelles, but only the solidification or aggregation of the spherical hybrid micelles.

On the other hand, compared with polymer that are prepared in thin film or bulk forms, the one-dimensional nanofibers are of considerable interest, not only because of their unique properties such as a high specific surface area, a high aspect ratio and

easy electron transfer, but also for their potential applications including energy storage[21] tissue regeneration[22] and drug delivery.[23] For example, the linear structures of polyethylene nanofibers can promote the directed transport of electrons or heat.[24] Filomicelles can function as nano-carrier to effectively deliver the anticancer drug with long circulation time and sustained drug release.[23] When these linear nanostructures are modified further through the introduction of functional nanoparticles, they can be applied for photocatalysis,[25] and hyperthermia treatment in cancer therapy.[26]

Desired properties of nanofibers often include nanometric dimensions, versatile labeling and functionalization, high stability and nanoparticles with homogeneous distribution. The most commonly employed methods include electrospinning,[27, 28] template-assisted methods[29-34] and self-assembly.[35, 36] However, the template-assisted methods have a prerequisite for electrostatic interaction or coordination of possible precursor metal ion to the polymer block while the self-assembly of pre-formed nanoparticles into nanofibers need a precise control of co-assembly behavior of nanoparticles and one polymer block in order to obtain cylindrical micelles. Instead, the synthesis of hybrid spherical micelles is comparably easy. As far as we know, an effective but also facile method for the synthesis of hybrid cylindrical micelles is still lacking.

Previously, we have developed a novel sphere-to-cylinder transition induced by nanopore extrusion of the block copolymer spherical micelles in the solution.[37] In the current study, we report for the first time the generation of gold nanoparticle/polymer cylindrical micelles by using extrusion of the spherical micelles through small cylindrical pores. The block copolymer spherical micelles before extrusion were pre-loaded with gold nanoparticles, by incorporating the polymer coated gold nanoparticles. This nanopore extrusion provides a convenient approach for the generation of multifunctional inorganic/organic hybrid nanomaterials.

7.2 Experimental Section

7.2.1 Preparation for the thiol-capped AuNPs

The dodecanethiol coated AuNPs were prepared in organic phase according to a method described in the literature.[38] Briefly, to a screw-capped test tube equipped with a magnetic stirring bar were added $HAuCl_4 \cdot 4H_2O$ (0.1 mmol, 41.2 mg),

dodecanthiol (0.1 mmol, 23.9 μL) and 5 mL anhydrous THF. Resulting mixture was vigorously stirred for more than 5 hr at room temperature to form transparent yellow solution. Triethylsilane (0.5 mmol, 80 μL) dissolved in about 0.5 mL anhydrous THF was then quickly added to form immediately a purple solution. After stirring for another 5 hr, an excess of methanol was used to quench the mixture and precipitate the product, which was separated by centrifugation, washed with methanol, and dried under reduced pressure. The final brown powder was dissolved in THF to a final mass concentration of 2.0 mg/mL with average diameters of 6.6 ± 0.4 nm from Figure 7.1A and adsorption peak at 522 nm for the UV-vis spectra from Figure 7.2A.

7.2.2 Synthesis of PS_{285}-*b*-PI_{245} and PS_{110}-SH

The diblock copolymer, PS_{285}-*b*-PI_{245} was prepared by sequential anionic polymerization in THF as described in a previous publication from this group.[39, 40] On the other hand, the thiol terminated polystyrene (PS_{110}-SH) was also prepared by anionic polymerization of polystyrene, followed by titrating with propylene sulfide (~ 2 eq) before determination using acidic methanol.[41] Briefly, THF was distilled as needed from poly(styryl)lithium into calibrated ampoules and further isolated with stopcock. Styrene was purified first by stirring over finely grounded calcium hydride followed by fractional distillation into ampoules in presence of dibutylmagnesium and then was distilled into calibrated ampoules, followed by stopcock isolation. Propylene sulfide was purified simply by stirring over finely grounded calcium hydride and degassing on the high vacuum line followed by distillation into calibrated ampoules and further isolation. Acidic methanol (glacial acetic acid to methanol volume ratio of 1:1) was degassed on the high vacuum line before distillation into ampoules. Styrene was polymerized in solvent THF after initiation at -78 ^{o}C with *n*-butyllithium. After 3 hr reaction, 2 eq of propylene sulfide was added. After further stirring for 10 min, the living chains were terminated using acidic methanol, followed by precipitation in excess methanol. Both the block copolymer PS-*b*-PI and PS-SH were characterized by gel permeation chromatography, a combination of static and dynamic light scattering, and proton nuclear magnetic resonance.

7.2.3 Preparation of PS coated AuNPs

The dodecanethiol coated nanoparticles (AuNPs@DT) in THF (2.0 mg/mL with 5

mL) was concentrated via centrifugation (29000 rcf, 30 min), while thiol teriminated polystyrene was dissolved in THF, and past through 450 nm filter. Then the AuNPs@DT solution was added dropwise to the polymer solution under stirring, followed by 5 min sonication followed by 30 min N_2 bubbling. The mixture was left stirring for 3 days, before separation by more than 5 times centrifugation (29000 rcf, 40 min) to remove excess unbounded free polystyrene. Finally, polystyrene coated gold nanoparticles (AuNPs@DT@PS) were redissolved in THF again, to a final stock solution with gold mass concentration of 1.0 mg/mL.

7.2.4 Incorporation of AuNPs into block copolymer micelles

The AuNPs@DT@PS and PS_{285}-*b*-PI_{245} copolymer were mixed and dissolved in 3 mL THF with pre-determinated weight ratio (1/6, 1/10 and 1/20). Then 3 mL *n*-hexane was slowly added at 2 mL/hr under stirring. Then the gold nanoparticle and polymer solution was under sonication for 10 min to ensure completely uniform dispersion of the solute, before the large amount of *n*-hexane was quickly added under vigorous stirring to fix the spherical micelles with final THF content of 12.5% in the solution. The prepared hybrid spherical micelles solution were left undisturbed at room temperature for more than two weeks to ensure that they reached the thermodynamically stable state before laser light scattering measurement and nanopore extrusion.

7.2.5 Nanopore extrusion

An SGE gastight syringe and a Whatman 20-nm filter were used. The double-layer structure of the membrane was well-characterized.[42] The upper thick layer (59 μm) and the under thin layer (1 μm), respectively, contain 200- and 20-nm pores with pore number of ~ 9×10^8. On average, each small pore is covered by a large one. Spherical hybrid micelles solution was stored in the syringe and the solution after extrusion was collected into a pre-dust-free vial (typical volume of 1 mL) for further LLS measurement. The nanopore extrusion experiment was performed at room temperature and the flow rate for nanopore extrusion of micellar solution was fixed at 20 mL/hr, realized by a Harward-2000 syringe pump.

7.2.6 Characterization methods

The Transmission electron microscopy (TEM) imaging was performed on an FEI

CM 120 microscpe operated at 120 kV. 10 μL of the polymer solutions was placed onto carbon-coated copper grids, followed by drying in ambient air with a hair dryer.

A commercial LLS spectrometer (ALV/DLS/SLS-5022F) equipped with a multi-τ digital time correlator (ALV5000) and a cylindrical 22 mW He-Ne laser (λ_0 = 632 nm,Uniphase) as the light source was used. In dynamic LLS, the Laplace inversion of each measured intensity-intensity time correlation function $G^{(2)}(t,q)$ in the self-beating mode can lead to a line-width distribution $G(\Gamma)$. For a pure diffusive relaxation, Γ is related to the translational diffusion coefficient D, i.e., $\Gamma = Dq^2$ at $q \rightarrow 0$ and $c \rightarrow 0$, or further to the hydrodynamic radius R_h by the Stocks-Einstein equation, $R_h = k_B T/6\pi\eta D$, where k_B, T and η are the Boltzmann constant, the absolute temperature and the solvent viscosity, respectively.

UV-vis spectra were recorded on a Varian Cart 50 spectrophometer, between 300 and 900 wavelength. Dilute solutions of the gold nanoparticles and hybrid micelles were measured in glass cuvettes, using pure solvent as a reference.

7.3 Results and Discussion

Figure 7.1 is a scheme presenting the procedure for this new approach to the fabrication of hybrid cylindrical micelles. In brief, the dodecanethiol stabilized gold nanoparticles synthesized in organic solvent are further decorated with thiol-terminated polystyrene, followed by encapsulation with diblock copolymer PS-*b*-PI in a mixture solvent of THF and *n*-hexane. The generated hybrid spherical micelles solution are subsequently used for extrusion through small nanopores (20 nm in diameter and 1000 nm in length purchased from Whatman), resulting in long hybrid cylindrical micelles with gold nanoparticles dispersed along the centerline.

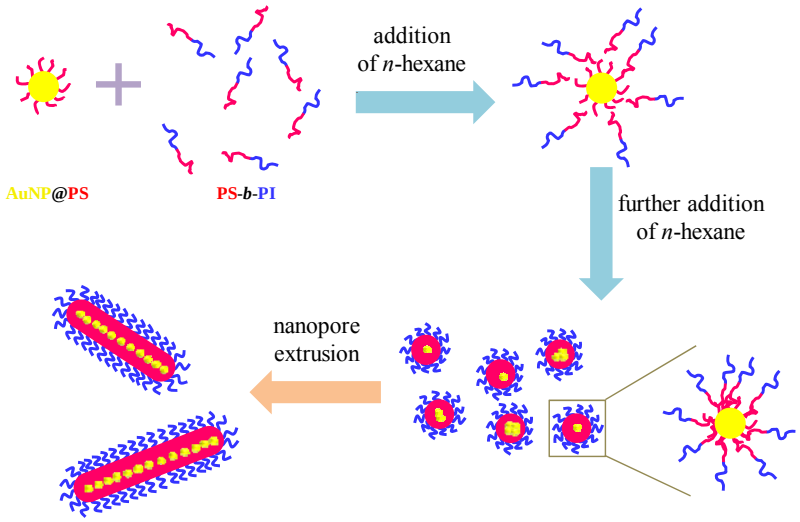

Figure 7.1. Schematic presentation of the procedure for the fabrication of hybrid cylindrical micelles.

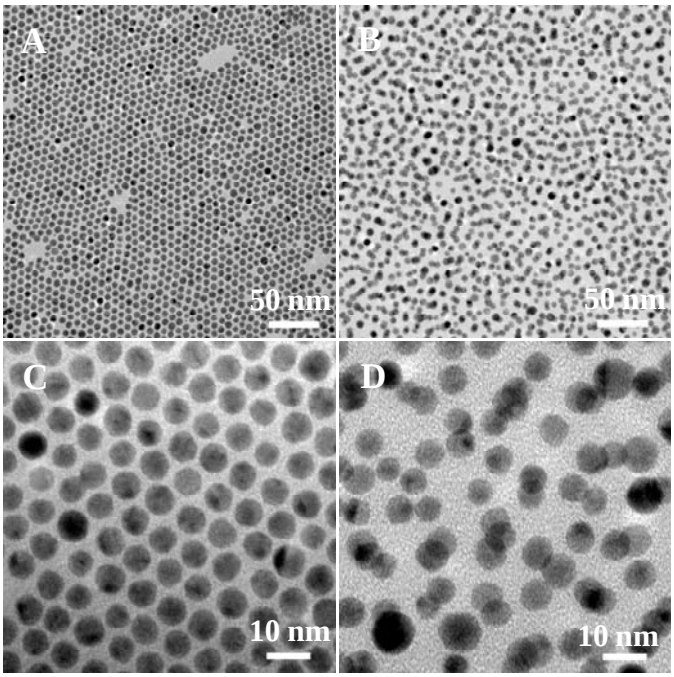

Figure 7.2. Presentative TEM images for (A and C) dodecanethiol stabilized AuNPs@DT and (B and D) polystyrene coated AuNPs@DT@PS in THF after purification via centrifugation (29000 rcf for 40 min) at different magnifications.

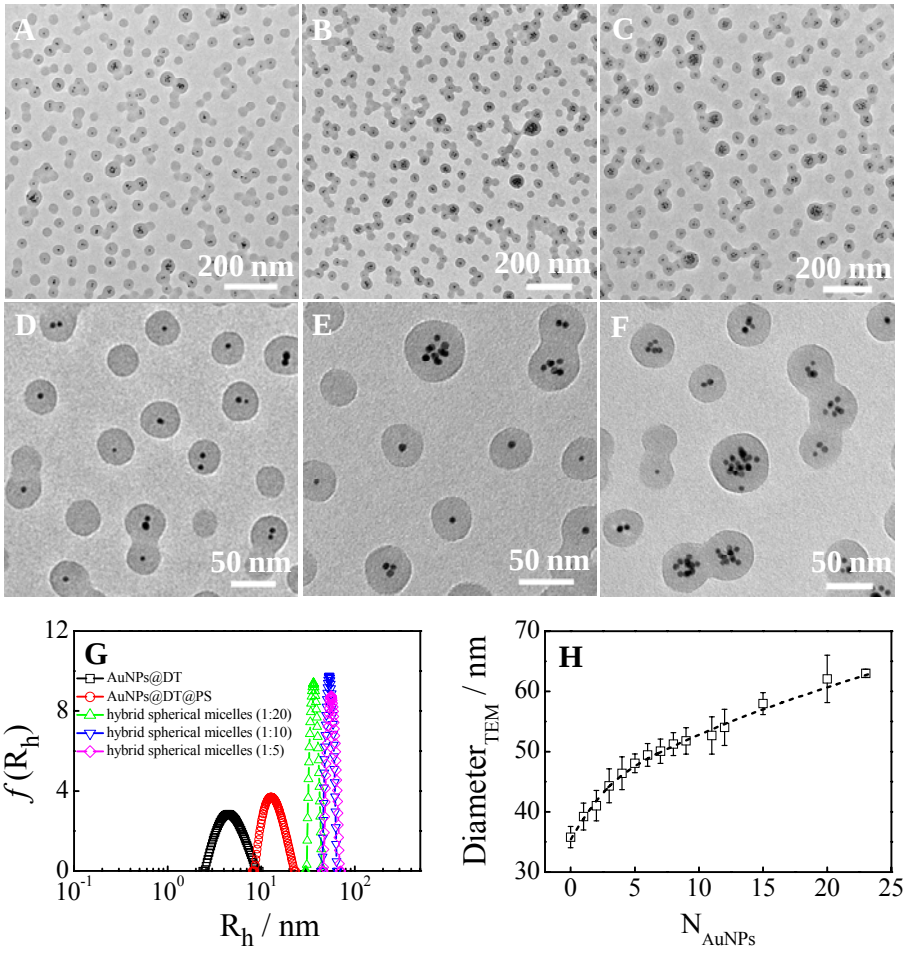

Figure 7.3. (A-F) TEM images for the hybrid spherical micelles with different $m_{AuNPs}/m_{PS\text{-}b\text{-}PI}$: (A and D) for 1:20; (B and E) for 1:10; and (C and F) for 1:5 at different magnifications; (G) hydrodynamic radius distributions for the AuNPs@DT, AuNPs@DT@PS in THF as well as the AuNPs encapsulated hybrid spherical micelles in solution measured at scattering angle of 20 °; and (H) average diameters of selected spherical micelles obtained from TEM images as a function of gold nanoparticles number per micelle.

TEM images for small dodecanethiol stabilized gold nanoparticles (AuNPs@DT) and polystyrene coated gold nanoparticles (AuNPs@DT@PS) dispersed in THF are presented in Figure 7.2 while that for the gold nanoparticle encapsulated spherical micelles with different mass ratio of AuNPs and PS-*b*-PI are shown in Figure 7.3. The slight coupling of small nanoparticles in Figure 7.2D confirms the successful coating of polymer chains on the particle surface. Average hydrodynamic diameter for AuNPs@DT in THF in Figure 7.3G was estimated to be 8.9 nm, larger than the diameter obtained from TEM analysis, 6.6 nm. Meanwhile,

the AuNPs@DT@PS in THF have average hydrodynamic diameter of 25.8 nm, much larger than diameter from TEM images, 6.9 nm. Then, average length of the polystyrene brushes on the nanoparticle surface can be estimated to be 8.4 nm in solution. Calculated fully stretched contour length, unperturbed end to end distance and experimentally measured hydrodynamic diameters for the free thiol-terminated polystyrene PS_{110}-SH are 33 nm, 7.7 nm and 4.2 nm, respectively, indicating a slightly stretched and probably, a cone-shaped volume (more stretched near the gold surface and more coiled away from the surface) for the PS brushes on gold nanoparticle surface.[43]

The hybrid spherical micelles are prepared by slowly adding the selective solvent *n*-hexane to the AuNPs@DT@PS and diblock copolymer PS-*b*-PI solution in THF, with a final THF content of 12.5% (v/v). In Figure 7.3A-F, it is found that AuNPs are located in the core part of the spherical micelles and average size of the hybrid spherical micelles could be controlled by incorporating different number of AuNPs into the micelles, realized by varying the relative starting mass ratio $m_{AuNPs}/m_{PS\text{-}b\text{-}PI}$. Figure 7.3H shows the diameter of the hybrid spherical micelles in TEM scales with the average AuNPs number per micelle encapsulated. The empty spherical micelles without nanoparticles incorporated have an average hydrodynamic radius of 30 nm, while after AuNPs are incorporated, the value increases to 36, 51, and 57 nm for micelles with $m_{AuNPs}/m_{PS\text{-}b\text{-}PI}$ of 1:20, 1:10, and 1:5, respectively (Figure 7.3G). Note that the number of AuNPs in each micelle is not quite uniform after preparation and there are still few empty spherical micelles even for $m_{AuNPs}/m_{PS\text{-}b\text{-}PI}$ = 1:5. This phenomenon might be due to the faster micellization of block copolymer unimers as the selective solvent *n*-hexane is added in the solution. And this could be improved through the optimization of the sample preparation strategy or precise separation of clusters through density gradient centrifugation.[44] Hybrid spherical micelles with even higher $m_{AuNPs}/m_{PS\text{-}b\text{-}PI}$ are not attempted, presumably because their corresponding hydrodynamic radius is too larger compared with the diameter of the nanopores used for extrusion later.

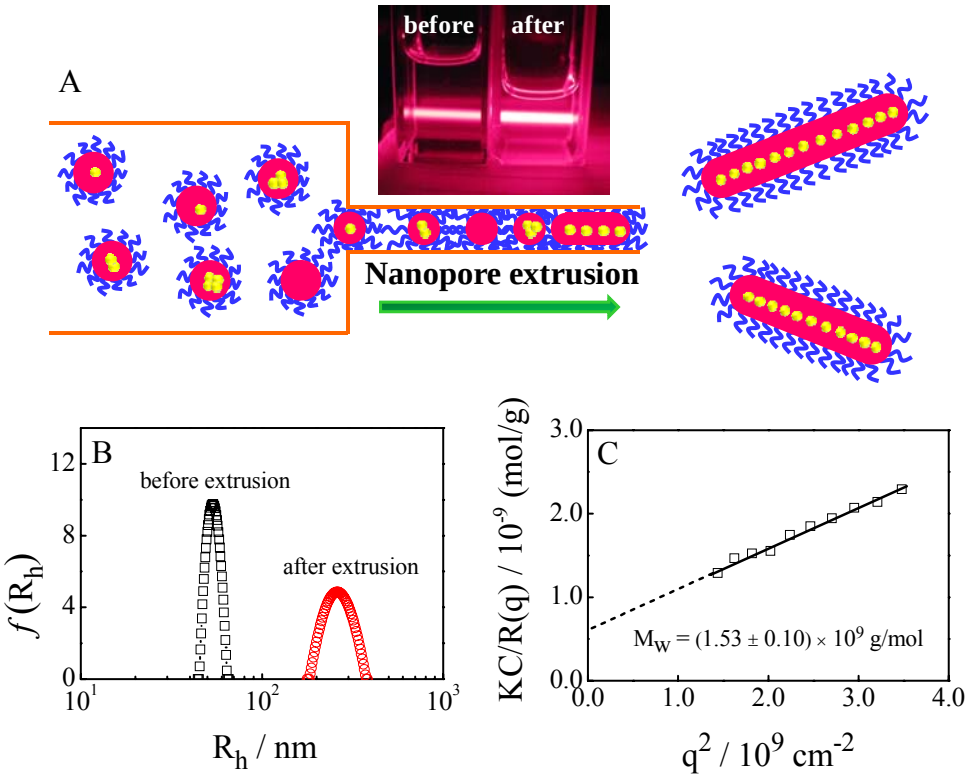

Figure 7.4. (A) scheme for the extrusion of hybrid spherical micelles through small cylindrical nanopores (20 nm×1000 nm); (B) hydrodynamic radius distributions for the micelles solution before and after extrusion (for $m_{AuNPs}/m_{PS\text{-}b\text{-}PI}$ = 1:10), which is obtained from LLS measurement at scattering angle of 20°; (C) Plot of KC/R(q) versus q^2 of the hybrid micelles in solution after extrusion through small cylindrical nanopores.

After the hybrid spherical micelles solutions were kept at room temperature for a sufficient time to reach its thermodynamically stable state, the solution was then transferred to a 10-mL gastight syringe equipped with a Harvard-2000 syringe pump for further extrusion through small cylindrical pores (20 nm in diameter) as Figure 7.4A shows. Using the hybrid spherical micelles with $m_{AuNPs}/m_{PS\text{-}b\text{-}PI}$ = 1:10 for example, laser light scattering (LLS) measurement revealed that the average scattering intensity increases by ~ 40 times for micelles solution collected after extrusion through the small nanopores and the measured corresponding average hydrodynamic radius $\langle R_h \rangle$ is ~ 250 nm, much larger than ~ 51 nm for hybrid spherical micelles before extrusion (Figure 7.4B). Static LLS shows the estimated average molar mass M_w = (1.53 ± 0.1) × 10^9 g/mol and average radius of gyration $\langle R_g \rangle$ = 450 nm for the micelles after extrusion (Figure 7.4C).

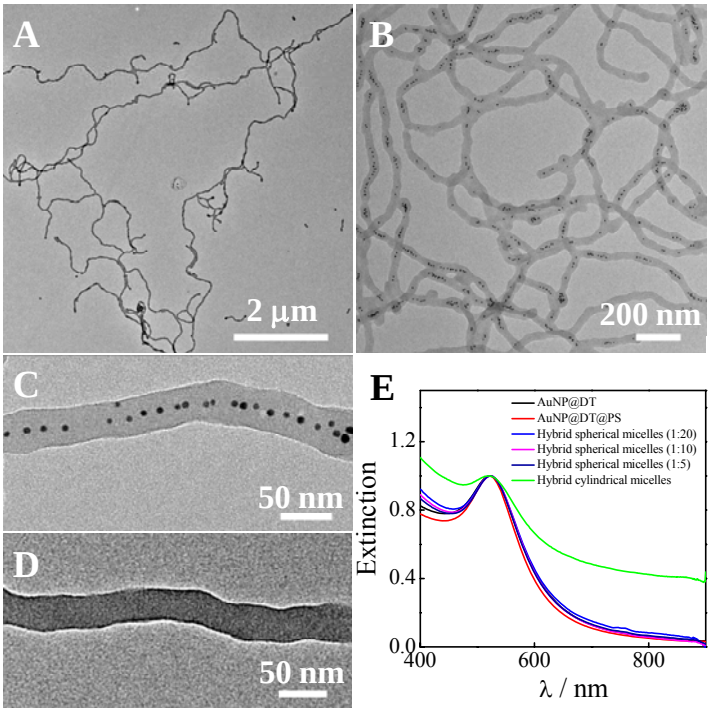

Figure 7.5. (A, B and C) TEM images for hybrid cylindrical micelles after their formation in extrusion of hybrid spherical micelles ($m_{AuNPs}/m_{PS\text{-}b\text{-}PI} = 10$) through small cylindrical pores (20 nm) at different magnifications; (D) TEM images for empty cylindrical micelles after formation in extrusion of block copolymer spherical micelles without AuNPs addition; and (E) ultraviolet-visible absorption spectra for the alkyl stabilized AuNPs@DT, polystyrene coated AuNPs@DT@PS in THF, hybrid spherical micelles with different $m_{AuNPs}/m_{PS\text{-}b\text{-}PI}$, and the hybrid cylindrical micelles obtained after nanopore extrusion for $m_{AuNPs}/m_{PS\text{-}b\text{-}PI} = 10$.

Transmission electron microscopy (TEM) was used to confirm the hybrid cylindrical micelles in the solution after nanopore extrusion. Figure 7.5A and B show TEM images for the hybrid cylindrical micelles with a diameter of ~ 39 nm and broadly distributed length. Each cylindrical micelle has lots of gold nanoparticles entrapped, and located along the centerline of the cylinder. Further detailed structure for the cylindrical micelles with AuNPs loaded is presented in Figure 7.5C while the empty cylindrical micelles prepared from extrusion of pure spherical micelles is given in Figure 7.5D for comparison. It is revealed that AuNPs could be roughly uniformly distributed along the nanofibers through this extrusion method. The measured absorption spectra of the generated hybrid cylindrical micelles are shown in Figure 7.5E, wherein that for AuNPs@DT, AuNPs@DT@PS in THF and hybrid

spherical micelles with different $m_{AuNPs}/m_{PS\text{-}b\text{-}PI}$ in the mixture solvent are also presented for comparison. All curves are quite close to each other, with the absorption peak at 522 nm, indicating no severe AuNPs aggregation in all dispersions.

We believe the detailed mechanism for the sphere-to-cylinder transition induced by the extrusion of the hybrid spherical micelles through small cylindrical pores should be similar to what we have found before for the empty spherical micelles.[40] Namely, as extrusion starts, hybrid spherical micelles are first accumulated at the pore entrance, because their hydrodynamic diameter is much larger than the nanopore. Under the hydrodynamic force of the elongational flow field, the blocked spherical micelles were squeezed into the nanopore and underwent the intermicellar fusion inside the nanopore while more spherical micelles are continuously accumulated at the pore entrance, resulting in the rearrangement of individual spherical micelles into long cylindrical micelles inside the nanopore. We have pointed out the moderate softness is key important for the transition, soft enough for the intermicellar core fusion, but solid enough for preventing fast intermicellar fission. Such softness can be carefully tuned by the addition of the good solvent to swell the spherical micelles. In the current study, the incorporation of metal nanoparticles into the micellar core can also significantly influence the softness of the micelles. We have found that extrusion of hybrid spherical micelles with even higher $m_{AuNPs}/m_{PS\text{-}b\text{-}PI}$ could not result in cylindrical micelles, but the breakdown of the nanopore membranes. In principle, starting with different $m_{AuNPs}/m_{PS\text{-}b\text{-}PI}$ for the hybrid spherical micelles ready for nanopore extrusion, we are able to prepare hybrid cylindrical micelles with controllable nanoparticles loading density along the line.

7.4 Conclusion

In conclusion, we have demonstrated a new conceptual method for the preparation of hybrid and peapod-like cylindrical micelles by extrusion through small cylindrical pores. The block copolymer spherical micelles before extrusion are pre-loaded with small gold nanoparticles via co-self-assembly in the solution. The cylindrical micelles are formed due to the compression and forced fusion of spherical micelles inside the long cylindrical pores. Such sphere-to-cylinder transition induced by nanopore-extrusion could be completed in microseconds to seconds and the

generated hybrid cylindrical micelles have a uniform diameter ~ 38 nm and length as long as ten micrometers. Further, small gold nanoparticles could be roughly uniformly distributed along the nanofibers while its loading density could be controlled by varying the starting mass ratio of $m_{AuNPs}/m_{PS\text{-}b\text{-}PI}$ during the preparation of hybrid spherical micelles. Finally, it is believed that other functional nanoparticles could also be embedded into the polymer nanofibers through nanopore extrusion. The simplicity and versatility of this method make it a powerful route for the preparation of multifunctional cylindrical polymer micelles by introducing functional nanoparticles with desirable optical, electronic and magnetic properties into such micelles for diagnostic imaging, drug delivery, sensors, and device fabrication.

7.5 References and Notes

(1) Riess, G., *Progr. Polym. Sci.* **2003,** 28, 1107-1170.

(2) Blanazs, A.; Armes, S. P.; Ryan, A. J., *Macromol. Rapid Commun.* **2009,** 30, 267-277.

(3) Moughton, A. O.; Hillmyer, M. A.; Lodge, T. P., *Macromolecules* **2012,** 45, 2-19.

(4) Pochan, D. J.; Chen, Z. Y.; Cui, H. G.; Hales, K.; Qi, K.; Wooley, K. L., *Science* **2004,** 306, 94-97.

(5) Li, Z. B.; Kesselman, E.; Talmon, Y.; Hillmyer, M. A.; Lodge, T. P., *Science* **2004,** 306, 98-101.

(6) Oh, H.; Green, P. F., *Nat. Mater.* **2009,** 8, 139-143.

(7) Lin, Y.; Boker, A.; He, J. B.; Sill, K.; Xiang, H. Q.; Abetz, C.; Li, X. F.; Wang, J.; Emrick, T.; Long, S.; Wang, Q.; Balazs, A.; Russell, T. P., *Nature* **2005,** 434, 55-59.

(8) Balazs, A. C.; Emrick, T.; Russell, T. P., *Science* **2006,** 314, 1107-1110.

(9) Goldman, E. R.; Mattoussi, H., *Nat. Mater.* **2005**, 435-446.

(10) Daniel, M. C.; Astruc, D., *Chem. Rev.* **2004,** 104, 293-346.

(11) Lu, A. H.; Salabas, E. L.; Schuth, F., *Angew. Chem.-Int. Edit.* **2007,** 46, 1222-1244.

(12) Sailor, M. J.; Park, J. H., *Adv. Mater.* **2012,** 24, 3779-3802.

(13) Mai, Y. Y.; Eisenberg, A., *Acc. Chem. Res.* **2012,** 45, 1657-1666.

(14) Kang, Y.; Taton, T. A., *Angew. Chem.-Int. Edit.* **2005,** 44, 409-412.

(15) Kang, Y.; Taton, T. A., *Macromolecules* **2005,** 38, 6115-6121.

(16) Kim, B.-S.; Qiu, J.-M.; Wang, J.-P.; Taton, T. A., *Nano letters* **2005,** 5, 1987-1991.

(17) Sanchez-Gaytan, B. L.; Cui, W. H.; Kim, Y. J.; Mendez-Polanco, M. A.; Duncan, T. V.; Fryd, M.; Wayland, B. B.; Park, S. J., *Angew. Chem.-Int. Edit.* **2007,** 46, 9235-9238.

(18) Kamps, A. C.; Sanchez-Gaytan, B. L.; Hickey, R. J.; Clarke, N.; Fryd, M.; Park, S. J., *Langmuir* **2010,** 26, 14345-14350.

(19) Hickey, R. J.; Haynes, A. S.; Kikkawa, J. M.; Park, S. J., *J. Am. Chem. Soc.* **2011,** 133, 1517-1525.

(20) Luo, Q. J.; Hickey, R. J.; Park, S. J., *ACS Macro Lett.* **2013,** 2, 107-111.

(21) Im, J. S.; Yun, J.; Kim, J. G.; Lee, Y. S., *Curr. Org. Chem.* **2013,** 17, 1424-1433.

(22) Leung, V.; Ko, F., *Polym. Adv. Technol.* **2010,** 22, 350-365.

(23) Geng, Y.; Dalhaimer, P.; Cai, S.; Tsai, R.; Tewari, M.; Minko, T.; Discher, D. E., *Nat. Nanotechnol.* **2007,** 2, 249-255.

(24) Shen, S.; Henry, A.; Tong, J.; Zheng, R. T.; Chen, G., *Nat. Nanotechnol.* **2010,** 5, 251-255.

(25) Yang, J. Z.; Yu, J. W.; Fan, J.; Sun, D. P.; Tang, W. H.; Yang, X. J., *J. Hazard. Mater.* **2011,** 189, 377-383.

(26) Huang, C. B.; Soenen, S. J.; Rejman, J.; Trekker, J.; Liu, C. X.; Lagae, L.; Ceelen, W.; Wilhelm, C.; Demeester, J.; De Smedt, S. C., *Adv. Funct. Mater.* **2012,** 22, 2479-2486.

(27) Kalra, V.; Lee, J.; Lee, J. H.; Lee, S. G.; Marquez, M.; Wiesner, U.; Joo, Y. L., *Small* **2008,** 4, 2067-2073.

(28) Lee, C. H.; Tian, L. M.; Abbas, A.; Kattumenu, R.; Singamaneni, S., *Nanotechnology* **2011,** 22.

(29) Duxin, N.; Liu, F.; Vali, H.; Eisenberg, A., *J. Am. Chem. Soc.* **2005**, 392-398.

(30) Wang, X.-S.; Wang, H.; Coombs, N.; Winnik, M. A.; Manners, I., *J. Am. Chem.*

Soc. **2005,** 127, 8924-8925.

(31) Djalali, R.; Li, S. Y.; Schmidt, M., *Macromolecules* **2002,** 35, 4282-4288.

(32) Wang, H.; Patil, A. J.; Liu, K.; Petrov, S.; Mann, S.; Winnik, M. a.; Manners, I., *Adv. Mater.* **2009,** 21, 1805-1808.

(33) Walther, A.; Yuan, J.; Abetz, V.; Muller, A. H. E., *Nano Letters* **2009,** 9, 2026-2030.

(34) Zhang, M.; Wang, M. F.; He, S.; Qian, J. S.; Saffari, A.; Lee, A.; Kumar, S.; Hassan, Y.; Guenther, A.; Scholes, G.; Winnik, M. A., *Macromolecules* **2010,** 43, 5066-5074.

(35) Li, W. K.; Liu, S. Q.; Deng, R. H.; Zhu, J. T., *Angew. Chem.-Int. Edit.* **2011,** 50, 5865-5868.

(36) Mai, Y. Y.; Eisenberg, A., *Macromolecules* **2011,** 44, 3179-3183.

(37) Chen, Q.; Zhao, H.; Ming, T.; Wang, J.; Wu, C., *J. Am. Chem. Sci.* **2009,** 131, 16650-16651.

(38) Sugie, A.; Somete, T.; Kanie, K.; Muramatsu, A.; Mori, A., *Chem. Commun.* **2008**, 3882-3884.

(39) Hong, L. Z.; Zhu, F. M.; Li, J. F.; Ngai, T.; Xie, Z. W.; Wu, C., *Macromolecules* **2008,** 41, 2219-2227.

(40) Chen, Q.; Wang, J.; Wu, C., *In preparation*.

(41) Quirk, R. P.; Ocampo, M.; Polce, M. J.; Wesdemiotis, C., *Macromolecules* **2007,** 40, 2352-2360.

(42) Jin, F.; Wu, C., *Phys. Rev. Lett.* **2006,** 96, 237801.

(43) Wuelfing, W. P.; Gross, S. M.; Miles, D. T.; Murray, R. W., *J. Am. Chem. Soc.* **1998,** 120, 12696-12697.

(44) Chen, G.; Wang, Y.; Tan, L. H.; Yang, M. X.; Tan, L. S.; Chen, Y.; Chen, H. Y., *J. Am. Chem. Soc.* **2009,** 131, 4218-4219.

Appendix

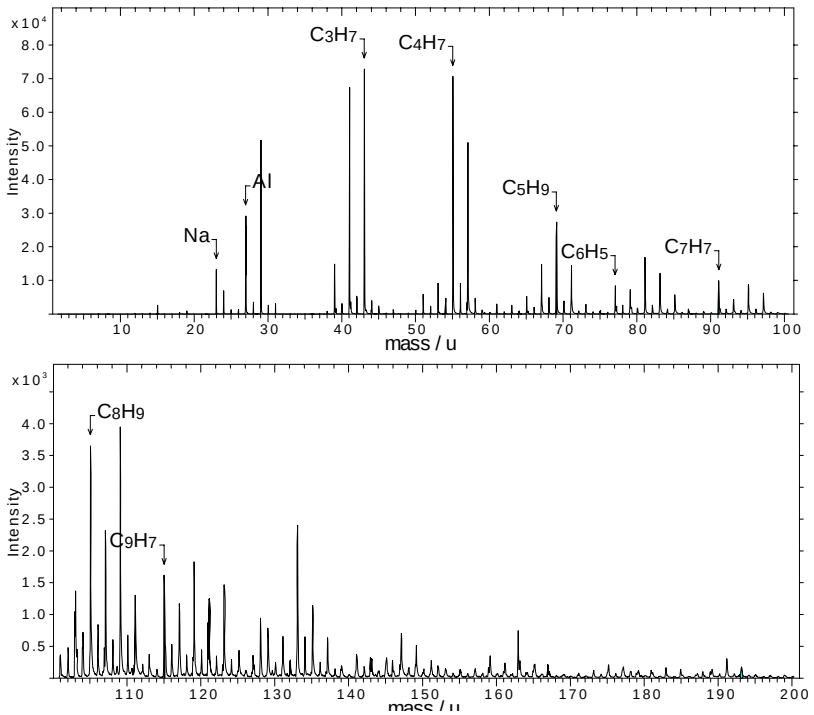

Figure 5.S1. Positive TOF-SIMS spectra in the mass range *m*/*z* 0-200 *u* for PS-*b*-PI adsorption layer on aluminum oxide membrane surface after washing with vast volume of THF solvent. Characteristic peaks for polystyrene in plot include 27, 39, 51, 77, 91, 103 etc. and for polyisoprene include 41, 69, 81, 93, 95, 119 etc.

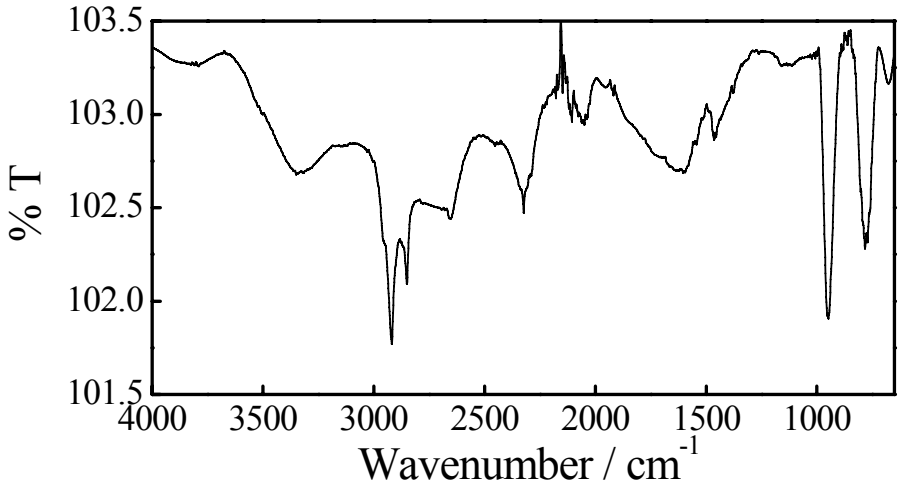

Figure 5.S2. ATR infrared spectra of PS-*b*-PI adsorption layer on aluminum oxide membrane surface after washing with vast volume of THF solvent. Characteristic peaks for PS include 2922, 2850 cm^{-1} and that for PI include 2324 cm^{-1}.

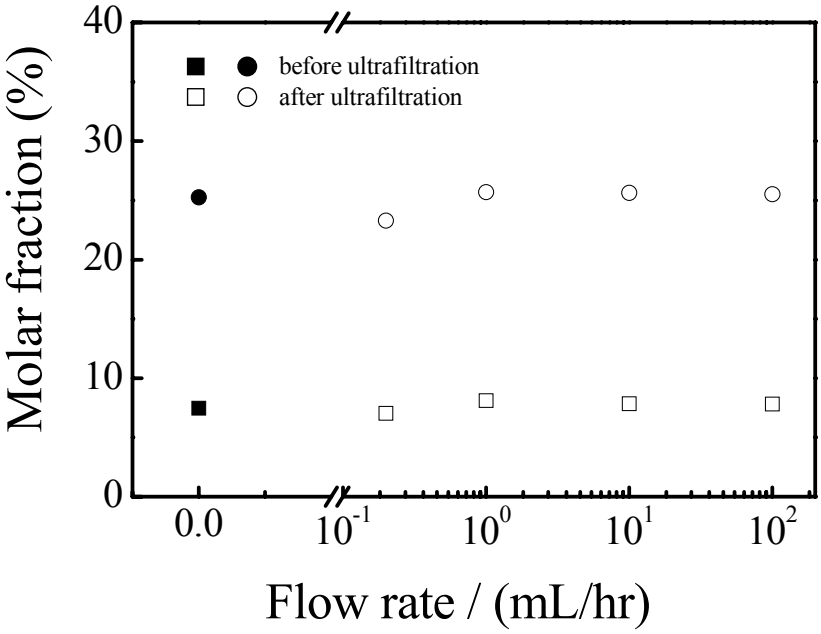

Figure 5.S3. Flow rate dependence of the molar fraction for the *n*-hexane/THF mixture solvent for ultrafiltration with 20 nm nanopores. The composition of the mixture solvent is determined by the ratio of C-CH_2-O for THF and C-CH_2-C for *n*-hexane from 1H NMR.

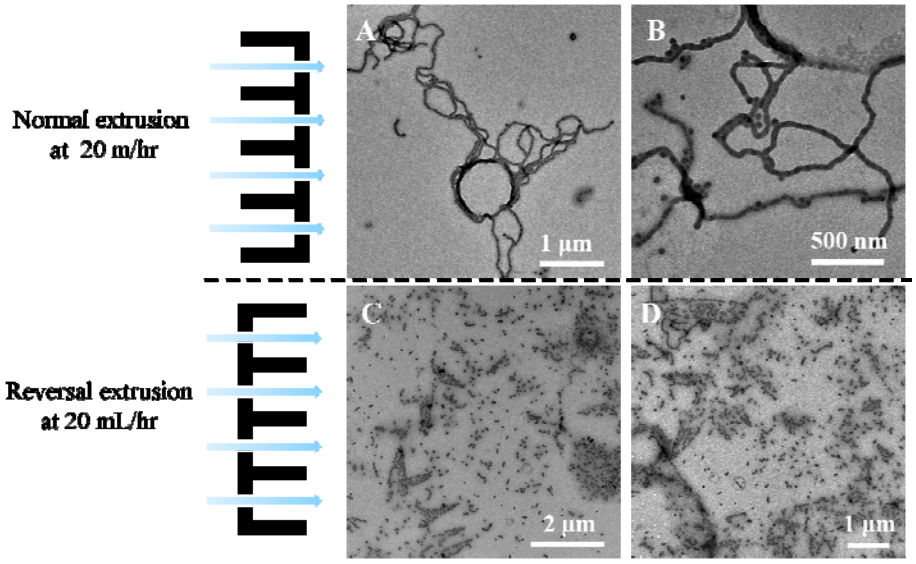

Figure 5. S4. TEM images for the micelles solution after nanopore extrusion, with normal 200 nm-to-20 nm direction (A and B) and reversal 20 nm-to-200 nm direction (C and D) with the same extrusion condition: flow rate 20 mL/hr, polymer concentration, 0.5 mg/mL, THF content, 18%. Only very few wormlike micelles could be generated for the reversal extrusion.

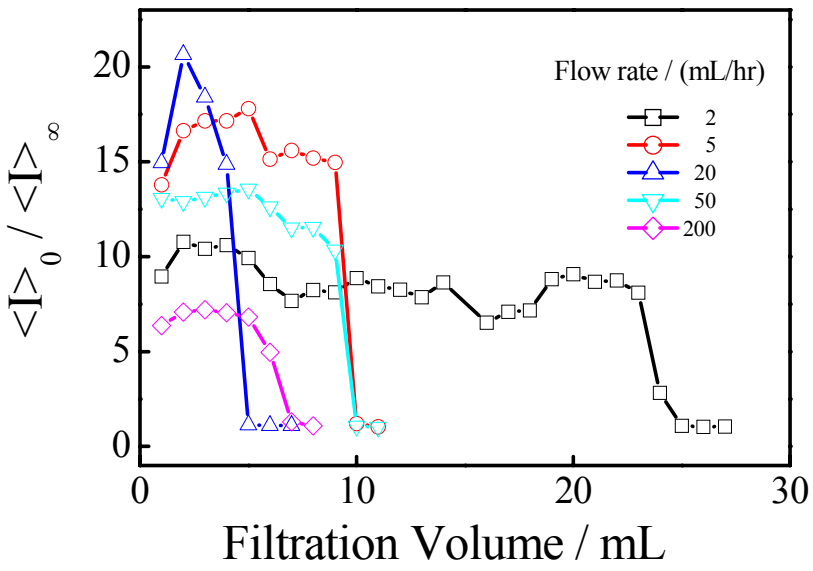

Figure S5. Filtration volume and extrusion flow rate dependence of sphere-to-fiber transition extent, $\langle I \rangle_0/\langle I \rangle_\infty$, for micelles extrusion through nanopores with THF content, 18% and block copolymer concentration, 0.5 mg/mL. The same filter membrane has been recycled by rinsing with vast THF solvent and drying at 50 ^{o}C overnight and then used for next cycle of extrusion.

Publications

1. Dong, Q.; **Chen, Q.**; Yang, W.; Zheng, Y.; Liu, X.; Li, Y.; and Yang, M. "Thermal Properties and Flame Retardancy of Polycarbonate/Hydroxyapatite Nanocomposite", *Journal of Applied Polymer Science,* **2008**, *109*, 659.

2. **Chen, Q.**; Zhao, H.; Ming, T.; Wang, J.; and Wu, C. "Nanopore Extrusion-Induced Transition from Spherical to Cylindrical Block Copolymer Micelles", *Journal of the American Chemical Society,* **2009**, *131*, *16650*.

3. **Chen, Q.**; Liu, J.; Schibel, A.; White, S and Wu, C. "Transolcation Dynamics of Poly(styrenesulfonic acid) through an α-Hemolysin Protein Nanopore", *Macromolecules*, **2010**, *43*, 10594.

4. Tan, M.; Wu, X.; Jeong, E.; **Chen, Q.** and Lu, Z. "Peptide-Targeted Nanoglobular Gd-DOTA Monoamide Conjugates for Magnetic Resonance Caner Molecular Imaging", *Biomacromolecules*, **2010**, *11*, 754.

5. Tan, M.; Wu, X.; Jeong, E.; **Chen, Q.**; Parker, D. and Lu, Z. "An Effective Targeted Nanoglobular Manganese (II) Chelate Conjugate for Magnetic Resonance Molecular Imaging of Tumor Extracellular Matrix", *Molecular Pharmaceutics*, **2010**, *4*, 936.

6. Zhao, H.; **Chen, Q.**; Hong, L.; Zhao, L.; Wang J.; and Wu, C. "What Morphologies Do We Want?-TEM Images from Dilute Diblock Copolymer Solutions", *Macromolecular Chemistry and Physics*, **2011**, *212*, 663.

7. **Chen, Q.**; Diao, S.; and Wu, C. "How does a supercoiled DNA chain pass through a small conical glass pore?", *Soft Matter*, **2012**, 8, 5451.

8. Lai, H.; **Chen, Q.** and Wu, P. "The Core-Shell Structure of PNIPAM Collapsed Chain Conformation Induced a Bimodal Transition on Cooling", *Soft Matte*r, **2013**, *9*, 3985.

9. **Chen, Q.**; Li, Y. and Wu, C. "How Long Cylindrical Micelles Formed after Extruding Block Copolymer in a Selective Solvent through a Small Pore Fragment back into Spherical Ones", *Macromolecules*, **2013**, *In revision*.

10. **Chen, Q.** and Wang, J. "Nanoparticle-Loaded Cylindrical Micelles from Nanopore Extrusion of Block Copolymer Spherical Micelles", **2013**, *submitted*.

11. **Chen, Q.** and Wu, C. "Enhanced Fluids Flow through Nanopores by Polymer Brushes" **2013**, *in preparation*.

12. **Chen, Q.**; Wang, J. and Wu, C. "Extrusion of Spherical Micelles Made of Block Copolymer through a Small Cylindrical Pore: Mechanism of Sphere-to-Cylinder Transition and the Effect of THF Content and Extrusion Flow Rate", **2013**, *in preparation*.